Investigating the Viscoelastic Properties of Aqueous Protein Systems by Brillouin Spectroscopy and Molecular Dynamics

by

© Dillon F. Hanlon

A thesis submitted to the School of Graduate Studies in partial fulfillment of the requirements for the degree of Doctor of Philosophy.

Department of Physics and Physical Oceanography
Memorial University

October 2023

St. John's, Newfoundland and Labrador, Canada

Abstract

In this study, we explore how proteins and water molecules interact which could be of importance in fully understanding biological processes. By using Brillouin light scattering and molecular dynamics together, we aim to learn more about these interactions. Specifically, Brillouin spectroscopy was employed to investigate the temperature dependence of the viscoelastic properties of gastropod mucus, in both its natural and hydrated and dehydrated states, and in a bacterial cell lysate solution. Additionally, time-dependent Brillouin scattering studies were conducted on dehydrated mucus. The concentration of proteins in both the hydrated and dehydrated states of gastropod mucus was determined using attenuated total reflectance (ATR) Fourier transform infrared (FTIR) spectroscopy. Molecular dynamics (MD) simulations were also performed on protein-water systems to explore bulk viscoelastic properties similar to those obtained from Brillouin spectroscopy.

The Brillouin spectra of natural gastropod snail mucus revealed two peaks. The first peak, located near 8.0 GHz, and was attributed to the longitudinal acoustic mode of the liquid mucus and persisted throughout the temperature range. The second peak, observed only at temperatures $T \leq -2.5^{\circ}$C and having a shift of approximately 18.0 GHz, indicated the presence of a phase transition. At this temperature, anomalies in the temperature dependent parameters of the longitudinal acoustic mode and the associated viscoelastic properties, as well as the emergence of the ice peak, suggested

a transition from a viscous liquid state to a coexistence of liquid mucus and solid ice phases. The incomplete phase transition, as indicated by the presence of an ice peak at -2.5°C, was attributed to glycoprotein-water interactions. Moreover, the Brillouin scattering results indicated that water molecules bind to glycoproteins in the mucus at temperatures above the freezing point, leading to a reduced capacity of bound water to facilitate freezing. Consequently, a gradual liquid-solid transition and depression of the freezing point occurred.

Temperature dependent Brillouin scattering on diluted and dehydrated mucus provide complimentary results to that of the natural mucus, while also adding results for the concentration dependence of snail mucus as a function of time. As the dilutions increased, the spectral parameters, frequency shift and full width at half maximum (FWHM), both decreased. Furthermore, with the addition of more water to the system, the freezing point depression observed in the natural snail mucus, increased from -2.5°C up to -1.0°C. The ice peak remained unchanged with varying dilution. Dehydrated mucus displayed a single peak attributed to the longitudinal acoustic mode of liquid mucus over the entirety of the experiment. The frequency shift increased as the protein concentration increased, as indicated by ATR data. Likewise, the FWHM also increased as protein concentration increased. Results from the dehydration experiments are indicative of a transition to a gel like phase once a protein concentration of ~ 50 wt% glycoproteins was reached. Furthermore, bacterial (*E. coli*) cell lysate in solution with water was investigated using Brillouin spectroscopy as a function of temperature. A single peak corresponding to the longitudinal acoustic mode of the fluid was observed, with frequency shifts consistently smaller than those of water throughout the temperature range studied.

In addition to experimental studies, molecular dynamic simulations were employed

to explore the viscoelastic properties of protein-water systems. The simulations covered a temperature range of 280K to 340K and revealed strong temperature dependence of properties such as bulk modulus, speed of sound, and viscosity. We observed a consistent increase in the bulk modulus, speed of sound, and viscosity as we increased the protein concentration. Notably, our molecular dynamics simulation results closely resemble the trends and behaviour observed in Brillouin scattering experiments conducted on aqueous protein solutions. This similarity in MD and experimental work validates the utility of simulations in exploring the viscoelastic properties of protein water solutions. Consequently, our work provides a strong rationale for using computer simulations with experimental techniques, offering potential for advancing our understanding of both simple and complex systems.

Collectively, this comprehensive study sheds light on the viscoelastic properties of different biological systems, providing valuable insights into phase transitions, water interactions, and the influence of protein concentration on their mechanical behavior.

Acknowledgements

First and foremost, a special thank you goes to my supervisor, Dr. Todd Andrews, for providing me with an abundance of guidance and inspiration throughout this project, especially when things were moving at a snail's pace. I would also like to send a big thank you to Dr. Maynard Clouter for his expertise and guidance, especially with designing the sample chamber used in this work. I would also like to acknowledge my colleagues within the Andrews' research group, Brad McNiven, and Stephen Spencer. As well, I would like to thank the faculty, staff and fellow graduate students in the Memorial University of Newfoundland Dept. of Physics and Physical Oceanography. Additionally, a great deal of appreciation goes to Dr. Ivan Saika-Voivod for his expertise and knowledge on the systems studies as well his helpful feedback throughout different stages of this work. Moreover, I would like to thank Dr. Stefan Wallin for his insights and feedback throughout the various stages of writing this thesis, including feedback giving during my comprehensive exam. I would also like to thank Dr. M. Shajahan G. Razul for his expertise and insights involving the molecular dynamic simulations. As well, I would like to thank Dr. Valerie Booth and Sina Heravi for their assistance with the cell lysate project.

I would also like to express my gratitude to the Natural Sciences and Engineering Research Council of Canada and the School of Graduate Studies for supplying financial support during my PhD program.

A great deal of appreciation goes to my friends and family, who have exhibited an enormous amount of support and patience throughout this whole process. Specifically, I would like to acknowledge: my parents, Alma and Fergus; my sisters, Lisa and Amanda; my brother Colin; and my grandmother Emily (Grammy).

Last, but certainly not least, I would like to thank my wife Kaitlyn, my dog Morris (Mo), and especially my daughter Sophie for providing me with the love and support throughout this whole process.

Statement of contribution

The thesis author (D. F. Hanlon) was the main contributor to all of the proceeding manuscripts, sharing authorship with Dr. G. Todd Andrews, the faculty supervisor for this graduate project.

This work resulted in four manuscripts: one entitled “Temperature Dependence of the Viscoelastic Properties of a Natural Gastropod Mucus by Brillouin Light Scattering Spectroscopy” which has been accepted into *Soft Matter* journal with reference *Soft Matter*, 2023, DOI: 10.1039/D3SM00762F., another entitled “Influence of Hydration and Dehydration on the Viscoelastic Properties of Snail Mucus by Brillouin Spectroscopy”, a third paper called “Brillouin light scattering studies of aqueous *E. Coli* cell lysate: Viscoelastic properties of a multimacromolecular solution” submitted to the Journal of Chemical Physics, and a fourth entitled “Probing the Viscoelastic Properties of Aqueous Protein Solutions using Molecular Dynamics Simulations”.

For all manuscripts, the writing responsibilities were shared from the outset of writing the document, the majority of Dr. Andrews’ input came once an initial draft of a given manuscript was completed. While the thesis author guided all the studies, completing most experiments and data analysis independently, discussions with Dr. Andrews provided invaluable insight and assistance throughout the course of the work. In addition, the first and second manuscript had Dr. Maynard Clouter as a co-author for his expertise and guidance designing and assisting with manufacturing the temperature controlled sample chamber. The third manuscript featured the collaborative contributions of Dr. Valerie Booth and Sina Heravi as co-authors. Their expertise and insights greatly enhanced the sections related to the production and extraction of bacterial cell lysate. Additionally, their valuable input played a significant role in refining the final draft of the manuscript which is soon to be submitted to a peer-reviewed journal. Similarly, the fourth manuscript had both Dr. Ivan Saika-Voivod and Dr. M. Shajahan G. Razul as co-authors. Their specialized knowledge in molecular dynamic simulations and their comprehensive understanding of protein-water systems significantly enhanced the work. Moreover, their constructive feedback and suggestions played a pivotal role in revising the final version of the manuscript which is ready for submission into a peer-reviewed journal.

Table of contents

List of tables

List of figures

List of symbols

η	apparent viscosity
v	sound velocity
τ	relaxation time
M^*	Complex longitudinal modulus
M'	Storage moduli
M''	Storage moduli
f_B	Brillouin frequency shift
ρ	Mass density
n	Refractive index
m	Mass
ω_i	angular frequency of incident light
ω_s	angular frequency of scattered light
Ω_i	angular frequency of phonon
$\mathbf{q}$	Wavevector of phonon
ϕ	angular offset between optical cavities of a tandem Fabry-Perot interferometer
λ	Wavelength of light
k_B	Boltzmann constant
Φ	Normalized correlation function of density fluctuation
$\delta\rho^*$	q^{th} component of density fluctuation
ρ	Number density
$S(q,\omega)$	Dynamic structure factor
M_s^0	0th moment dynamic structure factor
$S(q)$	Static structure factor
χ_T	Isothermal compressibility
G	Shear moduli
K	Bulk Moduli
ζ	Longitudinal kinematic viscosity
Γ	Full width at half maximum

List of abbreviations

AFP	Antifreeze Protein
AFM	Atomic Force Microscopy
A	Aperature
ATR	Attenuated Total Reflectance
BLS	Brillouin Light Scattering
BS	Beam splitter
FTIR	Fourier Transform Infrared
FWHM	Full width at half maximum
F	Filter
HDL	High Density Liquid
HWP	Half wave plate
M	Mirror
PEG	Polyethylene Glycol
PMT	Photomultiplier tube
PDB	Protein Data Bank
TBA	Tert-Butyl Alcohol
TMAO	trimethylamine-N-oxide
VNDF	Variable neutral density filter

Chapter 1

Introduction

1.1 Water: An Overview

Water is a vital and essential substance that plays a crucial role in many aspects of our lives. It is a simple molecule, composed of two hydrogen atoms covalently bonded to one oxygen atom, yet it exhibits a wide range of unique and complex physical and chemical properties [1, 2]. In this introduction, we will briefly explore some key physical properties of water as well as explore some of its unique characteristics, including its density, viscosity, and its ability to absorb and release heat, as well as its ability to dissolve a variety of substances [1]. Water is without a doubt one of, if not the, most investigated material on the planet, but the mechanisms underlying its different properties remain unknown. Its small size belies the complexities of its dynamics and physical properties. Unlike other molecules, the specific physical and chemical properties of liquid water are excellent for the circumstances required for life on Earth [2].

Figure 1.1 depicts the structure of water with chemical formula H_2O, in various

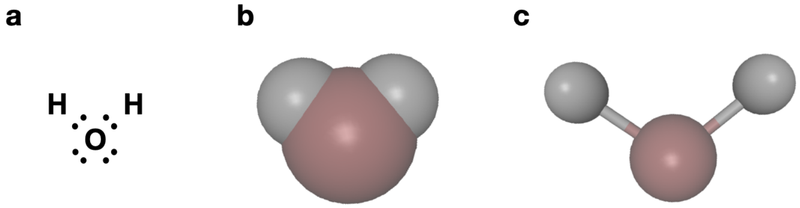

Figure 1.1: Three representations of the molecular shape of a water molecule described by: a) Lewis dot diagram b) space filling structure and c) ball and stick representation.

representations. In a water molecule, each hydrogen atom consists of a single positively charged proton which forms the nucleus and is surrounded by a single negatively charged electron. The oxygen atom, on the other hand, has a nucleus consisting of eight positively charged protons and eight uncharged neutrons, which is surrounded by eight negatively charged electrons [1]. When water molecules are formed, the ten electrons pair up to occupy five orbitals. One pair is closely associated with the oxygen atom, while two pairs are considered as “outside” electrons related to the oxygen atom. The remaining two pairs form the two identical O-H covalent bonds. The outer pairs, which are not involved in bonding, are known as lone pairs. These lone pairs repel each other, leading to the creation of electron clouds that spread out around the oxygen atom. This phenomenon is the primary factor contributing to the structure of water [3]. When compared to the one positive charge on each hydrogen atom, the eight positive charges in the oxygen nucleus powerfully attract all of these electrons. This results in hydrogen atoms that are partially depleted of electrons and hence partially positively charged, and an oxygen atoms that is partially negatively charged. Because of the bent structure and the presence of these charges, a dipole moment exists from the centre of the negative charge to the centre of the positive charge. Water becomes polar due to the presence of this dipole moment. The polarity of water is an important property that gives rise to many of its unique characteristics, both physical and chemical [3]. For example, the partial negative charge on the oxygen atom allows

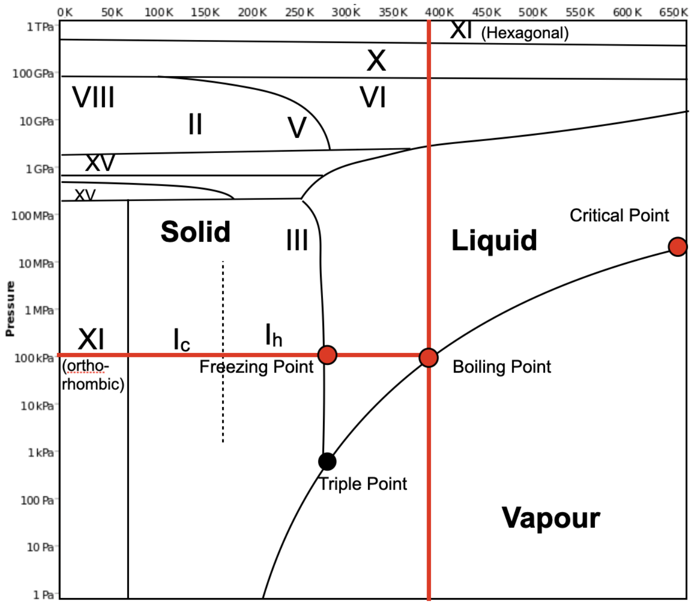

Figure 1.2: Simplified temperature and pressure phase diagram for water.

water to form hydrogen bonds with other water molecules. These bonds are relatively weak compared to covalent bonds, but they are abundant in water and contribute to its high surface tension and viscosity. The polarity of water also makes it a good solvent, allowing it to dissolve a wide range of polar and ionic substances. Solubility is the capacity of a solute to dissolve in a solvent. The excellent solvent properties of water, together with its non-toxic nature, make water a preferred solvent for many chemical reactions [4].

Water naturally exists in three primary states, namely, solid, liquid, and gas. These states are determined by the interplay of temperature and pressure as illustrated by the phase diagram in Fig. 1.2. Exploring the distinct phases of water is crucial for understanding its behavior and influence on a wide range of physical and chemical processes [3]. To illustrate the preferred physical states of water at different temperatures and pressures, phase diagrams are commonly employed. These diagrams provide a visual representation of the relationship between temperature, pressure, and the corresponding phases of water. However, the phase diagram of water is complex, featuring multiple triple points where all three phases coexist and one, or possibly two, critical points that mark the highest temperature and pressure at which distinct liquid and gas phases can coexist [5]. Ice, the solid state of water, is formed when liquid water is cooled below a temperature of T = 0°C at atmospheric pressure. However, the phase diagram of ice is remarkably complex, revealing at least 17 different phases of ice determined experimentally under various temperature and pressure conditions [3, 5]. These different phases of ice exhibit unique crystal structures and properties, some of which can only be observed at extreme temperatures and pressures. The phase we are most familiar with is ice Ih which can occur for temperatures as low as T = -60°C, and for pressures up to 200 MPa [1, 3]. There has been an extensive amount of work investigating the different phases of ice and research is still ongoing in this regard [6]. It is noticeable that most phase boundaries between the ices are parallel to the temperature axis, implying density-driven phase transformations [7]; entropy-driven phase transformations, such as ice Ih to liquid water, show phase boundaries approximately parallel to the pressure axis. All phases that share phase boundaries with liquid water (ices Ih, III, V, and VI and VII) have disordered hydrogen bonding [3]. Once liquid water is heated to a temperature of 100°C we find the onset of the gaseous phase of water in the form of vapor.

Water has a number of unusual anomalies that are still to this day being investigated [8]. For example, one of the fundamental characteristics of water is its density, which undergoes an interesting change during the transition from liquid to solid state. Most substances contract when cooled, but water does not, expanding and becoming less dense upon freezing [1, 9]. In addition to the transition observed from liquid to solid phases, there is another feature related to the density of water as it cools within the liquid state. Unlike most substances, which show a continuous increase in density as temperature decreases, water reaches its maximum density at approximately 4 °C [1, 9]. This behavior arises from the unique hydrogen bonding interactions among water molecules. At higher temperatures, water molecules have enough thermal energy to overcome the attractive forces of hydrogen bonds, leading to more random molecular arrangements and increased molecular spacing. As a result, water has a lower density as the temperature rises [10]. However, as water cools below 4°C, the hydrogen bonds become more stable, causing the water molecules to arrange themselves into a more organized structure. Furthermore, water exhibits a relatively high viscosity compared to many other common liquids, at room temperature, water viscosity is higher than that of substances like some commonly studied liquids, namely, ether and benzene [11]. This means that water flows more slowly and resists deformation or shearing forces. It has been stated that life depends on these anomalous properties of water [12]. The anomalous macroscopic properties of water are derived from its microscopic structuring and reflect the balance between low-density and high-density structures [13]. Attempting to understand these anomalies can lead to a better understanding of water itself, allowing for advancements in technological applications [8]. Overall, the physics of water is complex and multifaceted, and its unique properties have a profound impact on many aspects of our day-to-day lives.

1.2 Water: Interaction with Macromolecules

Proteins are vital for the proper functioning of living cells, and they are complex molecules composed of chains of amino acids linked together through peptide bonds [14]. When it comes to interacting with water, proteins and polymers do so by a number of ways including hydration processes and hydrogen bonding. The nature of these interactions can influence a protein's structure and function [15–19].

The process of hydration refers to the process by which water molecules are attracted to and surround the protein, forming a layer of water molecules that is bound to the protein surface, often referred to as the hydration shell [18]. The interactions between the protein and the water molecules in this hydration shell are important for stabilizing the proteins structure and allowing it to function properly [18]. Traditionally, water arranged around a solute belongs to the bulk water (free water). However, studies have shown that some of this water may be bound to the solute and should not be treated as bulk water but as part of the protein [20, 21]. In fact, one study even suggest that the proteins are capable of binding to all waters in the system [21]. As the protein-water interaction site occurs in the hydration shell, certain proteins behave differently in these regions, in particular antifreeze proteins. For example, antifreeze proteins (AFP) bind to ice crystals unlike most proteins [22]. The reason for this difference concerns the interaction area. They introduce greater order (lower entropy) in their hydration shell for their enthalpic binding of the surface water molecules [23]. Additionally, the presence of glycans attached to glycoproteins, a type of antifreeze proteins, imposes a long-range order on the water structure out to several nanometers, dependent on the orientation of the glycan [24].

In addition to hydration, proteins also interact with water through hydrogen bonding. This occurs when the partial positive charge on the hydrogen atoms of water molecules is attracted to the partial negative charge on the oxygen atoms of the protein [1, 9]. These hydrogen bonds can help stabilize the proteins secondary structure by adding extra support to the peptide bonds between the amino acids. The interactions between proteins and water can also influence the behavior of proteins in solution [25, 26]. For example, proteins that are highly hydrophobic, or water-fearing, tend to aggregate and form clumps in aqueous solutions [25, 27]. This is because the hydrophobic regions of the protein are not attracted to the water molecules and instead try to avoid contact with them. On the other hand, proteins that are highly hydrophilic, or water-loving, tend to dissolve easily in water and remain well-dispersed [25–28].

Overall, the interactions between proteins and water are very complex and multifaceted, and they play a crucial role in determining the structure and function of proteins. Understanding the physics of the molecular interactions occurring between proteins and water molecules can be important for a wide range of applications, including the processing and use of polymers in various industries such as medical and food sciences [29, 30].

1.3 Brillouin Scattering in Water

Brillouin scattering in water has proven to be an invaluable tool for probing its acoustic properties and unraveling the underlying mechanisms governing phonon propagation [31–34]. Understanding the acoustic behavior of water is fundamental in a number of research areas, including hydrodynamics, oceanography, condensed matter and biomedical research. This section briefly outlines the results previously obtained from Brillouin light scattering (BLS) spectroscopy studies performed on water.

To date, there have been a number of studies on normal or supercooled water by Brillouin scattering as a function of temperature [34–41]. These previous studies used a variety of wavelengths of light (*i.e.* 532 nm, 514.5 nm, or 488 nm) and employed either a 90° or 180° scattering geometry to collect Brillouin spectra. These studies primarily focused on examining the frequency shift and full width at half maximum (FWHM) of the longitudinal acoustic mode of water as temperature was varied. Furthermore, raw spectral signatures were used to gather data on sound velocity, bulk modulus, and sound absorption. In all of these studies, the sound velocity, and hence frequency shift, consistently increased as the temperature increased, and reached a maximum around 70°C [42]. Similarly, all studies revealed a notable decrease in sound velocity within the supercooled region ($T \leq 0$ °C). The speed of sound showed consistent values of approximately 1380 m/s at T = -20 °C and increasing to around 1580 m/s at T = 70 °C, which has been observed in previous studies. Furthermore, previous studies have also presented data on the FWHM, enabling the estimation of the apparent viscosity η. However, specific studies, such as the one mentioned in Ref. [35], employ viscosity calculations to extract information about the relaxation time of molecular fluctuations in water. Moreover, previous BLS studies on water [35, 36] have provided information on the frequency-independent sound absorption coefficient α/f^2, which is calculated from the FWHM. These studies reported sound absorption values ranging from ~ 70×10^{-15} s^2/m at T = -10 °C, which then decreased to around 5×10^{-15} s^2/m at T = 70 °C. Additionally, in Ref. [32], sound absorption was obtained for normal and supercooled water within the temperature range of -20 °C ≤ T ≤ 20 °C which showed a maximum value of 120×10^{-15} s^2/m at T = -20 °C and exponentially decreased to 20×10^{-15} s^2/m at T = 20 °C. Like the sound velocity results, there have been a few studies that investigate the behaviour of the sound absorption as a function of temperature [31, 42]. All studies show a rather rapid increase in α/f^2 at lower temperatures. The likely process behind the increase in sound attenuation has been attributed to shear and bulk viscosity and heat conduction in the medium [43]. Furthermore, it has been proposed that the relaxation process observed in water occurs between molecules because of the nonzero time value necessary for the restoring forces to drive the system to a local equilibrium altered by the local pressure (density) fluctuations [43]. Throughout the literature there have been a few studies on water using apparent viscosity in an attempt to try and understand relaxation times, one of which found the relaxation time τ to decrease from 2.5 ± 0.5 ps at T = 0 °C to 1.0 ± 0.5 ps at T = 15 °C [31].

Throughout the literature, there has been consistency in all reported Brillouin light scattering values on liquid water, whether it be frequency shift, FWHM, sound velocity or sound absorption [35, 36, 40, 44]. As briefly mentioned previously, there is a maximum in the sound velocity near 70 °C. The true reasoning behind this maximum is still to this day not quite clear. However, there have been a number of theories suggested as to why this maximum occurs, all relating to a two-state model [45–47]. According to the two-state model, water molecules can adopt two distinct states: the low-density liquid (LDL) state and the high-density liquid (HDL) state. These states exhibit variations in molecular packing and hydrogen bonding configurations. The LDL state is characterized by a more open structure with fewer hydrogen bonds, whereas the HDL state features denser packing and a higher number of hydrogen bonds, as described in Ref. [47]. This model offers a possible explanation for the observed anomalous behavior of the sound velocity maximum. However, further research is necessary to validate this theory. There have been a few studies however, that show that there is a minimum in the adiabatic compressibility (maximum in bulk modulus) which occurs at ~ 64 °C [48–50]. This result is rather odd seeing how the speed of sound and adiabatic compressibilty κ are directly related through $v = (1/\kappa\rho)^{1/2}$, where ρ is the mass density. The main theory behind the anomalous behaviour of the adiabatic compressibility and speed of sound is also attributed to this two-state model previously hypothesized [45–47].

Overall, the previous Brillouin scattering studies on water shows the influence temperature has on the speed of sound and sound attenuation. Understanding the behaviour of water is crucial for understanding the behaviour of aqueous protein solutions.

1.4 Brillouin Scattering in Aqueous Solutions

The viscoelastic properties of protein and polymer water solutions have been studied previously using Brillouin spectroscopy as a function of both temperature and concentration. By examining the speed of sound, sound absorption, viscosity, and complex longitudinal modulus, insights into the molecular behavior of these solutions can be determined. Brillouin scattering provides a non-invasive method to directly study these properties by analyzing the obtained spectra. Understanding the high-frequency viscoelasticity, specifically in the MHz to GHz range, using Brillouin light scattering is particularly valuable as it can uncover the connection between viscoelasticity and the dynamics and structure of polymer-water systems. This knowledge can have significant applications in various fields, such as understanding biomolecular behavior in different environments and the development of new biomaterials and therapies. In this section, we will review the results of several earlier studies focused on biomacromolecules and water solutions.

Previous Brillouin scattering studies [51–62], have consistently shown that the presence of biomacromolecules in aqueous solutions leads to an increase in the frequency shift observed in the Brillouin spectra. These studies have explored the relationship between frequency shift and factors such as concentration, temperature, or both. One common trend observed across all these studies is that the frequency shift tends to increase with higher protein concentration. Similarly, as the temperature increases, the frequency shift tends to decrease. Moreover, the full width at half maximum (FWHM) of the Brillouin linewidth, also obtained from the Brillouin spectra, exhibits a similar behavior in all investigated aqueous solutions. Specifically, an increase in protein concentration corresponds to an increase in the FWHM and related quantities derived from it. On the other hand, raising the temperature leads to a decrease in the FWHM.

Brillouin light scattering has been employed in several investigations on bio-fluids and bio-specimens to examine the influence of protein concentration on their viscoelastic properties [51–56, 60]. A BLS study on cell cytosol [51] demonstrated that as the concentration of proteins increased, the frequency shift increased from approximately 7.6 GHz at 0 wt% to around 9.0 GHz at 40 wt%. Notably, this increase followed a linear trend up to a protein concentration of 20 wt%. Furthermore, it was suggested that the Brillouin shift follows an universal trend as a function of concentration, up to approximately 40 wt% [51]. Similarly, a study on gelatin gels utilizing Brillouin light scattering investigated the viscoelastic properties as a function of concentration, showing a near-linear increase in the frequency shift from approximately 7.5 GHz to around 8.2 GHz for polymer concentrations up to 18 wt% [52, 60]. Various other studies employing Brillouin microscopy have reported frequency shift values ranging from 7.5 GHz to 7.8 GHz for different biological cells and proteins, including red blood cells, cytoplasm, nuclei, and ALS protein [53–56].

Brillouin light scattering was conducted on tert-butyl alcohol (TBA)–water solutions to investigate the role of the hydrophobic effect and interaction in biophysical and biochemical processes such as protein folding [59]. Similar to other polymer-water solutions, this study also demonstrated an increase in the frequency shift from approximately 7.5 GHz to around 7.8 GHz for TBA concentrations up to 12 wt%. Furthermore, this study on TBA investigated how the frequency shift changes with temperature, similar to the reference [57]. Both the Brillouin study on TBA [59] and the BLS study on hydrophobic polymers such as trimethylamine-N-oxide (TMAO), proline, and N-methylacetamide [57] demonstrated how the frequency shift varies with concentration and temperature. Moreover, both of these studies observed a decrease in the frequency shift with increasing temperature for all polymer concentrations. A similar behavior was also observed in a BLS study on aqueous solutions of polyethylene glycol (PEG) as a function of temperature and concentration.

A common trend in the frequency shift for all the aqueous protein/polymer systems is that they all have values close to that of water at low concentrations. Moreover, the frequency shift increases linearly for most systems up to approximate polymer concentrations of 20 wt% [52, 59]. Furthermore, it has been stated previously [52] that the frequency shift is very sensitive to polymer networks. Analogous observations can be made by investigating the sound velocity of these systems using Brillouin spectroscopy since the sound velocity is directly proportional to frequency shift. Typically the speed of sound for most aqueous protein solutions has a value of ~ 1500 - 1600 m/s at room temperature. Similar to the frequency shift, the sound velocity increases with increasing protein concentration up to values around 1850 m/s.

Spectral data from the above studies also show the results for the FWHM as a function of both concentration and temperature. The study on the biological fluids showed a near linear increase in the FWHM as the protein concentration increased. This trend was also observed in the studies on the hydrophobic polymers [57–59], as well as the BLS study on aqueous PEG solution [62], where the FWHM increased with increasing polymer concentration. The study by Ref. [57] and Ref. [59] also calculated the apparent viscosity from the FWHM as a function of concentration and temperature. The magnitude of the apparent viscosity increases with increasing concentration. These studies showed an Arrhenius behaviour for the high temperature region (T ≥ 20°C) while fitting an equation of the form $\eta = \eta_0 e^{E_a/k_B T}$ to the data. This fit was then used to extract the activation energy E_a. The activation energy showed no change with concentration, therefore linking the change in viscosity to the pre-factor η_0. The changes in this factor have previously been attributed to conformational changes in the hydration and further related to structural relaxation times [57, 59].

The complex longitudinal modulus M^* is a commonly calculated quantity in aqueous protein solutions [51, 57–59, 63]. It is defined as $M^* = M' + iM''$, where M' represents the storage modulus and M'' represents the loss modulus. These moduli are properties of viscoelastic materials. The storage modulus describes the amount of energy stored elastically in a system and is given by ρv^2, while the loss modulus describes the amount of energy dissipated as heat and is described by $2\pi\eta f_B$, where ρ, is mass density, v is the speed of sound, η is the apparent viscosity, and f_B is the Brillouin frequency shift [52, 59]. The complex longitudinal modulus provides valuable insights into the viscoelastic behavior of materials, as demonstrated in Ref. [63].

In the study mentioned above, it was observed that aqueous protein solutions exhibit a structural transition from a highly hydrated state to a gel-like state, and eventually to a low hydration state [63]. This study states that as the protein concentration increases, the solution undergoes a transition from a liquid-like state to a gel-like state, and finally to a solid-like state. According to the model proposed in Ref. [63] in the liquid-like state, both the frequency shift and the FWHM increase almost linearly with concentration. In the gel-like state, the frequency shift remains constant while the FWHM increases exponentially. Finally, in the solid-like state, the frequency shift remains constant, but the FWHM exponentially decreases. This model provides valuable insights into the relationship between the complex longitudinal modulus and the viscoelastic properties of protein solutions. Ref. [63], reported the transition from the liquid-like to gel-like state occurring at a concentration of ~ 40 wt%. This behaviour is similar to a study on hydrophobic molecules (TBA) where the frequency shift and apparent viscosity increase linearly up to a protein concentration of 18 wt% [57]. This is a likely indication that the system is still in a liquid-like state. Understanding these transitions can lead to an understanding in the interactions between protein and water molecules. The FWHM can also provide insight on the damping of sound waves in a fluid. A few Brillouin studies discussed previously provide results for the hypersound attenuation as a function of temperature [62]. In general, this results shows similar trends to that of the FWHM but can provide insight on the effect different types of proteins and molecules have on the damping of sound waves. Brillouin scattering studies on polypropylene glycol (PPG) were performed in Ref. [64] to investigate the hypersonic velocity, attenuation coefficient, and elastic moduli as a function of temperature. It was shown that the shape of the spectrum (i.e, frequency shift, FWHM, intensity etc.) is determined by the transport coefficients, elastic modulus and relaxation times of the polymers in the liquid. It was also found that the effect of temperature strongly influences the attenuation coefficient of sound waves in PPG.

The studies detailed in this chapter have all examined the temperature dependence of the frequency shift, full-width at half-maximum (FWHM), and other derived viscoelastic quantities of aqueous protein and polymer solutions. In general, it has been observed that the frequency shift tends to increase with higher protein concentration, while decreasing with rising temperature. This suggests that protein concentration plays a significant role in altering the viscoelastic properties, while temperature also plays a significant role. Similarly, the FWHM exhibits an overall increase with increasing protein concentration, but shows a decrease with higher temperature. These findings could provide valuable insights into the molecular-level interactions between proteins and water such as bonding between molecules or even on conformation changes. However, despite the progress made, there is still a need for a more comprehensive investigation to further understand these interactions. By utilizing Brillouin spectroscopy to investigate the properties obtained from these studies, we can gain a deeper understanding of the true nature of protein-water interactions. This technique offers a valuable tool to explore the viscoelastic properties and provides crucial information for a more comprehensive understanding of protein-water interactions at the molecular level.

1.5 Present Work

In the current work, Brillouin light scattering spectroscopy and attenuated total reflectance (ATR) - Fourier transform infrared (FTIR) spectroscopy was done on natural snail mucus in an attempt to determine the physics of the molecular interactions happening between protein and water at the molecular level. All Brillouin scattering experiments was conducted on natural and hydrated snail mucus was completed as a function of temperature. Meanwhile, experiments were conducted on dehydrated snail mucus over the course of 400 hours which inherently influenced the glycoprotein concentration as water evaporated from the system. Concentrations of proteins in the mucus were determined from the ATR-FTIR data. Furthermore, Brillouin scattering on an *E. coli* lysate solution was conducted as a function of temperature over the range $-5.0^{\circ}\mathrm{C} \leq T \leq 50.0^{\circ}\mathrm{C}$ in an attempt the understand the viscoelastic properties of such a complex system. In addition to these experimental techniques, computational studies were completed on a select number of protein-water system in an attempt to obtain values of bulk parameters such as bulk moduli, speed of sound and viscosity. Proteins for these studies were obtained through the Protein Data Bank (PDB) and were simulated using GROMACS v2022.3 [65–67]. All computations were completed over temperatures ranging between ~ 7°C and ~ 67°C .

The Brillouin scattering results for natural snail mucus show a singe peak due to the longitudinal acoustic mode of mucus for $T \geq -2.5$°C, and two peaks are present below this temperature attributed to the same mucus peak, and alongitudinal mode due to ice Ih. For *E. Coli* a single peak was observed for the entire temperature range studied [-5.0 °C, 50 °C], attributed to the longitudinal acoustic mode of the liquid cell lysate solution. Moreover, the viscoelastic properties obtained from Brillouin scattering experiments, including speed of sound, viscosity, and complex moduli, exhibit similar behaviours to results previously obtained on protein water systems [51–62]. In addition to the experiments, molecular dynamic simulations provided results for bulk moduli, sound velocity and viscosity which show similar trends to the results obtained via Brillouin scattering experiments in this work. Complementing this experimental work with computational studies could provide a comprehensive study on the viscoelastic properties of these systems. While experiments provide direct measurements and observations, computational models can offer insights into the underlying mechanisms governing a system. This is extremely important for understanding the molecular interactions happening between protein and water molecules. Furthermore, having both experiment and computational results exhibiting similar trends with one another provides confidence in the accuracy and reliability of the computational results to be used for modelling simple and complex systems in the future.

The significance of this work is twofold. Firstly, this study on aqueous protein water solutions provides new insights into the interaction between proteins and water. The concentration dependence of the freezing point depression of snail mucus provides insights for a new model of how glycoproteins bind to water molecules to depress the freezing point. Furthermore, the influence of glycoprotein concentration on viscoelastic properties of snail mucus reveals the influence of these proteins on the solution behavior and suggests alterations in molecular configuration at various concentrations. The similarity in behaviors between the viscoelastic proteins of simple and complex protein-water systems, particularly at lower protein concentrations, suggest that even complex systems such as *E.Coli* lysate solutions can be modelled by simple systems. This is particularly important for computer simulation where simple systems could be used to model the properties of complex systems. This work on *E.Coli* lysate solutions provides confidence that simple computer models can capture the physics of complex systems. Moreover, molecular dynamic simulations performed in this work were able to capture the overall viscoelastic behaviour and trends of aqueous protein solutions as seen in experiments. Secondly, the protein-water systems exhibit very interesting viscoelastic properties which are of fundamental interest due to the possible applications in both medical applications and food science [29, 30]. Understanding how these proteins behave in the presence of waters is crucial for these potential applications. Furthermore, this work aims to showcase the significance results from Brillouin light scattering spectroscopy has in understanding the molecular interaction in complex fluids.

Bibliography

[1] M. F Chaplin. Water: Its importance to life. *Biochemistry and Molecular Biology Education*, 29(2):54–59, 2001.

[2] C. H. Cho, G. W. Robinson, et al. Liquid water and biological systems: The most important problem in science that hardly anyone wants to see solved. *Faraday Discussions*, 103:19–27, 1996.

[3] C. E Boyd. *Water Quality: An Introduction*. Springer Nature, 2019.

[4] R. S Varma. Clean chemical synthesis inwwater. *Acc. Chem. Res*, 35:533, 2002.

[5] M. F Chaplin. Structure and properties of water in its various states. *Encyclopedia of Water: Science, Technology, and Society*, pages 1–19, 2019.

[6] C. G Salzmann. Advances in the experimental exploration of water's phase diagram. *The Journal of Chemical Physics*, 150(6), 2019.

[7] M. Seidl, A. Fayter, J. N. Stern, K. Amann-Winkel, M. Bauer, and T. Loerting. High-performance dilatometry under extreme conditions. *Proceedings of the 6th Zwick Academia Day 2015*, 76, 2015.

[8] P. Ball. Water—an enduring mystery. *Nature*, 452(7185):291–292, 2008.

[9] M. Chaplin. *The Water Molecule, Liquid water, Hydrogen Bonds and Water Networks*. Singapore: Pan Stanford Publishing Pte. Ltd, 2011.

[10] A Pietropaolo, R Senesi, C Andreani, A Botti, MA Ricci, and F Bruni. Excess of proton mean kinetic energy in supercooled water. *Physical Review Letters*, 100(12):127802, 2008.

[11] K Ni, H. Fang, Z. Yu, Z. Fan, and D. Reible. The effects of hydrogen bonding on the shear viscosity of liquid water. *International Journal of Sediment Research*, 34(1):8–13, 2019.

[12] W. AP Luck. The influence of ions on water structure and on aqueous systems. *Water and Ions in Biological Systems*, pages 95–126, 1985.

[13] F. Martelli. Unravelling the contribution of local structures to the anomalies of water: The synergistic action of several factors. *The Journal of Chemical Physics*, 150(9):094506, 2019.

[14] B. Alberts, A. Johnson, J. Lewis, M. Raff, K. Roberts, and P. Walter. The shape and structure of proteins. In *Molecular Biology of the Cell. 4th edition*. Garland Science, 2002.

[15] K. Tompa, M Bokor, T. Verebélyi, and P. Tompa. Water rotation arriers on protein molecular surfaces. *Chemical Physics*, 448:15–25, 2015.

[16] P. L Privalov and C. Crane-Robinson. Role of water in the formation of macromolecular structures. *European biophysics journal*, 46(3):203–224, 2017.

[17] F. Franks. Protein stability: the value of 'old literature'. *Biophysical Chemistry*, 96(2-3):117–127, 2002.

[18] L. Zhang, L. Wang, Y. Kao, W. Qiu, Y Yang, O. Okobiah, and D. Zhong. Mapping hydration dynamics around a protein surface. *Proceedings of the National Academy of Sciences*, 104(47):18461–18466, 2007.

[19] A. Paciaroni, S. Cinelli, E. Cornicchi, Alessio De Francesco, and Giuseppe Onori. Fast fluctuations in protein powders: the role of hydration. *Chemical Physics Letters*, 410(4-6):400–403, 2005.

[20] K. Meister, S. Ebbinghaus, Y. Xu, A. DeVries, M. Gruebele, D. M. Leitner, and M. Havenith. Long-range protein-water dynamics in hyperactive insect antifreeze proteins. *Proc. Natl. Acad. Sci.*, 110(5):1617–1622, 2013.

[21] S. Ebbinghaus, K. Meister, B. Born, A. L DeVries, M. Gruebele, and M. Havenith. Antifreeze glycoprotein activity correlates with long-range protein- water dynamics. *Journal of the American Chemical Society*, 132(35):12210–12211, 2010.

[22] S. Chakraborty and B. Jana. Antifreeze proteins: An unusual tale of structural evolution, hydration and function. In *Proc. Indian Natl. Sci. Acad.*, volume 100, pages 169–187, 2019.

[23] M. Schauperl, M. Podewitz, T. S Ortner, F. Waibl, A. Thoeny, T. Loerting, and K. R Liedl. Balance between hydration enthalpy and entropy is important for ice binding surfaces in antifreeze proteins. *Scientific reports*, 7(1):1–13, 2017.

[24] R. M Espinosa-Marzal, G. Fontani, F. B Reusch, M. Roba, N. D Spencer, and R. Crockett. Sugars communicate through water: Oriented glycans induce water structuring. *Biophysical Journal*, 104(12):2686–2694, 2013.

[25] K. A Dill. Dominant forces in protein folding. *Biochemistry*, 29(31):7133–7155, 1990.

[26] V. Daggett and A. Fersht. The present view of the mechanism of protein folding. *Nature Reviews Molecular Cell Biology*, 4(6):497–502, 2003.

[27] Ken Dill and Sarina Bromberg. *Molecular Driving Forces: Statistical Thermodynamics in Biology, Chemistry, Physics, and Nanoscience.* Garland Science, 2010.

[28] H. X. Zhou, G. Rivas, and A. P Minton. Macromolecular crowding and confinement: Biochemical, biophysical, and potential physiological consequences. *Annu. Rev. Biophys.*, 37:375–397, 2008.

[29] J. Li, A. D. Celiz, J. Yang, Q Yang, I. Wamala, W. Whyte, B. R. Seo, N. V. Vasilyev, J. J. Vlassak, and Z. Suo. Tough adhesives for diverse wet surfaces. *Science*, 357(6349):378–381, 2017.

[30] T. Uraji, H. Kohno, H. Yoshimura, M. Shimoyamada, and K. Watanabe. Freezing point depression of polyol-aqueous aolutions in the high concentration range. *Food Science and Technology International, Tokyo*, 2(1):38–42, 1996.

[31] J. Rouch, C. C. Lai, and S. H. Chen. Brillouin scattering studies of normal and supercooled water. *J. Chem. Phys.*, 65(10):4016–4021, 1976.

[32] J. Teixeira and J. Leblond. Brillouin scattering from supercooled water. *Journal de Physique Lettres*, 39(7):83–85, 1978.

[33] C. L.. O'Connor and J. P Schlupf. Brillouin scattering in water: the landau—placzek ratio. *J. Chem. Phys.*, 47(1):31–38, 1967.

[34] O. Conde, J. Leblond, and J. Teixeira. Analysis of the dispersion of the dound velocity in supercooled water. *Journal de Physique*, 41(9):997–1000, 1980.

[35] J Rouch, CC Lai, and SH Chen. Brillouin scattering studies of normal and supercooled water. *The Journal of Chemical Physics*, 65(10):4016–4021, 1976.

[36] C. L. O'Connor and J. P Schlupf. Brillouin scattering in water: the landau—placzek ratio. *The Journal of Chemical Physics*, 47(1):31–38, 1967.

[37] D. Liu, J. Xu, R. Li, R. Dai, and W. Gong. Measurements of sound speed in the water by brillouin scattering using pulsed nd: Yag laser. *Optics Communications*, 203(3-6):335–340, 2002.

[38] Jianfeng Xu, Xiaobin Ren, Wenping Gong, Rui Dai, and Dahe Liu. Measurement of the bulk viscosity of liquid by brillouin scattering. *Applied Optics*, 42(33):6704–6709, 2003.

[39] M Mijaković, B Kežić, L Zoranić, F Sokolić, Augustinus Asenbaum, Christian Pruner, Emmerich Wilhelm, and A Perera. Ethanol-water mixtures: Ultrasonics, brillouin scattering and molecular dynamics. *Journal of Molecular Liquids*, 164(1-2):66–73, 2011.

[40] O Conde, J Teixeira, and P Papon. Analysis of sound velocity in supercoled h2o, d2o, and water–ethanol mixtures. *The Journal of Chemical Physics*, 76(7):3747–3753, 1982.

[41] V. A. Del Grosso and C. W. Mader. Speed of sound in pure water. *the Journal of the Acoustical Society of America*, 52(5B):1442–1446, 1972.

[42] J. Teixeira and J. Leblond. Brillouin scattering from supercooled water. *J. de Phys. Lett.*, 39(7):83–85, 1978.

[43] S. Magazu, G. Maisano, D. Majolino, F. Mallamace, P. Migliardo, F. Aliotta, and

C. Vasi. Relaxation process in deeply supercooled water by mandelstam-brillouin scattering. *The Journal of Physical Chemistry*, 93(2):942–947, 1989.

[44] M. Hareng and J Leblond. Brillouin scattering in superheated water. *The Journal of Chemical Physics*, 73(2):622–625, 1980.

[45] CM Davis Jr and TA Litovitz. Two-state theory of the structure of water. *The Journal of Chemical Physics*, 42(7):2563–2576, 1965.

[46] A. Kumar, P. P. Pathak, and N. Dass. A study of speed of sound in water. *IOSR J. Appl. Phys.*, 8:21–23, 2016.

[47] L. G. M. Pettersson. A two-state picture of water and the funnel of life. In *Modern Problems of the Physics of Liquid Systems: Selected Reviews from the 8th International Conference "Physics of Liquid Matter: Modern Problems", Kyiv, Ukraine, May 18-22, 2018 8*, pages 3–39. Springer, 2019.

[48] S.V. Subrahmanyam and N. M. Moorthy. Effect of isomeric butanols on the temperature corresponding to the adiabatic compressibility minimum of water. *Journal of Solution Chemistry*, 4:347–357, 1975.

[49] V. B Corey. Adiabatic compressibilities of some aqueous ionic solutions and their variation with indicated liquid structure of the water. *Physical Review*, 64(11-12):350, 1943.

[50] G D'Arrigo and A Paparelli. Sound propagation in water–ethanol mixtures at low temperatures. i. ultrasonic velocity. *The Journal of Chemical Physics*, 88(1):405–415, 1988.

[51] S.V. Adichtchev, Y. A. Karpegina, K.A. Okotrub, M.A. Surovtseva, V.A. Zykova,

and N.V. Surovtsev. Brillouin spectroscopy of biorelevant fluids in relation to viscosity and solute concentration. *Physical Review E*, 99(6):062410, 2019.

[52] M. Bailey, M. Alunni-Cardinali, N. Correa, S. Caponi, T. Holsgrove, H. Barr, N. Stone, C. P. Winlove, D. Fioretto, and F. Palombo. Viscoelastic properties of biopolymer hydrogels determined by brillouin spectroscopy: A probe of tissue micromechanics. *Science Advances*, 6(44):eabc1937, 2020.

[53] G. Scarcelli, W. J Polacheck, H. T Nia, Kripa Patel, A. J Grodzinsky, R. D Kamm, and S. Hyun Yun. Noncontact three-dimensional mapping of intracellular hydromechanical properties by brillouin microscopy. *Nature Methods*, 12(12):1132–1134, 2015.

[54] G. Antonacci and S. Braakman. Biomechanics of subcellular structures by non-invasive brillouin microscopy. *Scientific Reports*, 6(1):1–6, 2016.

[55] Zhaokai Meng, S. C Bustamante Lopez, K. E Meissner, and V. V Yakovlev. Subcellular measurements of mechanical and chemical properties using dual raman-brillouin microspectroscopy. *Journal of Biophotonics*, 9(3):201–207, 2016.

[56] G. Antonacci, V. de Turris, A. Rosa, and G. Ruocco. Background-deflection brillouin microscopy reveals altered biomechanics of intracellular stress granules by als protein fus. *Communications Biology*, 1(1):1–8, 2018.

[57] L Comez, L Lupi, M Paolantoni, F Picchiò, and D Fioretto. Hydration properties of small hydrophobic molecules by brillouin light scattering. *The Journal of Chemical Physics*, 137(11):114509, 2012.

[58] L Comez, M Paolantoni, P Sassi, S Corezzi, A Morresi, and D Fioretto. Molecular properties of aqueous solutions: a focus on the collective dynamics of hydration water. *Soft Matter*, 12(25):5501–5514, 2016.

[59] L Lupi, L Comez, C Masciovecchio, A Morresi, M Paolantoni, P Sassi, F Scarponi, and D Fioretto. Hydrophobic hydration of tert-butyl alcohol studied by brillouin light and inelastic ultraviolet scattering. *The Journal of Chemical Physics*, 134(5):02B603, 2011.

[60] F. Palombo and D. Fioretto. Brillouin light scattering: applications in biomedical sciences. *Chemical reviews*, 119(13):7833–7847, 2019.

[61] G. S. Darbari, R. P. Sinsgh, and G. S. Verma. Temperature dependence of ultrasonic absorption in mixtures of glycerol and water. *Il Nuovo Cimento B (1965-1970)*, 41(1):15–24, 1966.

[62] M. Pochylski, F. Aliotta, Z. Blaszczak, and J. Gapiński. Structuring effects and hydration phenomena in poly(ethylene glycol)/water mixtures investigated by Brillouin scattering. *The Journal of Physical Chemistry B*, 110(41):20533–20539, 2006.

[63] M. Bailey, M. Alunni-Cardinali, N. Correa, S. Caponi, T. Holsgrove, H. Barr, N. Stone, C. P. Winlove, D. Fioretto, and F. Palombo. Viscoelastic properties of biopolymer hydrogels determined by brillouin spectroscopy: A probe of tissue micromechanics. *Sci. Adv.*, 6(44):eabc1937, 2020.

[64] C. H. Wang and Y. Y. Huang. Brillouin–rayleigh scattering studies of polypropylene glycol. iii. *The Journal of Chemical Physics*, 64(12):4847–4852, 1976.

[65] B. Hess, C. Kutzner, D. Van Der Spoel, and E. Lindahl. Gromacs 4: algorithms for highly efficient, load-balanced, and scalable molecular simulation. *Journal of chemical theory and computation*, 4(3):435–447, 2008.

[66] E. Lindahl, B. Hess, and D. Van Der Spoel. Gromacs 3.0: a package for molecular simulation and trajectory analysis. *Molecular modeling annual*, 7:306–317, 2001.

[67] D. Van Der Spoel, E. Lindahl, B. Hess, G. Groenhof, A. E M., and H. JC B. Gromacs: fast, flexible, and free. *Journal of computational chemistry*, 26(16):1701–1718, 2005.

Chapter 2

Theory & Methodology

2.1 Overview

Brillouin light scattering (BLS) spectroscopy is a powerful technique used to investigate the interaction between light and acoustic phonons in materials originally developed by Leon Brillouin in 1922 [1]. It serves as a valuable technique for investigating a material's elasticity and viscosity by measuring the longitudinal modulus in the GHz frequency range [2, 3]. Traditional methods for measuring viscoelastic properties typically involve contact forces. Other techniques, such as atomic force microscopy (AFM), the current standard in investigating the viscoelastic properties of proteins, and polymer solutions [4]. While AFM provides high transverse spatial resolution at the nanometer scale, measurements are averaged along the contact direction and heavily rely on mechanical models to extract values of, for example, Young Modulus E. Other methods for extracting elastic properties either require direct contact, introduce foreign particles, or are ineffective in certain situations such as when studying soft materials. Brillouin light scattering offers a non-destructive, and contact-free approach to study the viscoelastic properties of various systems directly from raw data. This chapter will provide an introduction to the theory behind BLS and the quantities that can be extrcated from the data.

2.2 Brillouin Light Scattering

2.2.1 Overview

Brillouin light scattering is an inelastic process arising from the interaction of light with spontaneous, thermally induced density fluctuations. These can be considered as microscopic acoustic waves, often called phonons. These acoustic waves, or sound waves, exhibit an intrinsic dependence on the viscoelastic properties of the material, in particular the complex longitudinal modulus M^*. Light scattered elastically from a sample has the same frequency as the incident laser light (532 nm). A small fraction of the incident light, however, can interact with the acoustic waves, and exchange energy and momentum in the process. Considering Fig 2.1a, this exchange in energy and momentum can be expressed by the following,

$$\hbar\omega_s = \hbar\omega_i \pm \hbar\Omega \tag{2.1}$$

and

$$\hbar\mathbf{k}_s = \hbar\mathbf{k}_i \pm \hbar\mathbf{q}, \tag{2.2}$$

where the indices i and s pertain to the incident and scattered light, respectively. Moreover, ω and $\mathbf{k}$ represent the frequency and wavevector of light, while Ω and $\mathbf{q}$

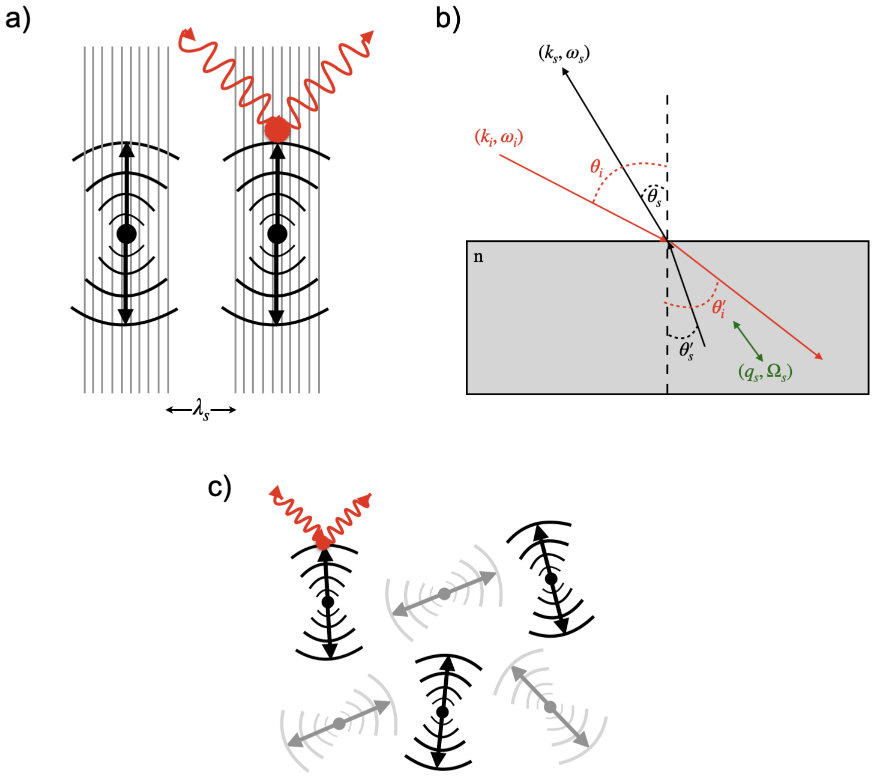

Figure 2.1: Brillouin light scattering process for a) scattering due to a Bragg reflection off thermally excited sound waves, b) light scattering process of creation (Stokes) and annihilation (anti-Stokes) of a phonon: $\omega_{i,s}$, $k_{i,s}$ - frequency and wave vector of incident and scattered light. Ω, $\mathbf{q}$ - frequency and wave vector of the phonon, and c) simplified schematic of random orientation of molecules in a liquid.

denote the frequency and wavevector of the phonon, respectively. During the scattering process, when a photon interacts with the medium, a phonon is either created or annihilated within the medium. This alteration in the presence of a phonon results in a change in energy for the scattered photon. Specifically, when a phonon is created, the scattered photon possesses less energy compared to the incident photon, while in the case of phonon annihilation, the scattered photon exhibits higher energy. These two phenomena are referred to as Stokes scattering and anti-Stokes scattering, respectively. For phonons propagating in the medium with refractive index n, the phonon wavevector $\mathbf{q}$ has both parallel and perpendicular components, where the magnitude of each are (see Fig 2.1b),

$$q_B^{\parallel} = n[k_i \sin\theta_i' + k_s \sin\theta_s'] \tag{2.3}$$

$$q_B^{\perp} = n[k_i \cos\theta_i' + k_s \cos\theta_s']. \tag{2.4}$$

where n is the refractive index of material and θ_i' and θ_s' are the angles that the internal incident and scattered light make inside the sample. Combining equations 2.3 and 2.4 yields the following,

$$q_B = [(q_B^{\parallel})^2 + (q_B^{\perp})^2]^{\frac{1}{2}} = n[k_i^2 + k_s^2 + 2k_ik_s(\sin\theta_i'\sin\theta_s' + \cos\theta_i'\cos\theta_s')]^{1/2}. \tag{2.5}$$

Using the fact that $k_i \simeq k_s$ since the velocity v_B of these phonons is much smaller than the speed of light then we can further simplify Eqn 2.5 to the following expression.

$$q_B = nk_i[2 + 2(\sin\theta_i'\sin\theta_s + \cos\theta_i'\cos\theta_s)]^{1/2} \tag{2.6}$$

Using the several trigonometric identities and the conservation of energy as in Eqn 2.1, Eqn 2.6 can be expressed into the following equation using $\Omega = 2\pi f_B = v_B q_B$,

$$f_B = \pm\frac{2f_iv_Bn}{c}\sin\frac{\theta}{2} \tag{2.7}$$

where $\theta = \pi + \theta_s - \theta_i'$. For $\theta = 180^\circ$ the bulk phonon velocity is,

$$v_B = \frac{f_B\lambda_i}{2n} \tag{2.8}$$

This intuitively can be understood as the density (acoustic) wave acting as a grating which diffracts the light: as the grating is travelling with velocity v, the scattered light experiences a frequency shift due to the Doppler effect. To explain this, first consider Figure 2.1b. The frequency shift of light incident on a medium can be derived by considering the interaction between a light wave with frequency f_i and wavelength λ_i and density waves travelling in a medium with frequency f_s. These density waves can be represented by regions of higher and lower densities as depicted in Fig 2.1. Constructive interference of light occurs when the Bragg condition

$$\lambda_i = 2nd\cos\phi$$

where d is the distance between consecutive density waves and ϕ is an arbitrary angle of incidence, is satisfied. It should be noted that, since the angle of incidence must equal the angle of reflection, the scattering angle θ then becomes $\theta = \pi - 2\phi$ so that the Bragg condition becomes

$$\lambda_i = 2nd\sin\frac{\theta}{2} = 2n\lambda_s\sin\frac{\theta}{2}. \tag{2.9}$$

If the density waves in Fig 2.1 are now moving with a velocity $\vec{v}$ then the scattered light is Doppler-shifted by an amount,

$$f_B = \pm\frac{2f_i vn}{c}\sin\frac{\theta}{2} \tag{2.10}$$

where c denotes the speed of light in vacuum, and n represents the refractive index of the medium. Equation 2.10 corresponds to the renowned Brillouin equation, originally formulated by Leon Brillouin in 1922 [1]. It is important to highlight that in the context of the current study, the backscattering geometry is employed, where θ is set to 180°. Using $\Omega = 2\pi f = vq$ the phonon velocity is

$$v_B = \frac{f_B \lambda_i}{2n}. \tag{2.11}$$

In liquids, molecules are randomly oriented as depicted in Fig 2.1c; it is this random orientation in liquids along with their interactions that give rise to the viscous nature of liquids [5, 6]. Changes in the Brillouin spectra measure the density fluctuations (sound waves) which are influenced by the inherent characteristics of randomly oriented molecules in the system.

It is well established that the scattering of light in fluids, as well as in any material, originates from fluctuations in the dielectric constant ϵ induced by thermally excited acoustic waves [1, 7–9]. During the scattering process, the frequency of the scattered light ucan be changed, resulting in a spectral distribution of the dispersed light. The derivation for scattering of light in liquids by Brillouin scattering is rather complex and has been previously reported in great detail [5, 6, 10, 11].

For the purpose of this thesis we are essentially concerned with the normalized correlation function, $\Phi_q(\mathrm{t})$, of the density fluctuations. We will follow a similar derivation as previously shown in Ref. [11]:

$$\Phi_q(t) = \left\langle \frac{\delta\rho_q^*(0)\delta\rho_q(t)}{\delta\rho_q^*(0)\delta\rho_q(0)} \right\rangle, \tag{2.12}$$

where $\delta\rho_q^*(t)$ is the qth component of the density fluctuation of the microscopic number density, $\rho(\mathbf{r}, t)$. The dynamic structure factor, $S(q, \omega)$, is then defined as,

$$S(q,\omega) = S(q) \int_{-\infty}^{\infty} \mathrm{d}t e^{-i\omega t} \Phi_q(t), \tag{2.13}$$

where we have introduced the static structure factor,

$$S(q) = \left\langle \delta\rho_q^*(0)\delta\rho_q(0) \right\rangle = \frac{1}{2\pi}\int_{-\infty}^{\infty} \mathrm{d}\omega S(q,\omega). \tag{2.14}$$

This corresponds to zeroth moment of the dynamic structure factor, $M_S^{(0)}$. In the low q limit, appropriate for light-scattering experiments, the following relation holds for liquids [11]:

$$M_S^{(0)} = S(q \to 0) = \frac{\rho k_B T \chi_T}{M_{\mathrm{mol}}}, \tag{2.15}$$

where M_{mol} is the molecular mass, k_B is the Boltzmann constant, ρ is the mass density and χ_T is the isothermal compressibility. We also recall the second (nonzero) moment of $S(q,\omega)$, which is given by the relation,

$$M_S^{(2)} = \frac{1}{2\pi}\int_{-\infty}^{\infty} \mathrm{d}\omega \omega^2 S(q,\omega) = \frac{q^2 k_B T}{M_{\mathrm{mol}}}. \tag{2.16}$$

An equation of motion for $\Phi_q(t)$ can be written in the form of a generalized Langevin equation [11],

$$\frac{\partial^2 \Phi_q(t)}{\partial t^2} + \omega_0^2(q)\Phi_q(t) + \int_0^t \mathrm{d}t' m_q(t-t')\frac{\partial \Phi_q(t')}{\partial t'} = 0. \tag{2.17}$$

Similarily, in the frequency space, $S(q,\omega)$ can be written as,

$$S(q,\omega) = \frac{2vq^2}{\omega}\mathrm{Im}[\omega^2 - \omega_0(q)^2 - i\omega m_q(\omega)]^{-1} \tag{2.18}$$

The parameter $\omega_0(q)$ introduced above is completely determined once the second sum rule for $S(q,\omega)$ is fulfilled, and it turns out to be

$$\omega_0^2(q) = \frac{(qv)^2}{S(q)} \tag{2.19}$$

In the equations 2.17 and 2.18, we have introduced the second memory functions, $m_q(t)$ and $m_q(\omega)$, which are part of the Zwanzig-Mori expansion of $\Phi_q(t)$ [11]. The advantage of incorporating these memory functions is that they ensure the first two non-zero spectral moments of $S(q,\omega)$ are always respected meaning that specific mathematical properties related to the spectral moments of the function are kept consistent.

According to the different kind of dynamics which can be probed, the (q,ω) space is usually divided into different regions. Within this space, two parameters are defined, those being, the average intermolecular distance denoted as d, and the relaxation time denoted as τ, which influences the process of structural relaxation. Among these, the structural relaxation plays an important role. It is linked to cooperative processes wherein the local arrangement, when perturbed by external or spontaneous fluctuations, undergoes a gradual reorganization towards a new equilibrium configuration. This relaxation phenomenon highlights the complex interplay of many-body effects, setting liquids apart from dilute gases, for example. As a result, it can be considered as a sort of fingerprint of the liquid state. Considering now the parameters d and τ, we can introduce two regions of the (q,ω) space that are relevant for the discussion that follows. The condition $qd \ll 1$ and $\omega\tau \ll 1$ defines the first region of the (q,ω) space where simple hydrodynamics holds. In this specific region, the fluctuations are primarily dominated by collisions. Alterations in the liquids structure are triggered by density fluctuations, and are assumed to occur gradually enough for the system to be treated as being in a state of local thermodynamic equilibrium. In this case, when we take the continuum limit into account, we can develop a set of equations that show the changes of particle number, current density, and energy density across both space and time. The clarity of this treatment becomes evident as we specify certain values for thermodynamic derivatives and transport coefficients. The outcomes of these calculations are represented by the Langevin equation and its associated memory function:

$$m_{q\to 0}(t) = \omega_0^2(q)[\gamma - 1]e^{-D_T q^2 t} + 2\eta_l q^2 \delta(t), \tag{2.20}$$

where $\gamma = C_p/C_v$ is the constant pressure to constant volume-specific heat ratio, $D_T = \kappa/(\rho C_v)$ where κ is the thermal conductivity, and η_l is the kinematic longitudinal viscosity.

If the condition $\omega\tau \ll 1$ is not met within the initial region, and if $qd \sim 1$, one transitions into what is known as the molecular hydrodynamics region [12]. In this region, the molecular dynamics is influenced both by structural and relaxation effects. In relation to the structural effects, they become significant due to their direct influence through the structure factor, $S(q)$. On the other hand, for what concerns the latter, an appropriate viscoelastic model has to be introduced. In fact, if an external disturbance is applied to a liquid system, the observed response depends on the relative duration of the perturbation ω^{-1} as compared to the relaxation time τ. If $\omega\tau \ll 1$, the system can respond to the perturbation, and quickly takes up a new configuration which corresponds to the simple hydrodynamic region previously referred to. If, conversely, $\omega\tau \gg 1$, the system has no time to respond before the perturbation is removed and the preexisting equilibrium state is unchanged; in this situation, the system behaves as a solid, and actually the condition $\omega\tau \gg 1$ can be used to define the purely elastic state. Measurements made in between these two time scales, that is, in the relaxation region, enable one to determine the relaxation time.

The gradual transition from the simple hydrodynamic regime to the molecular regime provides the main rationale for extending the hydrodynamic description. This extension involves maintaining the formal structure of the equations while replacing the thermodynamic derivatives and transport coefficients with functions that can vary in both space (or wavenumber) and time (or frequency). Therefore, Eqn 2.20 can be generalized using the following equation [11, 12],

$$m_q(t) = \omega_0^2(q)[\gamma(q) - 1]e^{-D_T(q)q^2 t} + \zeta_l(q,t), \tag{2.21}$$

where $\gamma(q)$ and $D_T(q)$ are the q-dependent generalizations of the corresponding thermodynamic quantities, and $\zeta_l(q,t)$ is the corresponding q and t dependent generalization of the longitudinal kinematic viscosity. The formulation presented here should be understood as a generalization of the formalism used at low values of q. It is important to note that this generalization does not consider the transverse contributions that are known to affect the density-density dynamics of liquids at high values of q [13, 14]. At sufficiently high q values, the distinction between pure transverse and longitudinal modes in a liquid system starts to become less significant, and the aforementioned transverse contributions become relevant. Equations 2.20 and 2.21 establish a formal relationship between $S(q,\omega)$ and a generalized form of longitudinal kinematic viscosity that depends on both q and ω. Similarly, a connection can be established between $S(q,\omega)$ and the generalized elastic moduli.

In a macroscopic formulation, the elastic moduli are defined as the coupling constants between the components of the (macroscopic) stress tensor and those of the (macroscopic) strain tensor. For an isotropic system, there are two independent elastic moduli: the shear modulus G and the bulk modulus K. The longitudinal modulus M is related to them by the expression $M = K + 4G/3$. The concept of elastic properties is applicable to a fluid system only at high frequencies. At low frequencies, the response of a liquid is predominantly viscous, with the stress tensor being coupled to the rate of strain according to Newton's law. In this case, the shear viscosity coefficient η_s and the bulk viscosity coefficient η_b act as coupling constants. To describe both the elastic and viscous properties of a fluid, it is useful to introduce a frequency-dependent stress-to-strain relation that encompasses the behavior of both solids and fluids in the appropriate limits [15]. This is achieved by introducing the frequency dependent viscosities ($\eta_{s,b}(\omega)$) and elastic moduli G(ω) and K(ω), which are related through the following,

$$G(\omega) = i\omega\eta_s(\omega) \tag{2.22}$$

and

$$K(\omega) = K_0 + i\omega\eta_b(\omega), \tag{2.23}$$

where K_0 is the zero frequency limit of the bulk modulus and is given by the inverse of the adiabatic compressibility κ_s.

The simplest ansatz for the frequency dependence of the viscosity is the one corresponding, in the time domain, to a single exponential decay. This is the basis of the Maxwell theory of viscoelasticity. With the formal connection between the generalized viscosity and elastic moduli contained in Eqs 2.22 and 2.23, we can write the spectral intensity as,

$$I_q(\omega) \propto S_q(\omega) = \frac{S_q M_0}{\pi\omega_B} \frac{M''(\omega)}{[M'(\omega) - \rho\omega^2/q^2]^2 + [M''(\omega)]^2} \tag{2.24}$$

where $S(q)$ is the static structure factor, ρ the mass density, M_0 the relaxed (low-frequency) longitudinal acoustic modulus, $M^*(\omega) = M'(\omega) + iM''(\omega)$ the generalized longitudinal acoustic modulus, and q the exchanged momentum.

In Brillouin spectroscopy the longitudinal acoustic modulus, $M^*(\omega) = M'(\omega) + iM''(\omega)$ can be directly determined from the Brillouin spectra. The first term in this equation is associated with the storage modulus which is the given by ρv^2, where ρ is the mass density and v is the speed of density fluctuations derived earlier in Eqn 2.11. Furthermore, the second term in the longitudinal acoustic modulus is known as the loss modulus and is given by $2\pi\eta f_B$, where η is the apparent viscosity and f_B is the frequency shift of the spectral Brillouin peaks. Moreover, the apparent viscosity η, is related to the full width at half maximum (FWHM) by [16],

$$\Gamma_B = \frac{1}{2\rho}\left[\frac{4}{3}\eta_s + \eta_b + \frac{\kappa}{C_p}(\gamma - 1)\right]q^2 \tag{2.25}$$

where $\eta_{s,b}$ is the shear and bulk viscosity, κ is the thermal conductivity of the liquid, ρ is the density of the liquid, and $\gamma = C_p/C_v$ is the ratio of specific heat at constant pressure C_p to the specific heat at constant volume C_v. The last term on the right is neglected since $\gamma - 1 \simeq 0$ [17]. Taking this into consideration we can rewrite Eqn 2.25 as the following:

$$\Gamma_B = \frac{1}{2\rho}[\frac{4}{3}\eta_s + \eta_b]q^2 = \frac{1}{\rho}\eta\frac{2\pi^2 n^2}{\lambda_i^2} \tag{2.26}$$

where $\eta = \frac{4}{3}\eta_s + \eta_b$ is the apparent viscosity and $q = \dfrac{4\pi n}{\lambda_i}$ where n and λ_i are the refractive index and wavelength of incident light, respectively.

To summarize, Brillouin spectroscopy is a useful technique for the study of molecular interactions in a fluid. The raw data obtained from the spectral peaks can yield important quantities of a fluid such as viscosity, as discussed, but also on information on damping of sound waves in a material. Using the values of frequency shift and FWHM obtained from the Brillouin spectra, as well as the sound wave velocity v obtained in Eqn. 2.10, it is possible to calculate the frequency independent sound absorption α/f^2 given by [5],

$$\frac{\alpha}{f^2} = \frac{\Gamma_B}{2vf_B^2}. \tag{2.27}$$

Overall, the spectral shift and shape is determined by a number of quantities such as transport coefficients, elastic moduli, and relaxation times in liquids. Understanding the behaviour of various fluids can lead to a better understanding of these quantities [18].

Bibliography

[1] L. Brillouin. Diffusion of light and x-rays by a transparent homogeneous body. *Ann. Phys*, 17(2):88–122, 1922.

[2] J. Dil. Brillouin scattering in condensed matter. *Reports on Progress in Physics*, 45(3):285, 1982.

[3] K. Koski and J. Yarger. Brillouin imaging. *Applied Physics Letters*, 87(6):061903, 2005.

[4] T. Kuznetsova, M. Starodubtseva, N. Yegorenkov, S. Chizhik, and R. Zhdanov. Atomic force microscopy probing of cell elasticity. *Micron*, 38(8):824–833, 2007.

[5] I. Morgan. *Brillouin Scattering Studies in Simple Liquids, Oxygen and Nitrogen.* PhD thesis, Memorial University of Newfoundland, 1976.

[6] R. Mountain. Thermal relaxation and brillouin scattering in liquids. *Journal of Research of the National Bureau of Standards. Section A, Physics and Chemistry*, 70(3):207, 1966.

[7] G. Benedek and T. Greytak. Brillouin scattering in liquids. *Proceedings of the IEEE*, 53(10):1623–1629, 1965.

[8] G. Patterson and P. Carroll. Light scattering spectroscopy of pure fluids. *The Journal of Physical Chemistry*, 89(8):1344–1354, 1985.

[9] J. Vaughan and J. Randall. Brillouin scattering, density and elastic properties of the lens and cornea of the eye. *Nature*, 284(5755):489–491, 1980.

[10] D. Hanlon. *Temperature dependence of acoustic properties of natural snail mucus by Brillouin spectroscopy.* MSc Thesis, Memorial University of Newfoundland, 2020.

[11] L. Comez, C. Masciovecchio, G. Monaco, and D. Fioretto. Progress in liquid and glass physics by brillouin scattering spectroscopy. In *Solid state physics*, volume 63, pages 1–77. Elsevier, 2012.

[12] J. Boon and S. Yip. *Molecular hydrodynamics.* Courier Corporation, 1991.

[13] V. Giordano and G. Monaco. Fingerprints of order and disorder on the high-frequency dynamics of liquids. *Proceedings of the National Academy of Sciences*, 107(51):21985–21989, 2010.

[14] F. Sette, M. Krisch, C. Masciovecchio, G. Ruocco, and G. Monaco. Dynamics of glasses and glass-forming liquids studied by inelastic x-ray scattering. *Science*, 280(5369):1550–1555, 1998.

[15] R. Zwanzig and R. Mountain. Title of the article. *Journal of Chemical Physics*, 43(10):4464, 1965.

[16] B. Berne and R. Pecora. *Dynamic Light Scattering: with Applications to Chemistry, Biology, and Physics.* Courier Corporation, 2000.

[17] J. Rouch, C. Lai, and S. Chen. Brillouin scattering studies of normal and supercooled water. *The Journal of Chemical Physics*, 65(10):4016–4021, 1976.

[18] C. Montrose, V. Solovyev, and T. Litovitz. Brillouin scattering and relaxation in liquids. *The Journal of the Acoustical Society of America*, 43(1):117–130, 1968.

Chapter 3

Methods & Materials

3.1 Sample Preparation

3.1.1 Snail Mucus

Figure 3.1 shows a prepared sample of transparent viscous natural snail mucus used in the present study. The mucus was purchased from an commercial source and its initial composition was unknown. Section 3.5.3 below outlines how we determine the approximate protein and water concentration of the natural snail mucus. The mucus was stored in a sealed container at room temperature until a sample was required for experimental purposes. Periodic testing of the mucus was conducted to confirm that there had been no degradation, which was achieved by comparing Brillouin spectra collected with the original spectra. Approximately 2 ml of mucus was carefully extracted using a syringe from the main container and was added the glass sample cell. The sample cell was made of a 15 cm long glass tube with an outer diameter of 6 mm and an inner diameter of 4 mm, sealed at one end using

Figure 3.1: Visual of natural snail mucus used in this work. Mucus is clear, viscous and some air bubbles are shown. Not shown in this schematic is the Teflon cap used to seal the top.

glassblowing. Mucus was added to the sample cell by applying gentle pressure to the syringe plunger, causing the mucus to slowly flow from the syringe barrel through the tube and into the sample cell. Employing this slow extrusion technique served the purpose of minimizing the formation of air bubbles in the mucus during loading. To account for expansion of the liquid upon cooling, particularly near and at the mucus freezing temperature, the cell was only filled to half of its capacity, containing approximately 1 cm^3 of mucus. Once the loading was completed, the top of the sample cell was sealed using a Teflon cap secured with epoxy. Following the loading process, the glass sample cell was placed in a sample holder (discussed in Sec. 3.3) in preparation for Brillouin scattering experiments.

3.1.2 Diluted Samples

The diluted snail mucus samples utilized in this study were prepared by combining natural snail mucus with ultra pure water. Using a syringe, 1 ml of mucus was extracted from the parent container and transferred to a glass sample cell, which was sealed at one end, as previously stated. Subsequently, ultra pure water was added to the cell in increments of 0.5 ml for each dilution. After the addition of ultra pure water, a stirring stick was used to mix the mucus water solution for a duration of 10 minutes. We ensured by visually inspected the sample that no remnants were left from the stirring stick. This standardized procedure was followed for all dilutions to maintain uniformity and significantly reduce the amount of bubbles in the sample. Following the mixing process, the samples were left undisturbed for at least 6 hours to allow the solution to equilibrate. It is important to note that the glass sample cell had certain physical limitations, restricting the maximum amount of water that could be added to 3 ml. Additionally, an alternative sample was prepared by initially adding 0.5 ml of mucus and subsequently adding 1.5 ml of water to the mucus. In total there were four dilutions summarized in Table 3.1.

Table 3.1: Summary of diluted mucus samples used in this work.

Dilution #	Amount of Water (ml)	Amount of Mucus (ml)	Total Volume (ml)
1	0.5	1.0	1.5
2	1.0	1.0	2.0
3	1.5	1.0	2.5
4	1.5	0.5	2.0

3.1.3 Dehydrated Mucus

To prepare the dehydrated mucus, approximately 2 ml of natural snail mucus was added to a clear cuvette, leaving one end unsealed. The mucus was then subject to dehydrate while collecting room temperature Brillouin spectra. Unfortunately, temperature dependent Brillouin spectroscopy could not be conducted due to physical limitations with the temperature controlled sample chamber.

3.1.4 Bacterial Cell Lysate

An autoclave was used to sterilize a 0.5 L flask that contained 0.75 L of Lysogeny Broth (LB) medium, which is made up of 5 g of yeast extract, 10 g of sodium chloride, and 10 g of tryptone citefisher. The flask was sealed with a sponge stopper and aluminium foil. Overnight cultures of *E. coli* JM109 were created by inoculating 0.75 L of LB media with 0.01 L aliquots of frozen glycerol cell stocks after the broth had warmed to room temperature. The inoculated cultures were placed in a 30°C incubator with shaking at 150 rpm, protected with a foam stopper. Six 4L flasks, each containing 1 L of LB media, were pre-warmed to 37°C. The following day, the flasks were inoculated with 1 mL of overnight culture per 0.1 L of fresh supplemented media and incubated at 37°C with centrifugation at 175 rpm. Cells were harvested during the log phase, typically at an absorption of 600 nm (A_{600}) ranging from 0.6 to 1.0. The harvested cells were then centrifuged at 5670 times the force of gravity. for 20 minutes at 4°C. The resulting pellet was subjected to three cycles of the French press method at a pressure of 10,000 psi and maintained at 4°C to generate the lysed cells. The French press cycle involved forcing the pellet through a small valve under high pressure. Typically, the volume of cell lysate obtained was approximately 30 mL. Once freeze dried, the volume reduced to approximately 5 mL. The lyophilized cell lysate was stored in a 15 mL falcon tube at -20°C for further use. A simplified overview of the cultivation process can be viewed in Table 3.2.

Table 3.2: Simplified Procedure Overview for Culturing and Harvesting *E. coli* Cells

Step	Action
1	Fill 500 mL flask with 75 mL of LB media (5g yeast extract, 10g NaCl, 10g tryptone). Seal with sponge plug and aluminum foil. Autoclave for sterilization.
2	Inoculate 75 mL LB media with 1 mL aliquots of frozen glycerol cell stocks. Incubate at 30°C with shaking (150 rpm).
3	Pre-warm six 4L flasks with 1L LB media to 37°C. Inoculate flasks with 1 mL of overnight culture per 100 mL of fresh media with supplements. Incubate at 37°C with centrifugation (175 rpm).
4	Harvest cells during log phase (A_{600} 0.6-1.0). Centrifuge at 5670 g for 20 min at 4°C. Subject pellet to 3 cycles of French press at 10,000 psi and 4°C to generate cell lysate.
5	Store resulting cell lysate in a 15 mL falcon tube at -20°C for further use.

3.2 Brillouin Spectroscopy Setup

3.2.1 Brillouin Scattering Geometry

Brillouin spectra throughout this work were collected using the optical setup shown in Figure 3.2. A 180° backscattering geometry with a diode-pumped frequency-doubled Nd:YVO_4 solid-state laser (single-mode Coherent Verdi-2) emitting a vertically polarized beam of light with a center wavelength of 532 nm and a bandwidth of 10 MHz with output power of 2W was used as the incident light source. The 2W laser beam initially goes through a variable neutral density filter ($VNDF_1$) to reduce beam power before going through a half-wave plate (HWP) to change the polarisation of the light from the vertical plane to the horizontal plane. The beam is then incident on a beam splitter (BS) with the reflected portion of the light being used as a reference beam and the transmitted portion being used as the sample probe beam.

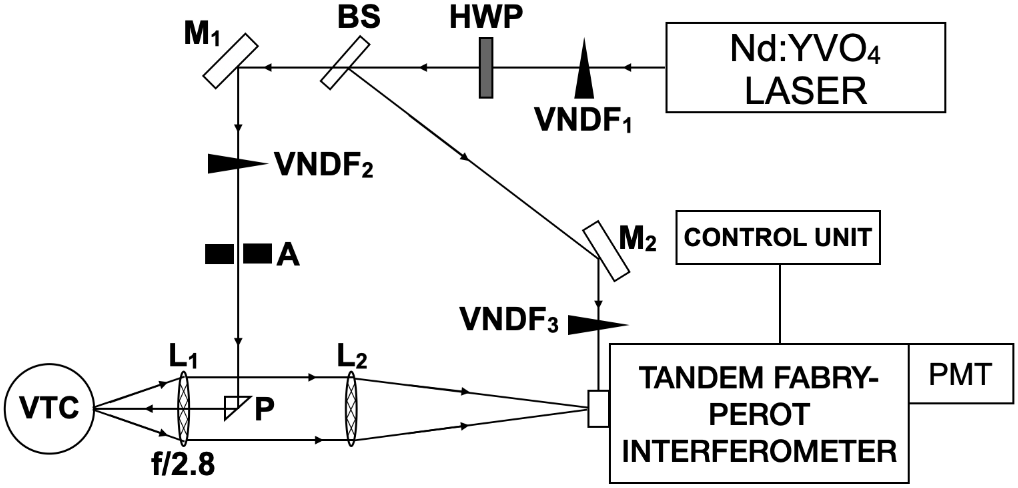

Figure 3.2: Optical setup for Brillouin scattering used in this study. HWP - half wave plate, BS - beam splitter, M - mirror, VNDF - variable neutral density filter, A - aperture L- lens, P- prism, VTC - variable temperature chamber, PMT - photomultiplier tube.

The path of the probe beam, which had been transmitted through the beam splitter, was redirected by 90° using a front surface mirror (M_1). It passed through a $VNDF_2$, which served to reduce the beam power. The beam power in this work was 100 mW. The beam underwent internal reflection by a prism (P), directing it on a path parallel to the original beam. The probe beam was then focused by a 5 cm camera lens (L_1) onto the sample enclosed by the variable temperature chamber (VTC). Some of the scattered light was collected and collimated by the same camera lens, with the size of the collection cone being set by adjusting the f-number (f/#). These experiments used an f/# of 2.8. This collimated scattered light passed through a second lens (L_2) with a focal length of 40 cm, focused the scattered light onto the input pinhole of 450 μm on the tandem Fabry-Perot interferometer.

The path of the beam, after being redirected by the BS, functioned as a reference beam and was directed towards a six-pass tandem Fabry-Perot interferometer using a front-surface mirror (M_2). Before entering the interferometer, the reference beam

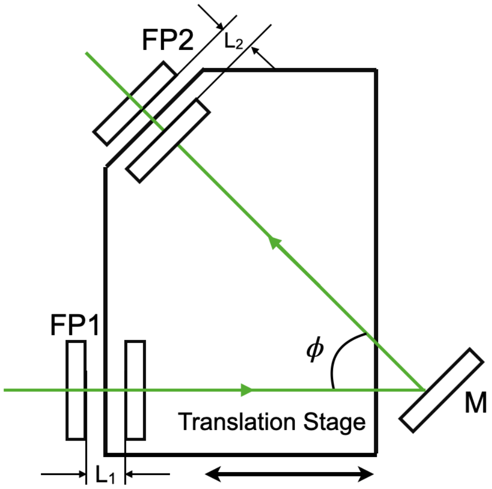

Figure 3.3: Schematic of a tandem Fabry-Perot interferometer. The light passes through one Fabry-Perot optical cavity (FP1), is reflected by a mirror (M), and then passes through a second Fabry-Perot optical cavity (FP2). L_1 and L_2 are the spacings of the optical cavities of FP1 and FP2, respectively. Figure adapted from Ref. [1].

passed through an aperture (A) and a variable neutral density filter ($VNDF_3$) that allowed for adjustment of the power. This beam played a vital role in maintaining the alignment of the interferometer. Furthermore, in conjunction with a shutter system inside the interferometer, it prevented saturation of the photomultiplier tube (PMT) while scanning the section of the scattered light spectrum (collected from the sample) that contained highly intense elastically scattered light.

3.2.2 Tandem Fabry-Perot Interferometer

Scattered light collected in this work was analyzed by a six-pass tandem Fabry-Perot interferometer manufactured by JRS Scientific Instruments. A schematic of the apparatus can be seen in Fig 3.3.

A simple Fabry-Perot interferometer consists of an optical cavity made by two partially reflective parallel planar mirrors. Light that enters the cavity undergoes multiple reflections and, due to interference effects, transmission through the etalon consists of a series of peaks, each corresponding to the frequency for which there is constructive interference. Each transmission peak is due to a different order of interference. Assuming that the light is normally incident on the cavity, constructive interference occurs when the spacing between the mirrors is [2],

$$L = \frac{m\lambda_m}{2} = \frac{mc}{2f_m} \tag{3.1}$$

Here, m represents an integer denoting the order of constructive interference, c denotes the speed of light in vacuum, λ_m represents the wavelength corresponding to a specific order, and f_m denotes the frequency associated with that order. The cavity between mirrors is filled with air. The frequency of the transmitted light can be expressed as follows:

$$f_m = \frac{mc}{2L} = mf_{FSR} \tag{3.2}$$

where f_{FSR} is the difference between successive resonant frequencies of transmitted light, called the free spectral range (FSR).

As depicted in Figure 3.3, the incident light in the instrument passes through two separate Fabry-Perot optical cavities. When these two cavities are combined in tandem, the resulting output represents a combination of each individual Fabry-Perot interferometer. The spacings of the two optical cavities, denoted as L_1 and L_2, are related by $L_2 = L_1 \cos\phi$, with different values within the range of $0 \le \phi \le \pi/2$. To enable simultaneous adjustment of both cavity spacings, one mirror from each optical cavity is positioned on the same translation stage. This synchronization ensures that the cavities are scanned concurrently when the translation stage is moved. By superimposing the outputs from both cavities, only frequencies that satisfy the following

$$f_m = m\frac{c}{2nl\cos\theta} \tag{3.3}$$

are transmitted. Here m is any integer, n is the refractive index of the medium between the Fabry-Perot mirrors, and l is the mirror spacing and θ is the angle of incidence. Note that $n = 1$ in this work since the medium between the Fabry-Perot plates is air and $\theta = 0^\circ$ since the light is incident normally on the Fabry-Perot mirrors. The tandem Fabry-Perot interferometer offers advantages such as improved transmission contrast and the elimination of ambiguities that may arise from overlapping transmission orders [1].

Furthermore, as previously mentioned, the scanned scattered light was directed through an output pinhole with a diameter of 700μm, and then detected by a photomultiplier tube (PMT). As the tandem Fabry-Perot interferometer scanned across the frequencies of the scattered light, the resulting photon counts were transmitted to a computer. The computer processed the data and displayed it as an intensity versus frequency spectrum.

3.3 Temperature Controlled Sample Chamber

3.3.1 Overview

This section describes the temperature controlled sample chamber used in the study. The cell design is depicted in Figure 3.4 and has been previously discussed in detail in a Ref. [3]. Here, we will provide a brief overview of the system.

To facilitate efficient heat transfer, the sample holder was constructed using brass due to its excellent heat conductivity. Thermal paste was applied to establish good thermal contact between the glass sample cell and the sample holder. This ensured that the sample cell holder could reach the desired temperature. Figure 3.5 illustrates the sample holder, which features two interchangeable holes, each with a diameter of 3/8”. These holes can hold either a glass vial containing a sample or a resistor. In order to ensure the sample holders ability to reach the required temperature, different resistors were tested for their heating capacities. By selecting the appropriate resistor, it was ensured that the sample holder could achieve the desired temperature. The 50 Ω resistor heated up the fastest and was capable of reaching temperatures of at least 50°C. A DT-670 series silicon diode from Lakeshore Cryotronics was used as a temperature sensor. The temperature, accurate to about ± 0.5 K, was obtained from the diode voltage using a standard calibration curve provided by Lakeshore Cryotronics. Both the resistor and silicon diode were connected through an electrical feed-through. To ensure optimal temperature control of the sample holder, the sample chamber was evacuated using a roughing pump capable of achieving pressures as low as 1×10^{-3} Torr. The sample cell holder shown in Figure 3.4 and 3.5, featured cooling tubes that allowed antifreeze to flow through it which allowed for cooling using the circulating bath provided by NESLAB Instruments. The circulating bath was also capable of heating the sample holder via an internal heater in the circulating bath. This feature was used mainly to ensure temperature was maintained.

The temperature of the sample cell holder is controlled by use of a heater and cooling bath system, using a cryogenic temperature controller from Lakeshore Cryotronics. Depending on the desired temperature of the experiment, either the heater or the cooling bath is initially turned on. Once the desired temperature is reached, the heater and refrigeration bath will work together to stabilize the sample cell holder. If

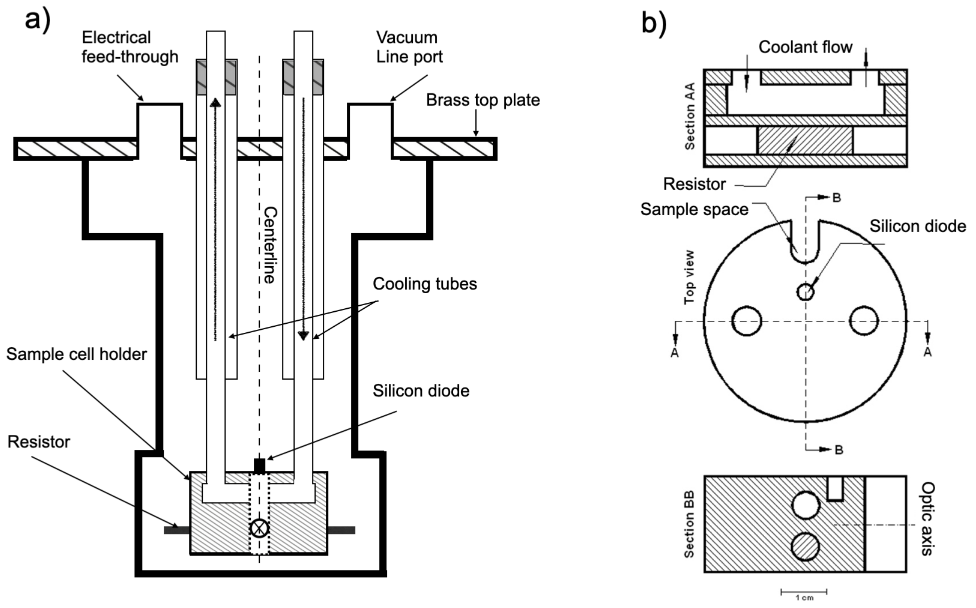

Figure 3.4: a) Schematic of the custom-built temperature-controlled sample chamber used in the present work with sample cell holder in place. b) Machine drawing of the sample cell holder shown in a).

the sample cell holder surpasses the desired temperature (voltage set-point) the heater will turn off and the cooling bath will turn on. Similarly, if the sample cell holder gets too cold, the bath will turn off and the heater will turn on. Fig 3.6 shows a simple flow chart illustrating the process that allows the desired temperature to be reached. It should be noted that both the ***Heating*** and ***Cooling*** branches of the flow chart are in a constant loop with one another to ensure the desired temperature is stable. This is because there are fluctuations in the temperature and cooling procedure.

3.3.2 Determining Accuracy of Temperature Cell

Accuracy of the temperature controlled sample holder was measured by collecting Brillouin spectra of water between $-5^{\circ}\mathrm{C} \leq T \leq 5^{\circ}\mathrm{C}$, being sure to get plenty of many temperature values near $T = 0^{\circ}\mathrm{C}$. The temperature at which spectral peaks due to

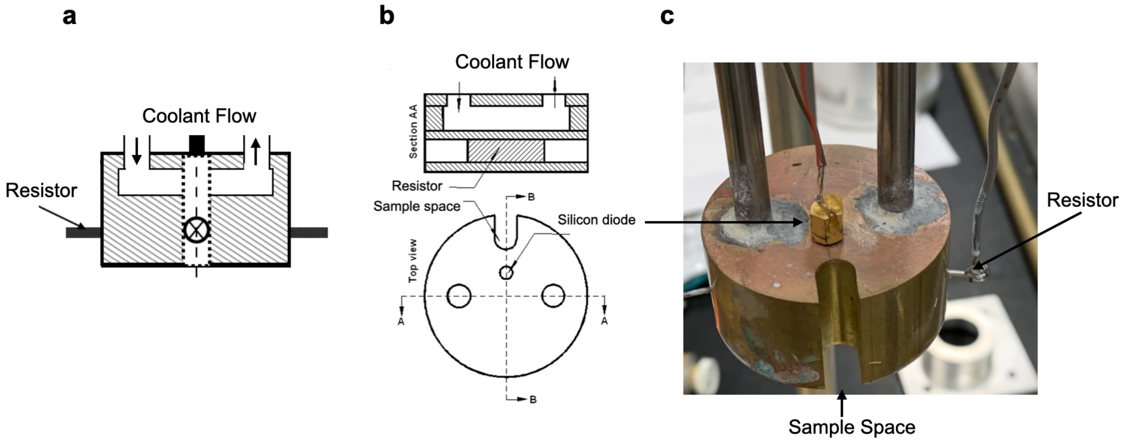

Figure 3.5: Schematic representation of the brass sample holder used in the variable temperature cell, showing: a) General schematic of the sample cell holder, b) Cross-sectional view of the holder, including a top-down perspective, and c) Actual image of the sample cell holder.

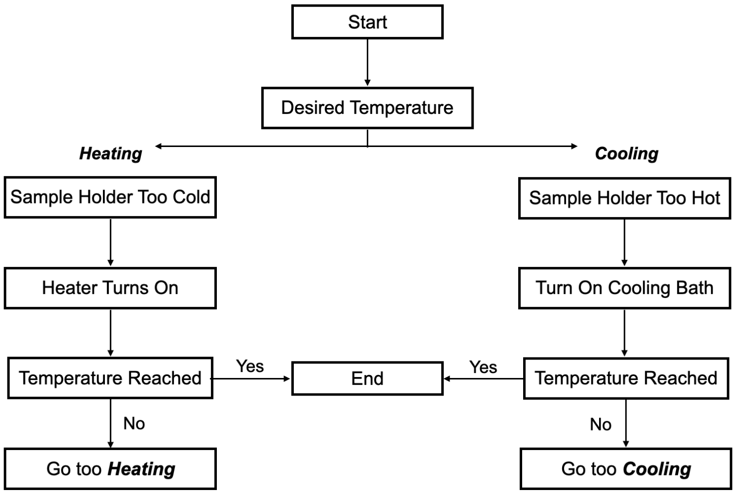

Figure 3.6: Simple flowchart showing the procedure for heating and cooling the temperature cell.

ice appear was deemed the freezing point of water. The uncertainty was estimated by comparing the temperature at which ice was present in the Brillouin spectra which occured at -0.4°C, and the freezing point of water which has previously been determined to be at $T = 0^{\circ}$C [4]. Consequently the uncertainty in the temperature cell was determined to be ± 0.4°C.

3.4 Analysis of Brillouin Spectra

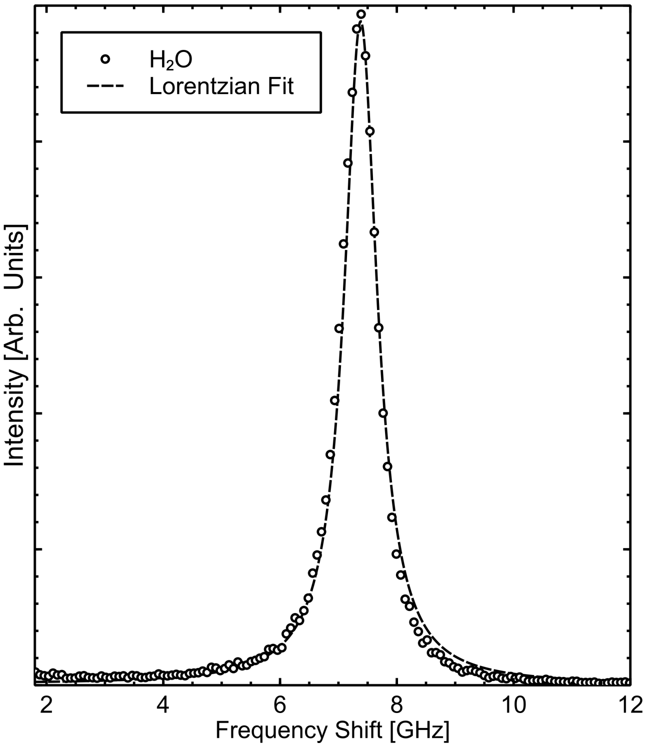

Figure 3.7: a) Representative Brillouin light scattering spectrum collected from water at a temperature of 22°C. Empty symbols: experimental data; dotted curves: Lorentzian fit. b) Simplified Brillouin spectrum of a liquid with the bulk longitudinal (L) modes are symmetric about the central peak (C) attributed to elastic scattering.

Figure 3.7a) shows the anti-Stokes peak from a sample Brillouin spectrum collected from water. The light spectra were characterised by a series of peaks created by Stokes and anti-Stokes scattering from acoustic phonons that are symmetric around an extremely intense central peak (C) assigned a frequency shift of zero, Fig. 3.7b) shows a typical Brillouin spectrum for a fluid. As previously stated, the reference beam, which has the same frequency as the elastically scattered light, causes the centre peak in the spectra. As a result, the frequency shifts of the Brillouin peaks detected correlate with the frequency of the investigated acoustic phonons.

In order to determine, accurately, the frequency shift and FWHM of the observed Brillouin peaks, spectral data were fit to mathematical functions using a self written code in Python [5] (See Appendix A), using the LMfit package [6]. Brillouin peaks from liquids typically behave like Lorentzian functions, therefore both the Stokes and Anti-Stokes peaks were fitted to a Lorentzian [7]. Figure 3.7a shows the result of such a fit and the accuracy is representative for all spectra analyzed throughout this work.

3.5 Infrared Spectroscopy

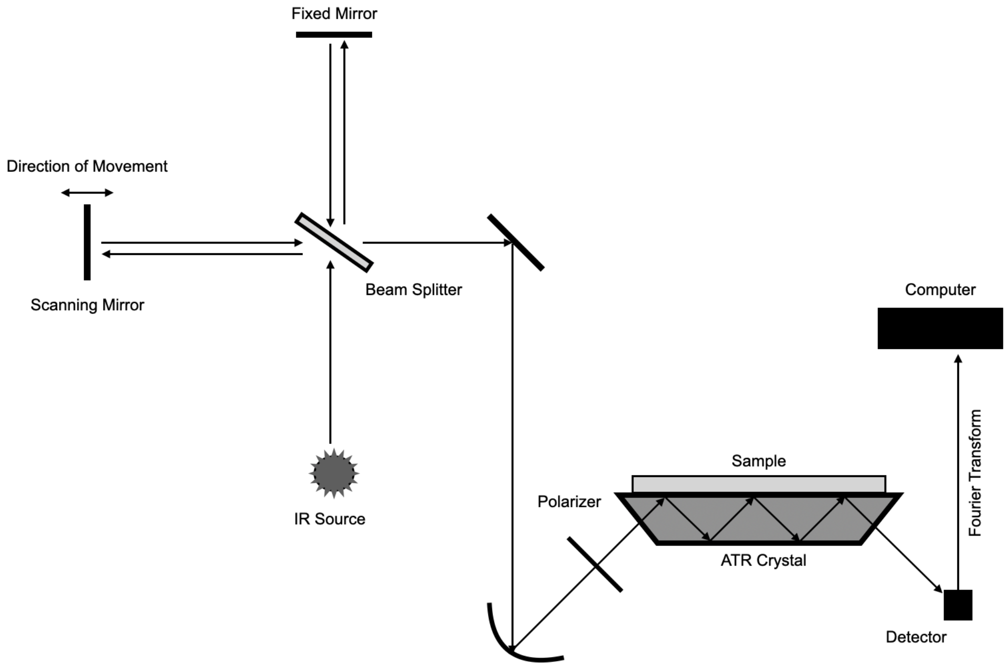

Figure 3.8: A schematic representation of the FTIR spectrometer demonstrating the use of a Michelson interferometer with an ATR attachment. The initial beam is produced by the infrared source. The beam splitter separates the initial IR beam into two beams with half the intensity of the original source. The fixed and scanning mirrors are utilised to create a path difference between the two beams, resulting in interference. The interfered infrared beam is incident on a sample, and the resulting interferogram is recorded at the detector.

3.5.1 Overview

Fourier Transform Infrared (FTIR) spectroscopy, a type of vibrational spectroscopy, has been effective in understanding the structure of proteins in aqueous solutions previously [8–10]. This technique allows for the identification and characterisation of numerous chemical groups which makes it valuable in understanding the structure of complicated liquid systems and is typically used in conjunction with other spectroscopic techniques in order to analyse various samples. It is based on the theory of infrared (IR) spectroscopy, which evaluates the absorption or transmission of infrared radiation by a material.

Figure 3.8 shows a schematic diagram of a FTIR spectrometer that makes use of a Michelson interferometer. A broadband thermal source generates the infrared beam, which behaves similarly to a black-body over the wavenumber region of interest (Mid-IR: 4000 cm^{-1} - 400 cm^{-1}, or Far-IR: 400 cm^{-1} - 80 cm^{-1}). The infrared beam is directed into the Michelson interferometer, which is made up of a beam splitter, a fixed mirror, and a scanning mirror. The beam splitter divides the beam into two equal-intensity beams. Both the fixed and movable mirrors redirects the beams back towards the beam splitter. The scanning mirror oscillates at a frequency determined by the control software, which is referred to as the mirror speed. A path difference is formed by moving one mirror, causing the beams to interfere with one another.

Most commonly, FTIR data are collected by either transmission (absorption) or attenuated total reflectance (ATR) methods in the Mid-IR range (4000 - 400 cm^{-1}). This work was done utilising the ATR-FTIR method, a popular analytical technique for identifying and characterising diverse chemical substances (see Fig. 3.8 for setup). It works on the basis of infrared (IR) spectroscopy, which assesses a sample absorption or transmission of infrared radiation. The ATR technique employs the application of a crystal prism, such as a diamond or zinc selenide, in contact with the sample. The infrared radiation is focused at a precise angle onto the prism, where it is internally reflected numerous times where some IR radiation is absorbed each time the beam is reflected from the interface between the sample and prism. At the interface, an evanescent wave, penetrates the sample normal to the crystal [11, 12]. As with other

IR spectroscopic measurements, specific frequencies that correspond to the vibrational modes of the sample are absorbed. The remaining beam passes out of the ATR attachment and is measured by the spectrometer, again as an interferogram. A Fourier transform results in the sample spectrum. When compared to typical transmission IR spectroscopy, this approach produces a substantially greater signal-to-noise ratio [11, 12].

ATR-FTIR is particularly useful for the analysis of samples that are opaque or difficult to prepare in a thin film, such as powders, liquids, and solid samples with irregular surfaces [12]. It is also a useful technique for the analysis of surfaces and interfaces, as it can provide information about the chemical composition and thickness of thin films. ATR-FTIR has a wide range of applications in various fields, including chemistry, biology, material science, and environmental science. It is used in the analysis of polymers, biomolecules, pharmaceuticals, and many other materials [13]. All ATR data presented in this thesis were collected using a Bruker Vertex 70V spectrometer, equipped with a Platinum Diamond ATR attachment (ATR). Additionally, spectra was collected using 32 scans and a 4 cm^{-1} resolution in the Mid-IR range (4000 - 400 cm^{-1}).

3.5.2 Theory

Every substance has its own vibrational signature, and even atoms in solids are constantly moving due to thermal vibration. The bending and stretching of molecules such as oxygen (O) and hydrogen (H) in water and aqueous systems involving water and polymers can be probed, and the characteristic frequency of these vibrational modes measured by the frequencies of infrared radiation absorbed by, and causing vibrations in the material [11, 12]. These vibrational mode energies are affected by the local environment, and any change to the system will influence the system will result in different vibrational mode frequencies. This is especially true for aqueous solutions where the amount of water is increasing or decreasing or the type of protein is changing accordingly. Identifying these differences in vibrational mode energies through the use of IR spectroscopy is useful in the study protein-water systems because it makes it possible to note changes in the water content and can give information on the concentration of proteins present.

The fundamental nature of molecular vibrations can be understood using a basic diatomic mass and spring model where the atoms have some mass M and the chemical bond between atoms can be represented as spring with some spring constant K. This system will have potential energy $U(q) = \frac{1}{2}Kq^2$, where K is the spring constant and q is the displacement of atoms in the model. The energy of the system can be solved using the time-independent Schrödinger equation,

$$-\frac{\hbar^2}{2M}\frac{\partial^2\psi}{\partial q^2} + U(q)\psi = E\psi \tag{3.4}$$

which results in quantized energies of the vibrations, E_n,

$$E_n = (n + \frac{1}{2})h\nu \tag{3.5}$$

where n is the vibrational quantum number, $\hbar$ is the Planck constant, and ν is the vibrational frequency of the diatomic system, ν is given by $\frac{1}{2\pi}\sqrt{\frac{K}{\mu}}$, where μ is the reduced mass for a diatomic system. The physics governing vibrations in materials is essentially the same for all states of matter, with the fundamental principles of vibrational energy states remaining consistent.

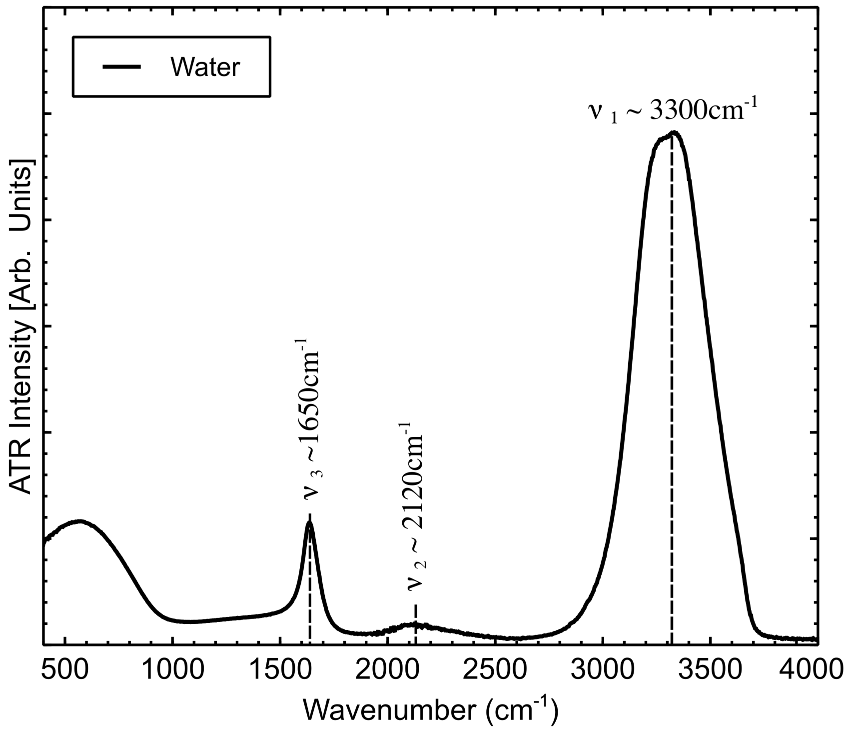

Figure 3.9: Representative ATR-FTIR spectra ($4000cm^{-1}$ - $400cm^{-1}$) for normal H_2O collected at room temperature. Characteristic peaks due to bending (ν_2 and ν_3) and stretching (ν_1) are labelled.

Figure 3.9 depicts typical ATR-FTIR data for H_2O. Material structural changes are deduced by evaluating the FTIR spectrum for differences in peak positions, shapes, widths, absolute and relative intensities. Peak positions correspond to vibrational mode energies, which vary depending on the atoms involved and their configuration in both the local environment and over longer range ordering [11, 12, 14]. The peak intensity in ATR-FTIR spectroscopy is determined by various parameters, including sample concentration, light path length through the sample, and molecule molar absorptivity [12, 15, 16].

3.5.3 Determination of Protein Concentration

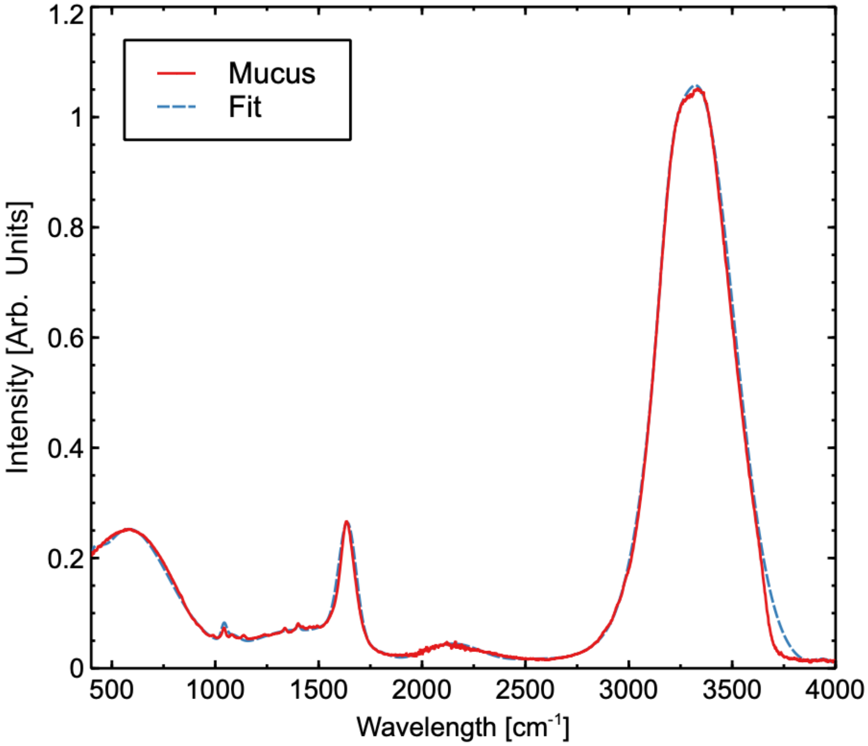

Figure 3.10: Representative ATR-FTIR spectra (4000cm^{-1} - 400cm^{-1}) for diluted snail mucus collected at room temperature. Dashed line is the sum of Gaussian fits for each absorbance bands.

Previous research has indicated that an accurate concentration measurement can be achieved by comparing the integrated intensity of water with that of an unidentified substance containing water [17]. The intensity of the absorbance peaks provides insight into the abundance of molecules that absorb infrared (IR) radiation [14]. To determine the integrated intensity, absorbance bands corresponding to water in the mucus samples were fitted to the Gaussian peaks as shown in Fig. 3.10 and then compared to the same absorbance bands observed in water (see Fig. 3.9). The full width at half maximum (FWHM) for the ν_1 mode generally decreases with decreasing concentration, the ν_2 mode remains relatively constant across most concentrations, and the ν_3 mode increases with higher concentrations when the peak is not observed.

It is important to note that in ATR-FTIR spectra, the intensity of the absorption band directly correlates with the concentration of the absorbing species in the sample. Higher concentrations result in stronger absorption bands and consequently higher peak intensities in the spectrum [14].

3.6 Molecular Dynamics

3.6.1 Overview

Molecular dynamics (MD) is a computational method for simulating the motion of atoms and molecules over time. It is a powerful tool for studying the properties of materials and biological systems at the atomic and molecular level [18]. MD simulations have been used to study a wide range of systems, including materials, biomolecules, and fluids. For example, MD simulations have been used to study the mechanical properties of materials such as ceramics and metals, to investigate the behavior of liquids and gases, and to study the dynamics of biological systems such as enzymes and protein complexes [19–21]. This current work uses MD simulations to study bulk properties such as sound velocity, bulk modulus and viscosity as a function of temperature of protein water system.

3.6.2 Theory

In MD simulations, the equations of motion are numerically solved for a system containing N_p atoms. For any given particle the equation of motion is,

$$\mathbf{f_i} = m_i \ddot{\mathbf{r}}_\mathbf{i}, \tag{3.6}$$

where m_i represents the mass of atom i, $\ddot{\mathbf{r}}_\mathbf{i}$ denotes the acceleration of atom i, which is the second derivative of the position vector $\mathbf{r_i}$ with respect to time t, and $\mathbf{f_i}$ denotes the force acting on atom i due to all other atoms in the system. The force exerted on atom i by atom j is given by,

$$\mathbf{f_{ij}} = -u'(r_{ij}) \frac{\mathbf{r_{ij}}}{r_{ij}} \tag{3.7}$$

where the displacement vector from atom i to atom j is given by $\mathbf{r_{ij}} = \mathbf{r_j} - \mathbf{r_i}$, and r_{ij} denotes the distance between atom i and atom j. Additionally, the derivative of the potential $u(r_{ij})$ will vary depending on the types of atoms present nearby. The net force acting on atom i is obtained by summing over all pairs of atoms in the system.

$$\mathbf{f_i} = \sum_{j \neq i}^{N_p} \mathbf{f_{ij}}. \tag{3.8}$$

By solving Equation 3.6 for all atoms in the system, we can determine the positions $\mathbf{r}$ and velocities $\mathbf{v}$ of each atom as functions of time t, given their initial values. Within this study, the "leap-frog" algorithm has been employed to numerical solve for $\mathbf{r}$ and $\mathbf{v}$ in such a way that these quantities are half a step away from each other (see Fig. 3.11 for visual aid). This algorithm numerically solves for $\mathbf{r}$ and velocities $\mathbf{v}$ in such a way that one quantity is half a time step from the other This algorithm is best visualized as shown in Figure 3.11.

Mathematically the algorithm takes the form,

$$\mathbf{v}\left(t + \frac{\delta t}{2}\right) = \mathbf{v}\left(t - \frac{\delta t}{2}\right) + \delta t \mathbf{f_i}(t) / m_i \tag{3.9}$$

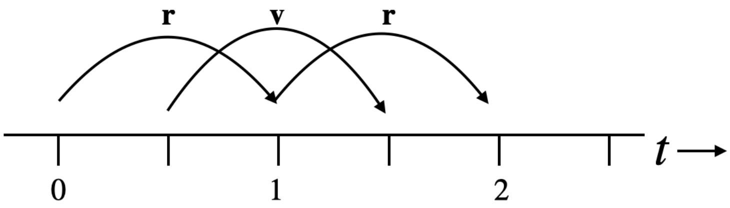

Figure 3.11: Schematic of the leapfrog integrator used for MD simulations.

$$\mathbf{r}(t + \delta t) = \mathbf{r}(t) + \delta t \mathbf{v}\left(t + \frac{\delta t}{2}\right) \tag{3.10}$$

where δt is the time step. The current velocity is then given by,

$$\mathbf{v}(t) = \frac{1}{2}\left(\mathbf{v}\left(t + \frac{\delta t}{2}\right) + \mathbf{v}\left(t - \frac{\delta t}{2}\right)\right) \tag{3.11}$$

It is now possible to use Eq. 3.11 to find the kinetic energy of the system,

$$K(t) = \frac{1}{2}\sum_{i=1}^{N_p} m_i v_i^2. \tag{3.12}$$

Furthermore, the system potential energy is given by,

$$U(t) = \sum_{i=1}^{N_p-1}\sum_{j>1}^{N_p} u(r_{ij}) \tag{3.13}$$

where in this case, $u(r_{ij})$ will be given by either Eq. 3.15 or Eq. 3.16. We require $U(t)$ in order to find the total energy of the system,

$$E(t) = U(t) + K(t). \tag{3.14}$$

In conclusion, Molecular Dynamics (MD) simulations generate new microstates by computing forces that drive the systems temporal evolution. MD is commonly employed to investigate the dynamics of a variety of systems.

3.6.3 Water Models

As mentioned previously, molecular dynamic (MD) simulations can provide valuable insights into the properties and dynamics of complex systems, including the interactions between molecules and their environment [18]. In order to accurately represent the behavior of water in MD simulations, it is important to use a suitable model for the water molecules.

There are several different models that can be used to represent water in MD simulations, and the choice of model will depend on the specific goals of the simulation and the level of detail that is required. There are a number of different water models commonly used; they are typically defined by the number of their interaction points (*i.e,* 3-site, 4-site, and 5-site), whether the model is rigid or flexible, and whether the model includes polarization effects [22]. Each of these can then be broken down even further and all have their advantages and disadvantages. Overall, the choice of water model for an MD simulation will depend on the specific goals of the simulation and the level of accuracy that is required.

TIP4P/2005

Over the years, several intermolecular potential models have been developed for computer simulations of water. One commonly used model is TIP4P/2005 [23]. A water molecule consists of three atoms: two hydrogen atoms (H) and one oxygen atom (O). In the TIP4P/2005 water model, an additional interaction site called the virtual site (M) is introduced, as depicted in Figure 3.12. The M site is in the same plane with

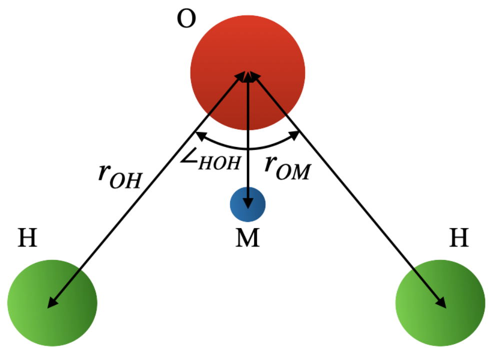

Figure 3.12: Four site water model for TIP4P/2005. Figure modified after [23].

the O and H atoms and is positioned along the bisector of the H-O-H angle and does not interact with the other atoms. The charged sites interact with each other through the Coulomb potential.

$$u_{electrostatic}(r_{ab}) = \frac{1}{4\pi\varepsilon_0}\frac{q_a q_b}{r_{ab}} \tag{3.15}$$

where q_a and q_b represent the charges on sites a and b respectively, ε_0 symbolizes the permittivity of free space (vacuum), and r_{ab} signifies the distance between site a and site b. The oxygen sites interact via the Lennard-Jones (LJ) potential,

$$u_{LJ}(r_{\mathrm{OO}}) = 4\varepsilon\left(\frac{\sigma^{12}}{r_{\mathrm{OO}}^{12}} - \frac{\sigma^{6}}{r_{\mathrm{OO}}^{6}}\right), \tag{3.16}$$

where r_{OO} represents the distance between two oxygen atoms, ε and σ denote the bond strength and distance parameters of the Lennard-Jones potential, respectively. The TIP4P/2005 parameters can be found in Table 3.3.

As previously stated, molecular dynamics simulations are critical in understanding the bulk characteristics of protein-water solutions at various concentrations and temperatures. It is possible to acquire vital insights into the complicated dynamics of both protein and water molecules by investigating these bulk properties. The

Table 3.3: Potential parameters of the TIP4P/2005. These values are taken from [23].

Parameter	Value
σ (nm)	0.31668
ϵ/k (K)	106.1
r_{OH} (nm)	0.09572
r_{OM} (nm)	0.01577
q_H (e)	0.5897
q_O (e)	0.0
q_M (e)	- 1.1794
$\angle$ HOH (°)	104.52

integration of experimental and simulation data is critical because it improves our understanding of the intricate and dynamic interactions between proteins and water. By combining experimental and computational methods, researchers can comprehensively study protein-water systems, offering potential breakthroughs in drug design, bioengineering, and our understanding of fundamental biological processes [24, 25]

Bibliography

[1] J. Sandercock. Tandem fabry-perot interferometer tfp-1, operator manual. *JRS Scientific Instruments*, 2001.

[2] A. Yariv and P. Yeh. *Photonics: optical electronics in modern communications.* Oxford university press, 2007.

[3] D. Hanlon. *Temperature dependence of acoustic properties of natural snail mucus by Brillouin spectroscopy.* MSc Thesis, Memorial University of Newfoundland, 2020.

[4] M. Chaplin. Structure and properties of water in its various states. *Encyclopedia of water: science, technology, and society*, pages 1–19, 2019.

[5] G. Van Rossum and F. Drake. *Python 3 Reference Manual.* CreateSpace, Scotts Valley, CA, 2009.

[6] M. Newville, T. Stensitzki, D. Allen, M. Rawlik, A. Ingargiola, and A. Nelson. Lmfit: Non-linear least-square minimization and curve-fitting for python. *Astrophysics Source Code Library*, pages ascl–1606, 2016.

[7] A. Pine. Brillouin scattering study of acoustic attenuation in fused quartz. *Physical Review*, 185(3):1187, 1969.

[8] R. Arunkumar, C. Drummond, and T. Greaves. Ftir spectroscopic study of the secondary structure of globular proteins in aqueous protic ionic liquids. *Frontiers in Chemistry*, 7:74, 2019.

[9] S. Lewis, A. Lewis, and P. Lewis. Prediction of glycoprotein secondary structure using atr-ftir. *Vibrational Spectroscopy*, 69:21–29, 2013.

[10] I. Spiridon, C. Teaca, and R. Bodirlau. Structural changes evidenced by ftir spectroscopy in cellulosic materials after pre-treatment with ionic liquid and enzymatic hydrolysis. *BioResources*, 6(1):400–413, 2011.

[11] P. Griffiths. Fourier transform infrared spectrometry. *Science*, 222(4621):297–302, 1983.

[12] B. Smith. *Fundamentals of Fourier transform infrared spectroscopy.* CRC press, 2011.

[13] C. Vigano, L. Manciu, F. Buyse, E. Goormaghtigh, and J. Ruysschaert. Attenuated total reflection ir spectroscopy as a tool to investigate the structure, orientation and tertiary structure changes in peptides and membrane proteins. *Peptide Science*, 55(5):373–380, 2000.

[14] P. Larkin. *Infrared and Raman spectroscopy: principles and spectral interpretation.* Elsevier, 2017.

[15] R. Silverstein and G. Bassler. Spectrometric identification of organic compounds. *Journal of Chemical Education*, 39(11):546, 1962.

[16] B. Stuart. *Infrared spectroscopy: fundamentals and applications.* John Wiley & Sons, 2004.

[17] S. Venyaminov and F. Prendergast. Water (h2o and d2o) molar absorptivity in the 1000–4000 cm- 1range and quantitative infrared spectroscopy of aqueous solutions. *Analytical biochemistry*, 248(2):234–245, 1997.

[18] A. Hospital, J. Goñi, M. Orozco, and J. Gelpí. Molecular dynamics simulations: advances and applications. *Advances and applications in bioinformatics and chemistry*, pages 37–47, 2015.

[19] M. Abraham, T. Murtola, R. Schulz, S. Páll, J. Smith, B. Hess, and E. Lindahl. Gromacs: High performance molecular simulations through multi-level parallelism from laptops to supercomputers. *SoftwareX*, 1:19–25, 2015.

[20] D. Frenkel, B. Smit, and M. Ratner. *Understanding molecular simulation: from algorithms to applications*, volume 2. Academic press San Diego, 1996.

[21] A. Stone. *The theory of intermolecular forces*. oUP oxford, 2013.

[22] Q. Johnson. An analysis of prominent water models by molecular dynamics simulations. 2010.

[23] J. Abascal, E. Sanz, R. García Fernández, and C. Vega. A potential model for the study of ices and amorphous water: Tip4p/ice. *The Journal of chemical physics*, 122(23):234511, 2005.

[24] J. Kay and M. Jewett. Lysate of engineered escherichia coli supports high-level conversion of glucose to 2, 3-butanediol. *Metabolic Engineering*, 32:133–142, 2015.

[25] N. Bongaerts, Z. Edoo, A. Abukar, X. Song, S. Sosa-Carrillo, S. Haggenmueller, J. Savigny, S. Gontier, A. Lindner, and E. Wintermute. Low-cost antimycobacterial drug discovery using engineered e. coli. *Nature Communications*, 13(1):3905, 2022.

Chapter 4

Temperature Dependence of the Viscoelastic Properties of a Natural Gastropod Mucus by Brillouin Light Scattering Spectroscopy

Reproduced from D. F. Hanlon, M. J. Clouter, and G. T. Andrews, Soft Matter, 2023, DOI: 10.1039/D3SM00762F. with permission from the Royal Society of Chemistry.

Co-Authorship Statement

We, the authors of this manuscript, have contributed collectively to the research, writing, and preparation of this work. Each author's contribution is outlined below:
D. F. Hanlon: Writing, Data Collection, Data Analysis, Instrumentation Design, and Editing.
M. J. Clouter: Writing, Data Analysis, Instrumentation Design, Editing, and Supervision.

G. T. Andrews: Writing, Data Collection, Data Analysis, Editing, Supervision, Conceived and Administered Experiment.

4.1 Abstract

Brillouin spectroscopy was used to probe the viscoelastic properties of a natural gastropod mucus at GHz frequencies over the range -11 °C $\leq T \leq$ 52 °C. Anomalies in the temperature dependence of mucus longitudinal acoustic mode peak parameters and associated viscoelastic properties at $T = -2.5$°C, together with the appearance of a peak due to ice at this temperature, suggest that the mucus undergoes a phase transition from a viscous liquid state to one in which liquid mucus and solid ice phases coexist. Failure of this transition to proceed to completion even at -11 °C is attributed to glycoprotein-water interaction. The temperature dependence of the viscoelastic properties and the phase behaviour suggest that water molecules bind to glycoprotein at a temperature above the onset of freezing and that the reduced ability of this bound water to take on a configuration that facilitates freezing is responsible for the observed freezing point depression and gradual nature of the liquid-solid transition.

4.2 Introduction

Gastropod mucus is a fascinating polymer hydrogel consisting primarily of long chains of tangled high molecular weight glycoproteins in 91 wt% to 98 wt% water [1–3]. These glycoproteins, despite being present at low weight percentages, are anticipated to play a dominant role in many of the physical properties of this natural complex fluid. This influence is expected to be especially apparent in the mucus viscoelasticity because these biopolymers expand in water and cross-link to form a gel [1]. In fact, stress-strain measurements with strain rates ≤ 100 Hz reveal non-Newtonian behaviour with the mucus displaying characteristics of a soft elastic solid at low strains and yielding at higher strains and presenting as a viscous liquid [1]. Analogous measurements of the high-frequency (*i.e.*, MHz to GHz) viscoelasticity have not been performed, but based on studies of other complex fluids, probing the upper end of this range would be particularly valuable because it would lead to the discovery of links between the viscoelasticity and the dynamics and structure of the mucus [4–6]. Quantification of the temperature dependence of the mucus viscoelastic properties in this frequency range would also be of considerable value because it would reveal other glycoprotein-induced anomalies and permit the phase behaviour of the mucus to be mapped. Such data is important for comparison to molecular dynamics simulations results on protein-water dynamics to inform refinement of models [7]. Knowledge of the temperature dependence of gastropod mucus viscoelasticity is also important from a technological standpoint. For example, synthetic mucus mimics are being developed for possible application as non-toxic adhesives to close internal wounds due to the ability of mucus to adhere to wet surfaces [8] and solutions of so-called antifreeze glycoproteins are being investigated as potential replacements for conventional cryprotectants due to their ability to provide the required high viscosity at low concentrations [9, 10].

In this study, Brillouin light scattering spectroscopy was used to characterize the temperature dependence of the GHz-frequency viscoelastic properties of a natural snail mucus over the range -11 °C to 52 °C. We report values for hypersonic velocity and attenuation, compressibility, complex longitudinal modulus, and apparent viscosity, and document a large and previously undiscovered glycoprotein-induced freezing point depression associated with an incomplete phase transition from the liquid state to one in which liquid mucus and solid ice coexist. These results complement previously published data on the low-frequency viscoelasticity of gastropod mucus and provide new insights into the physics of aqueous glycoprotein solutions and the role played by glycoproteins in the phase behaviour of these systems. In a broader context, the present study contributes new knowledge on phonon dynamics and phase transitions in complex fluids, and on water-macromolecule interaction vital to understanding the intricate behaviour of biological systems.

4.3 Brillouin Scattering in Liquids

Brillouin spectroscopy is a technique used to probe thermal acoustic waves by inelastic scattering of light. For a 180° backscattering geometry as used in the present work, application of energy and momentum conservation to the scattering process reveals that the hypersound velocity, v, and frequency shift of the incident light, f_B, are related by

$$v = \frac{f_B \lambda_i}{2n}, \tag{4.1}$$

where n is the refractive index of the target material at the incident light wavelength λ_i.

For liquids, the longitudinal kinematic viscosity or apparent viscosity $\eta = 4\eta_s/3 + \eta_b$, where η_s and η_b are the shear and bulk viscosity, respectively, is related to the full width at half maximum of the Brillouin peak due to the longitudinal acoustic mode via [11],

$$\Gamma_B = \frac{16\pi^2 n^2}{\rho \lambda_i^2} \left[\eta + \frac{\kappa}{C_p} (\gamma - 1) \right], \tag{4.2}$$

where ρ is the density, κ is the thermal conductivity, and $\gamma = C_p/C_v$ is the ratio of specific heat at constant pressure to that at constant volume. The second term in the brackets of this expression is usually neglected for simple liquids, thus leaving the expression for viscosity [11],

$$\eta = \frac{\rho \lambda_i^2}{16\pi^2 n^2} \Gamma_B. \tag{4.3}$$

The linewidth Γ_B is determined by the time that a thermal density fluctuation interacts with the incident light and is therefore a measure of its lifetime or, equivalently, its attenuation [12].

The complex longitudinal modulus, often referred to simply as the complex modulus, is related to the frequency shift and linewdith via [13],

$$M = M' + M'' i = \rho \left(\frac{f_B \lambda_i}{2n} \right)^2 + 2\pi \left(\frac{\rho \lambda_i^2}{16\pi^2 n^2} \Gamma_B \right) f_B i, \tag{4.4}$$

where the quantities in parentheses are the hypersound velocity and apparent viscosity given by Eqs. 4.1 and 4.3, respectively. M' is the storage modulus (or bulk modulus) and is a measure of how much energy is stored elastically in the system. The loss modulus, M'', is a measure of how much energy is lost through heat in the system.

The frequency-independent sound absorption coefficient can also be expressed in terms of f_B and Γ_B through [11],

$$\frac{\alpha}{f^2} = \frac{\Gamma_B}{2v f_B^2}. \tag{4.5}$$

Measurements of Brillouin peak frequency shift f_B and linewidth Γ_B thereby permit direct determination of hypersound velocity, apparent viscosity, complex longitudinal modulus, and sound absorption coefficient via Eqs. 4.1 through 4.5.

4.4 Experimental Details

4.4.1 Sample Preparation

The mucus used in the present study was a transparent and viscous natural snail mucus with a glycoprotein concentration of ~ 6% and water concentration of ~ 94% [14]. The mucus was kept in a sealed container at room temperature until a sample was required for use in experiments. A syringe was used to extract ~5 ml of mucus from the parent container. One end of a thin plastic tube was then attached to the tip of the loaded syringe while the other end was placed in the bottom of a sample cell consisting of a ~ 15 cm-long, 6 mm outer diameter/4 mm inner diameter glass tube sealed by glassblowing at one end. By applying gentle pressure to the syringe plunger, mucus was slowly forced from the syringe barrel, through the tube, and into the sample cell. This gradual extrusion helped minimize air bubble formation in the mucus during loading. To allow space for expansion upon cooling near and at the mucus freezing point, the cell was only filled to half capacity (~ 1 cm^3 of mucus). Once loaded, the top of the sample cell was sealed with a Teflon cap held in place with epoxy. After loading, the glass cell was placed in a sample holder in preparation for Brillouin scattering experiments.

4.4.2 Temperature-Controlled Sample Chamber

Fig. 4.1 shows schematic diagrams of the custom-built temperature-controlled sample chamber (Fig. 4.1a) and sample cell holder (Fig. 4.1b). The sample chamber was made primarily from aluminum and was designed to enclose the sample cell holder. The brass top plate had an electrical feed-through and a vacuum line port. It was important in this work that the sample chamber be evacuated to ensure the brass

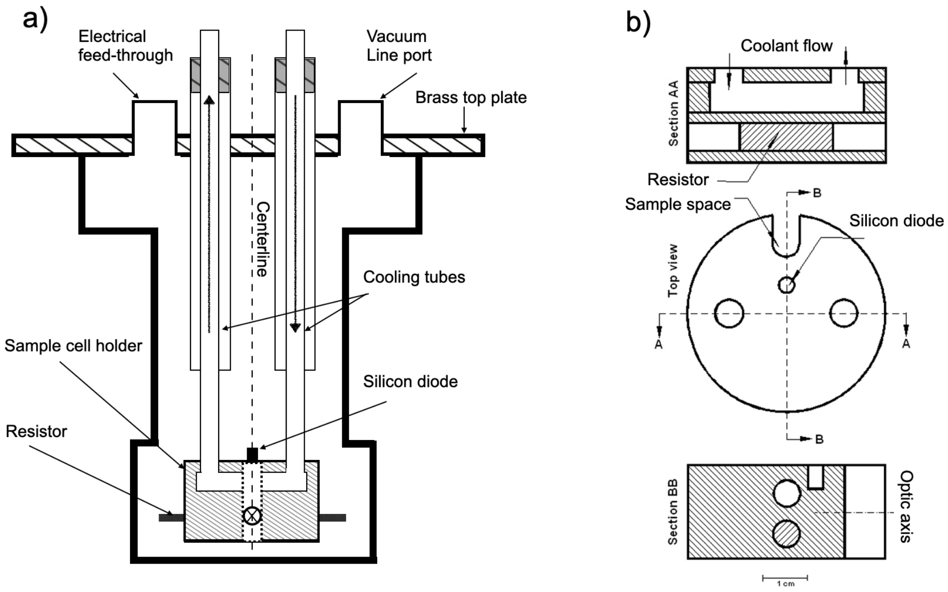

Figure 4.1: a) Schematic of the custom-built temperature-controlled sample chamber used in the present work with sample cell holder in place. b) Machine drawing of the sample cell holder shown in a).

sample cell holder, and therefore the sample, was at the desired temperature with high precision. Brass was used for the sample cell holder due to its exceptional thermal properties. Cooling tubes in the sample chamber allowed for the circulation of antifreeze coolant through the sample holder which helped for cooling the holder and for temperature stabilization. A 50 Ω resistor was placed in a vacant space in the sample holder to heat up the holder and to also assist with stabilization. A silicon diode was used to obtain the temperature of the sample cell holder. A glass sample cell which the sample resides in was held in place in the sample space shown in the sample cell holder (vertical dashed line, Fig. 4.1a) and the sample space labelled in Fig 4.1b. Thermal paste was used to ensure adequate contact between the glass sample cell and the brass sample cell holder.

The temperature of the sample cell holder is controlled by use of a heater and cooling bath system. Using a cryogenic temperature controller from Lakeshore Cryotronics. Depending on the desired temperature of the experiment, either the heater or the cooling bath is initially turned on. Once the desired temperature is reached, the heater and refrigeration bath will work together to stabilize the sample cell holder. If the sample cell holder surpasses the desired temperature (voltage set-point) the heater will turn off and the cooling bath will turn on. Similarly, if the sample cell holder gets too cold, the bath will turn off and the heater will turn on. A full description of the temperature control operation has been explained previously [15, 16].

Accuracy of the temperature controlled sample holder was measured by collecting Brillouin spectra of water between $-5^\circ\mathrm{C} \leq T \leq 5^\circ\mathrm{C}$, with a focus on obtaining data near $T = 0\ ^\circ\mathrm{C}$. The temperature at which spectral peaks due to ice appear was deemed the freezing point of water. The uncertainty in temperature reading from the diode was attributed to the difference between the freezing point of water (when ice appeared) and the freezing point of water found in the literature [17]. Brillouin peaks due to ice were observed in the spectra at a temperature of -0.4°C, thus the uncertainty associated with the temperature reading in this work was $\pm\ 0.4^\circ$C.

4.4.3 Brillouin Light Scattering Apparatus

Brillouin spectra were obtained using a 180° backscattering geometry using the set-up shown in Ref. [18]. Incident light of wavelength $\lambda_i = 532$ nm and power of 100 mW was provided by a Nd:YVO$_4$ single mode laser. A high-quality anti-reflection-coated camera lens of focal length $f = 5$ cm and $f/\# = 2.8$ served to both focus incident light onto the sample and to collect light scattered by it. After exiting this lens, the scattered light was focused by a 40 cm lens onto the 450 μm-diameter input pinhole of an actively-stabilized 3+3 pass tandem Fabry-Perot interferometer (JRS Scientific

Table 4.1: Refractive index and density of snail mucus, water, and ice Ih. Lone entries in the 'Refractive Index' and 'Density' columns indicate that the temperature dependence of the quantity was not known and was therefore taken to be constant and equal to the value shown over the temperature range probed in the present work.

Substance	Refractive Index [@ 532 nm]	Density [kg/m^3]
Mucus	1.34 [19]	1040 [Present Work]
Water	$\left(\frac{n^2-1}{n^2+2}\right)\frac{1}{\rho} = 2.180454\times10^{-4} + 9.746345\times10^{-9}\rho$ $-1.286164\times10^{-8}T - 1.666262\times10^{-11}\rho^2$ [21]	$T \geq 0$ °C: Values in Table I [20] $T < 0$ °C: Values in Table II [22]
Ice Ih	1.3117 at -7 °C by interpolation of data in Table I [23]	$\rho = \rho_0/[1 + 1.576^{-4}T - 2.778\times10^{-7}T^2$ $+8.850\times10^{-9}T^3 - 1.778\times10^{-10}T^4]$ [24]

Instruments) by which it was frequency-analyzed. The free spectral range of the interferometer was set to 30 GHz and the finesse was ~ 100. The light transmitted by the interferometer was incident on a 700 μm pinhole and detected by a low-dark count ($\lesssim$ 1 s^{-1}) photomultiplier tube where it was converted to an electrical signal and sent to a computer for storage and display.

4.4.4 Ancillary Quantities

To determine viscoelastic properties from Brillouin data the refractive index and density of the mucus, water, and ice were required. The density of the mucus was found to be 1040 ± 30 kg/m^3 by measuring the mass of a precisely known volume (100 ml) using a (Secura®, Satorius) microbalance and was taken to be constant over the temperature range probed in these experiments. This value is in good agreement with published values [19]. The refractive index of mucus was taken to be $n = 1.34$ [19]. For water, the refractive index and density were obtained from an empirical expression in Ref. [21] and tabulated values in Refs. [20] and [22], respectively. For ice, the refractive index at 532 nm was determined by interpolation of data in Table I

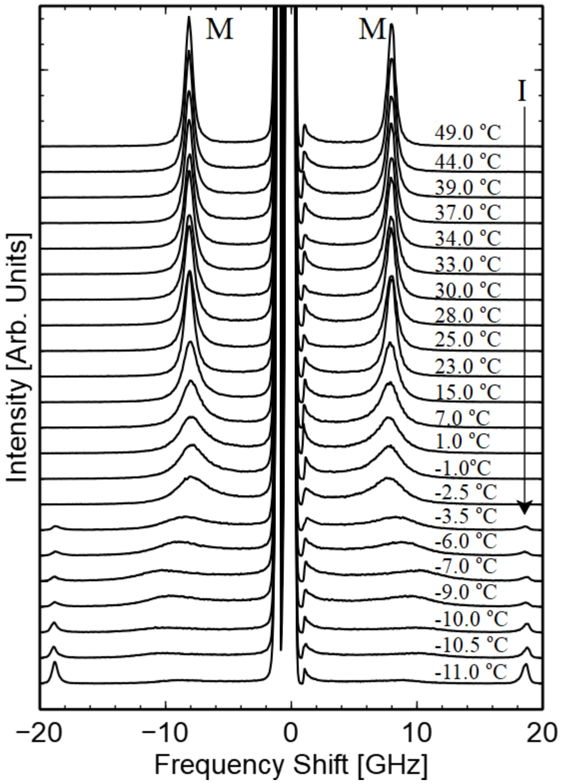

Figure 4.2: Brillouin spectra of a natural snail mucus (Sample #2). Temperatures at which spectra were collected are indicated. **M** and **I** represent peaks due to mucus and ice, respectively.

of Ref. [23] and the density using an empirical expression from Ref. [24]. A summary is provided in Table 4.1.

4.5 Results & Discussion

4.5.1 Brillouin Spectra and Mode Assignment

Fig. 4.2 shows a representative series of mucus spectra obtained from one of three nominally identical samples at temperatures in the range -11°C ≤ T ≤ 52°C. Similar sets of spectra were collected from the other two samples (see Fig. S1 in the Supplementary Materials). Peak parameters including frequency shifts, linewidths (FWHM), and integrated intensity were obtained by fitting Lorentzian functions to the Stokes and anti-Stokes peaks and averaging the resulting best-fit parameters. To obtain intrinsic linewidths, the instrumental linewidth of 0.3 GHz was subtracted from FWHM values obtained from the Lorentzian fits. Estimated uncertainties in peak parameters were obtained from the uncertainty in the Lorentzian fits. Raw peak parameter data (frequency shift, linewidth, and integrated intensity) for all three samples are presented in Tables S1-S3 in the Supplementary Materials.

Two sets of Brillouin peaks are present in the spectra - one at ~ ±8.0 GHz over the entire temperature range and another at ~ ±18.5 GHz for $T \leq -2.5^\circ$C. Due to the similarity of these shifts to those of liquid water (see Fig. 4.3) and that expected for solid water using a backscattering geometry at $T \lesssim 0$ °C [24–26], these peaks are attributed to the longitudinal acoustic mode in the liquid mucus and (likely polycrystalline) ice I_h, respectively.

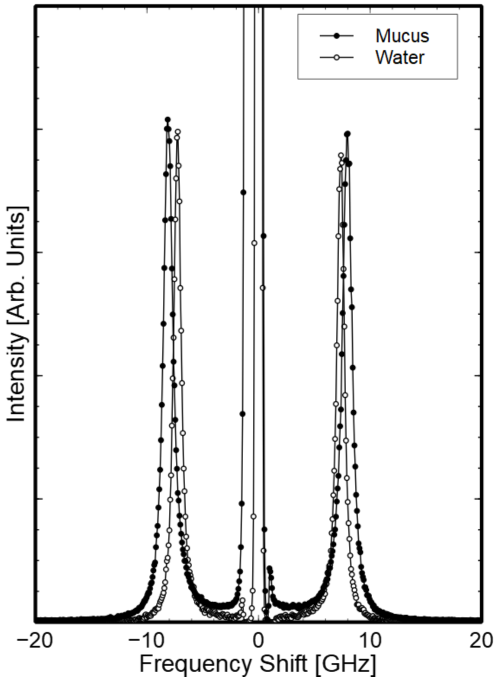

Figure 4.3: Room temperature Brillouin spectra of pure snail mucus and ultra pure water.

4.5.2 Phase Transition: Raw Spectral Signatures

Fig. 4.4 shows a discontinuous change in the temperature dependence of the mucus peak parameters at $T_{pt} = -2.5$ °C and presence of the ice peak for $T \leq -2.5$ °C, consistent with a transition of the system from liquid mucus to one in which mucus and ice coexist. More specifically, the presence of a peak at a shift similar to that of the longitudinal acoustic mode for pure water in spectra collected for 50 °C ≥ T ≥ -2.5 °C indicates that the mucus is in a liquid state over this range. The frequency shift of this peak decreases gradually with decreasing temperature over this range. The intensity of this peak also shows an overall decrease with temperature and an abrupt drop near -2.5 °C. The peak width increases gradually with decreasing temperature over the same range, reflecting moderate damping of this mode as the temperature approaches -2.5 °C. Moreover, the absence of the ice peak for $T > -2.5$ °C also indicates that only the liquid phase is present above this temperature.

In the range -11.0 °C ≤ T ≤ -2.5 °C, the presence of the peak due to liquid mucus and a second peak at a frequency shift close to that of polycrystalline ice Ih indicates the coexistence of liquid mucus with solid ice to at least -11.0 °C. The intensity of the ice peak increases with decreasing temperature over this range while there is a gradual decrease in the intensity of the liquid mucus peak, indicative of increasing amounts of ice and a reduction in the amount of liquid mucus in the system. Over this range there is also a rapid increase in mucus peak linewidth with decreasing temperature, suggesting increased damping of this mode. Analogous sets of Brillouin data for two other nominally identical samples are shown in Fig. S2 in the Supplementary Materials document.

Table 4.2: Hypersound velocity, storage (bulk) modulus, and loss modulus of a natural snail mucus and water at selected temperatures. Quantities for the present work are average values determined from data for three nominally identical samples. Uncertainty in sound velocity is ~ 2%, 4% in the bulk modulus and ranged from 3% at 50˚C to 9% at -11˚C.

Substance &	Velocity [m/s]				Storage (Bulk) Modulus [GPa]				Loss Modulus [GPa]			
Temperature Range	-10˚C	-2.5˚C	0˚C	50˚C	-10˚C	-2.5˚C	0˚C	50˚C	-10˚C	-2.5˚C	0˚C	50˚C
Mucus, -11˚C → 50˚C [Pres Work]	1770	1570	1580	1650	3.25	2.56	2.60	2.83	6.1	1.4	1.1	0.3
Water, -5.0˚C → 50 ˚C [Pres Work]	–	1330	1360	1500	-	1.76	1.85	2.22	-	0.55	0.48	0.2
Water, -9˚C → 100˚C - Ref. [11]	-	1375	1395	1540	-	1.89	1.95	2.34	-	-	-	-

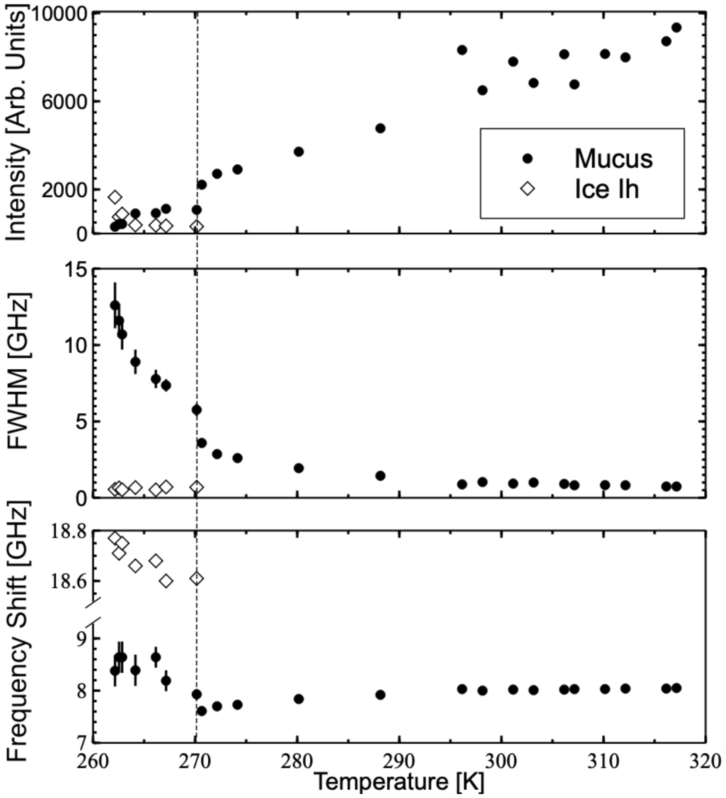

Figure 4.4: Brillouin peak intensity, linewidth, and frequency shift versus temperature for snail mucus. ■ - Mucus Mode, □ - Ice Mode. The dashed vertical line indicates the phase transition at -2.5 °C.

4.5.3 Viscoelastic Properties

Fig. 4.5 shows the temperature dependence of the hypersound velocity, compressibility, and apparent viscosity derived from the Brillouin data for a representative sample (see Fig. S3 for corresponding data for the two other samples). Viscoelastic properties at selected temperatures for this sample are presented in Table 4.2. Also shown are viscoelastic properties for water determined in the present work along with those of water from previous studies. The behaviour of viscoelastic properties of these systems above and below the phase transition temperature of $T_{pt} = -2.5$ °C is compared below.

Hypersound Velocity

For 50 °C ≥ T ≥ -2.5 °C, the mucus hypersound velocity shows an overall decrease at a rate of ~ 1.5 m/s/°C from ~ 1650 m/s to ~ 1570 m/s at the upper and lower ends of this interval, respectively (see Fig. 4.4). Analogous hypersound velocity data obtained for water in the present work and in previous studies [11, 20, 27] shows a similar trend over this temperature range, but with a rate of decrease that is ~ 2× higher and magnitude that is ~ 10% lower than for the mucus. Rates of decrease and velocities intermediate to those of water and snail mucus are observed for several aqueous polymer solutions with polymer concentrations similar to the glycoprotein concentration in the mucus over the temperature range 20 °C to 45 °C [28–34].

For -2.5 °C ≥ T ≥ -11 °C, the mucus hypersound velocity displays an overall increase at a decreasing rate from its minimum value of ~ 1570 m/s at $T_{pt} = -2.5$ °C to ~ 1700 m/s at -11.0 °C. This behaviour contrasts with that for supercooled water for which the velocity is ~ $10 - 30\%$ lower and which exhibits a rapid monotonic decrease with temperature over this range [11, 27]. The formation of ice results in a larger glycoprotein-to-water ratio [35] resulting in higher mucus mode velocity which increases as temperature decreases due to additional ice formation. The ice mode velocity shows a slight increase from 3770 m/s at -2.5°C to 3840 m/s at -11.0°C. The same trend is observed for pure polycrystalline ice Ih but the velocities are approximately 2-4% lower than for the ice-like solid [36].

Complex Longitudinal Modulus & Adiabatic Compressibility

Values of mucus complex longitudinal modulus (storage and loss moduli) at select temperatures are presented in Table 4.2. The storage (bulk) modulus exhibits a minimum at -2.5 °C and takes on a value that is ~ 30% greater than that for water at the highest temperature probed (~ 50 °C) in these experiments. At the lowest temperature probed (-11 °C), the mucus bulk modulus is approximately double that of supercooled water Ref.[27]. In general, for both mucus and ultra-pure water, the loss modulus decreases with increasing temperature. Furthermore, the value for both mucus and water at 50°C are nearly identical. As in a previous study on biopolymer hydrogels, the loss modulus in this system shows a greater change with temperature than the storage modulus [13]. The likely reason for this is that water has a relatively high storage (bulk) modulus and the addition of a small amount of protein would not cause it to change significantly. The loss modulus, shows analogous results to that of the FWHM as a function of temperature. Additionally, as the loss modulus is a measure of the amount of energy lost through heat in a system, we can say based on our data that as the temperature decreases more energy is lost in the system.

Fig. 4.5 shows the temperature dependence of the adiabatic compressibility of the mucus, $\kappa_s = 1/\rho v^2$. The compressibility displays a maximum at $T = -2.5$ °C. Below T_{pt}, κ_s decreases dramatically with decreasing temperature, while above the transition point it shows a gradual decline with increasing temperature. Interestingly, at the lowest temperature probed, the adiabatic compressibility of mucus is 50% larger than that of water [11] but is only ~ 18% higher than the value for water at the highest temperature probed.

Apparent Viscosity

The temperature dependence of the apparent viscosity of the snail mucus obtained from Eqn. 4.3 is shown in Fig. 4.5. The observed decrease with increasing temperature is similar to that previously reported for water [37] and other aqueous polymer solutions [29–33].

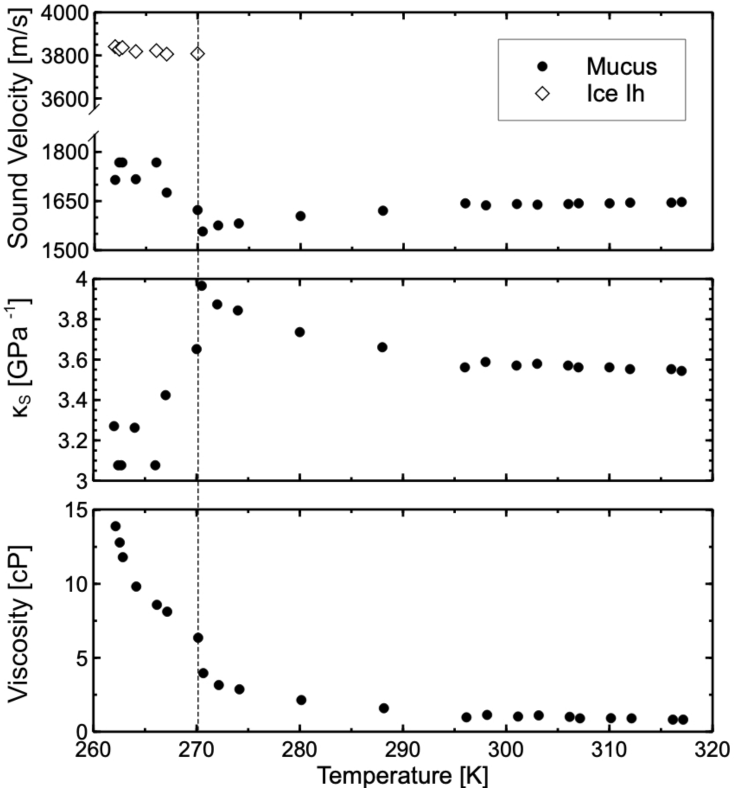

Figure 4.5: Hypersound velocity, adiabatic compressibility, and apparent viscosity versus temperature for a natural snail mucus (Sample #2). The dashed vertical line indicates the phase transition at -2.5 °C. The uncertainty in measured quantities is approximately 2× the size of the symbols.

Table 4.3: Best-fit parameters for fit of function $\ln(\eta) = \ln\eta_0 + \frac{E_a}{k_B T}$ to experimentally determined apparent viscosity.

Temperature Range	Sample	$\ln\eta_0$ (cP)	E_a kJ/mol	R^2
	1	-4.5 ± 0.4	13.6 ± 0.3	0.987
25.0°C ≤ T ≤ 52.0°C	2	-4.5± 0.4	13.6 ± 0.3	0.993
	3	-3.9 ± 0.6	13.5 ± 0.5	0.983
	Mean	-4.3 ± 0.5	13.6 ± 0.4	0.988
	Water[1]	-5.57 ± 0.3	13.8 ± 0.3	0.991

Fig. 4.6 shows the natural logarithm of the apparent viscosity as a function of inverse temperature for snail mucus. Analogous data for water is also shown for the

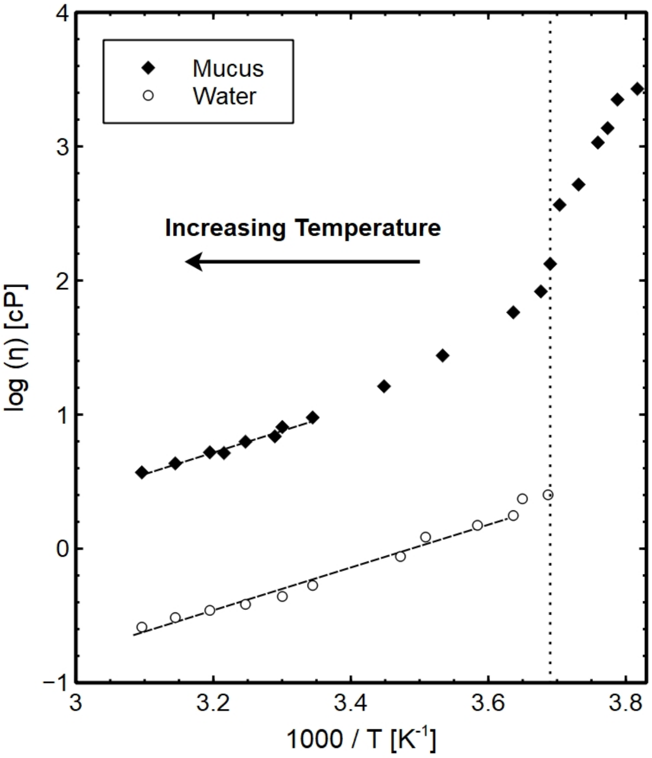

Figure 4.6: Natural logarithm of mucus viscosity versus inverse temperature. ◆ - Mucus, ○ - Water. Dashed lines represents best fits. Results for linear fits are given in Table 6.2. The dotted vertical line indicates the value of $1/T$ corresponding to the phase transition at -2.5 °C.

purposes of comparison. Over the high temperature range 25 °C $\leq T \leq$ 52 °C, $\ln(\eta)$ depends linearly on $1/T$ so we fit an Arrhenius relationship of the form

$$\eta = \eta_0 e^{E_a/k_B T} \tag{4.6}$$

to this data and extracted the activation (enthalpy) energy for the mucus E_a^m = 13.6 ± 0.4 kJ/mol (H-bond values typically range from $\sim 6-12$ kJ/mol [38, 39]). Here, η_0 is a prefactor that contains the entropic contribution to the viscosity and k_B is the Boltzmann constant [40]. A similar fit for water over the range 0 °C $\leq T \leq$ 52 °C yields E_a^w = 13.8 ± 0.3 kJ/mol (see Table 4.3).

The constant value of mucus activation energy over the high temperature range along with the fact that $E_a^m \simeq E_a^w$ over this range, suggests that the difference in apparent viscosity between mucus and water can be attributed to the entropic prefactor η_0. A higher value observed for mucus indicates an decreased level of disorder within the system, resulting in a lesser number of possible microscopic configurations compared to water. Moreover, due to viscosity being a measure of the internal friction of a fluid, the relatively higher apparent viscosity of mucus in this high-temperature region implies that mucus possesses a longer structural relaxation time in comparison to water. This observation is logical since an increase in the systems disorder or microscopic configurations would correspondingly require a longer duration for the system to relax. This is in line with previous studies [13, 41–44], along with a proposed model consisting of a high-hydration state (liquid-like system) provides further support for this observation. Similarly, the apparent viscosity can also provide information on the density fluctuation relaxation times. The apparent viscosity, as mentioned earlier, represents the resistance to flow exhibited by a material. Density fluctuations in a material are related to the molecular arrangment and motion of molecules in the solution. It is therefore inherently linked to the viscosity of the fluid [12, 45, 46]. In this high-temperature region, since the apparent viscosity is linear, this also suggests that the relaxation time for density fluctuation remains constant over temperature regime [40].

The intermediate region shows a nonlinear increase in η up to the phase transition temperature T_{pt}. This increase in viscosity is accompanied by an increase in the structural relaxation time [41]. Moreover, it is important to note that bound and free water exhibit different density fluctuation relaxation times by default [40]. Bound water, being more constrained in its motion near the solute, has slower dynamics compared to free water. As previously suggested these differences contribute to the change in apparent viscosity of the system, with their respective proportions of bound and free molecules playing a role [7, 40]. Thus the non-Arrhenius behaviour seen in this region implies that the nonlinear increase in apparent viscosity is due to the fact that the density fluctuation relaxation time as well as structural relaxation times change in a similar manner in this case. Previous studies has stated that this non-Arrhenius behaviour is related to the onset of cooperative motions and molecular collisions of proteins and water molecules in the system [47]. In this temperature region, the non-Arrhenius behaviour is usually characterized by either the power law or the Vogel–Fulcher–Tammann equation [47, 48]. The latter is often associated with glass transitions in liquids.

Below the transition, there is a rapid, approximately linear, increase in the apparent viscosity. It is also worth noting that the values of $d\eta/dT$ for the mucus above and below T_{pt} are drastically different. This is not surprising given that below T_{pt} there is the coexistence of ice Ih and liquid mucus. A previous proposed model has suggested that in the case of antifreeze glycoproteins, that the glycoproteins are bound to water in the proteins respective hydration shell [49]. Furthermore, the data presented in this manuscript, combined with the apparent viscosity data, suggests a probable scenario where proteins bound to the ice require a higher activation energy, as observed here, to induce viscous flow. This can be attributed to the stronger bond existing between the protein, water, and ice.

Hypersound Attenuation

Fig. 4.7 shows the frequency-independent hypersound absorption coefficients for mucus and water determined from Eq. 4.5 as a function of temperature for $T > -2.5$ °C. It is clear from this result that over this range more sound is absorbed in the medium

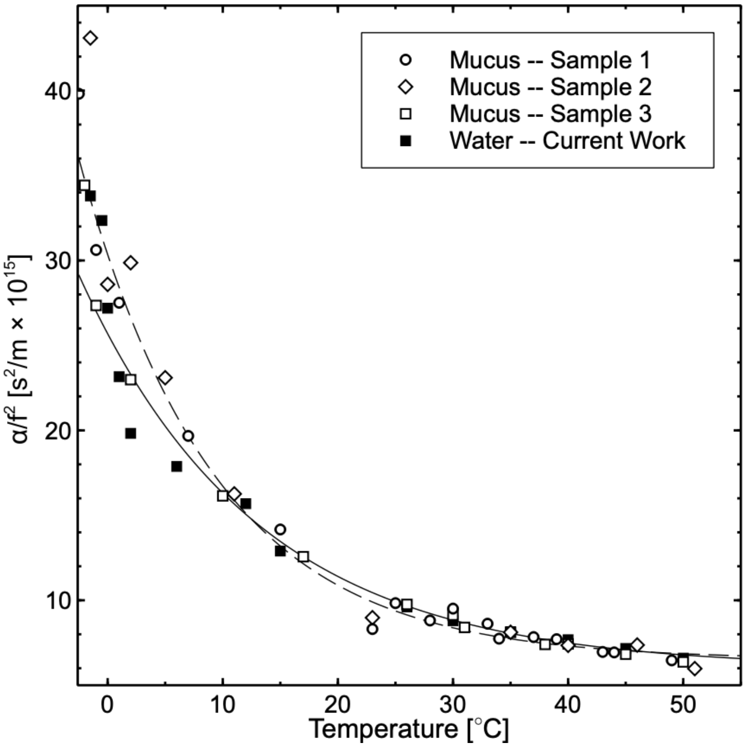

Figure 4.7: Plot of α/f^2 for mucus samples and de-ionized water collected as a function of temperature over the range -2.5°C ≤ T ≤ 52.0°C. Dashed line is a representative fit for all mucus samples. Solid line is the best fit obtained for ultra-pure water. The uncertainty in the data is approximately the size of the symbols.

as temperature decreases. This is expected because the absorption coefficient is proportional to apparent viscosity, which increases with decreasing temperature, and inversely proportional to hypersound velocity, which decreases with deceasing temperature (see Eq. 4.5).

The trend in Fig. 4.7 suggests fitting an equation of the form $\alpha/f^2 = A\exp(-B/T)$ to the $\{\alpha/f^2, T\}$ data to obtain an understanding of how the sound waves in snail mucus are damped throughout the temperature range -2.5°C ≤ T ≤ 52.0°C. Table 4.4 shows the best-fit parameters for both snail mucus and water in this work. The constant A is a pre-exponential factor and a measure of the intensity of the absorption, while the parameter B is a measure of how much sound is absorbed as a function of temperature. Additionally, ϵ derived from B is a measure of the energy barrier associated with this sound damping.

Below T_{pt} one must also account for the possibility of additional attenuation effects due to the presence of ice crystallites. The temperature dependence of I_m/I_i shown in Fig. 4.8 indicates that in most cases more water freezes into ice as temperature decreases, resulting in an increase in size and/or number of 'obstacle' ice crystallites in solution. There are, however, instances for which this is not the case, the behaviour varying from sample to sample, likely due to differences in the local microscopic environment, particularly with regard to glycoprotein concentration (see Fig. S2 in Supplementary Materials). This, coupled with observed differences in mucus peak linewidth for the three samples for $T < -2.5$ °C (see Fig. 4.9) suggests that damping of hypersound in this temperature range is not only due to absorption phenomena but also to scattering from ice crystallites in solution.

The non-zero intensity of the liquid mucus peak in spectra collected at -11 °C (see Fig. 4.2) indicates that there is still coexistence of liquid and solid phases at the lowest temperature studied in this experiment. It is therefore not known if the mucus will solidify completely at a proximate lower temperature. Linear extrapolation of the best-fit line for the I_m/I_i versus temperature data shown in Fig. 4.8, however, suggests that complete freezing may occur at approximately -12.5°C. At this temperature, the liquid mucus mode is expected to be completely damped out, as suggested by the diverging peak FWHM at low temperature in Fig. 4.9.

4.5.4 Phase Transition: Influence of Glycoproteins

The observed freezing point depression and coexistence of liquid and solid phases over a relatively large temperature range are manifestations of the inhibition of ice growth

Table 4.4: Best-fit parameters for fit of function $\alpha/f^2 = A\exp(-B/T)$ to experimental sound absorption data for $T \geq -2.5$ °C.

Sample	A ($\times 10^{-20}$ s^2/m)	B ($\times 10^3$ K)	ϵ kJ/mol
1	1.1 ± 0.9	4.7 ± 0.5	39.6 ± 5.6
2	3.1 ± 0.8	3.6 ± 0.6	29.9 ± 3.8
3	2.8 ± 0.7	3.3 ± 0.5	26.1 ± 3.8
Mean =	2.3 ± 0.8	3.9 ± 0.5	31.9 ± 4.8
Water^1	0.7 ± 0.1	4.6 ± 0.6	38.6 ± 5.8
Water [11]	0.5 ± 0.1	3.7 ± 0.3	30.9 ± 5.8

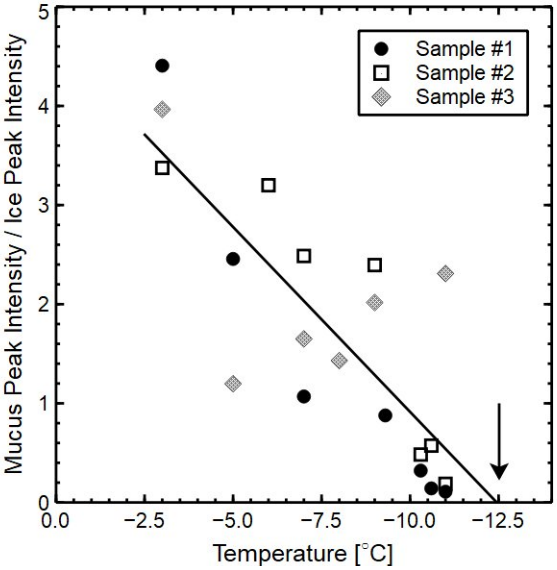

Figure 4.8: Ratio of Mucus Peak Intensity to Ice Peak Intensity versus Temperature for three nominally identical samples of snail mucus. Solid Line - Line of best-fit to experimental data (●, □, ◈): $I_m \ / \ I_i = 0.3731\mathrm{T} + 4.6444$. The arrow in the bottom right indicates the estimated temperature at which the mucus peak intensity equals zero.

due to water-glycoprotein interaction. On a microscopic scale, this effect is usually attributed to glycoprotein adsorption onto the surface of nucleating ice crystallites [50, 51]. Intuitively, however, a more likely track to freezing is one in which water binds to the mucus glycoprotein molecules at a temperature above the inception of freezing as shown schematically in Fig. 4.10. In fact, evidence for such binding

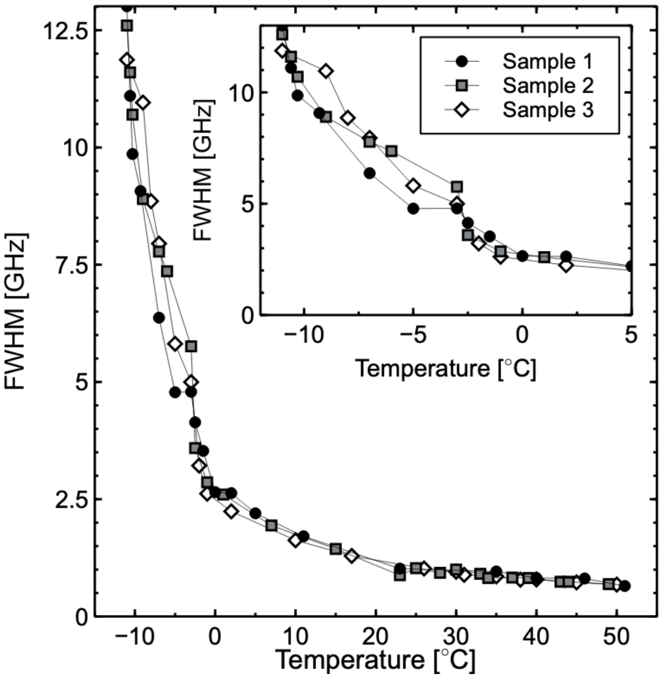

Figure 4.9: Mucus Peak Linewdith versus Temperature. The inset highlights the sample-to-sample differences in FWHM for temperatures below the phase transition at -2.5 °C.

has been observed for glycoproteins from *Dissostichus Mawsoni* [49]. Bound water molecules in the glycoprotein hydration shell would have a reduced ability to reorient and take up a configuration that would permit freezing. Due to a reduction in available thermal energy, increasing amounts of water would become bound to glycoprotein molecules as temperature is decreased, leaving less free water and causing hydration shells to swell. This would result in a lowering of the temperature at which ice is formed and, when freezing did ensue under such conditions, the ice would be in the form of nanocrystallites attached to glycoprotein molecules in solution. The results of the present study provide strong support for this route to freezing. If the inhibition of ice growth was due to glycoprotein molecules adsorbing onto the surface of nucleating ice crystallites, one would expect to find the ice at the solution surface

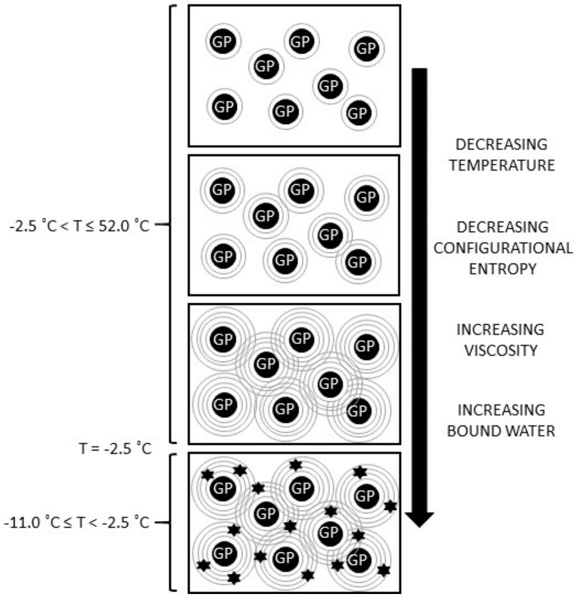

Figure 4.10: Simplified schematic representation of changes in the snail mucus system with decreasing temperature over the range -11.0 °C < T ≤ 52 °C. • - glycoprotein molecule, ∘ - hydration shell, ✶; - ice crystallite. Due to reduced thermal energy, increasing amounts of water become bound to glycoprotein molecules (leaving less free water) and the hydration shells swell. As a result, there is an increase in viscosity and a decrease in configurational entropy. For -11.0 °C < T ≤ -2.5 °C, ice crystallites bound to glycoproteins are present in solution.

due to its density being lower than that of the liquid phase. This is contrary to observations as we see definitive evidence for the presence of ice in solution in mucus Brillouin spectra in the form of a peak at a frequency shift corresponding to that of pure ice Ih. Furthermore, the non-negligible contribution of scattering to hypersound attenuation below the transition temperature is compelling indirect evidence that ice crystallites are present in solution. This model of freezing is also supported by the results of THz absorption spectroscopy work which show that the diameter of the hydration shell of antifreeze glycoproteins from *Dissostichus Mawsoni* increases with decreasing temperature for 5 °C ≥ T ≥ 20 °C [49]. This, along with the fact that complexation of the glycoprotein with borate shifted the hydration dynamics towards that of free water, lead the authors to propose that long-range water-protein interactions contribute significantly to antifreeze activity. Moreover, molecular dynamics simulations show that even an increase in hydration shell diameter of a few Å can result in nearly all water being bound [7, 40, 52], thereby leaving little to no free water to freeze at or near the 'equilibrium' freezing point. It is conceivable, of course, that ice could be nucleating on the sides of the cell and that this is the source of our 'ice' signal but this is unlikely given that its density is lower than that of liquid water and because we have three independent but nominally identical samples that behave essentially the same way.

4.6 Conclusion

The GHz-frequency viscoelastic properties and phase behaviour of a natural gastropod mucus were probed over the temperature range -11 °C $\leq T \leq$ 52 °C by Brillouin light scattering spectroscopy. Anomalies in the temperature dependence of spectral peak parameters and derived viscoelastic properties reveal the inception of a previously uncharacterized liquid-to-solid phase transition at -2.5°C, with coexistence of liquid mucus and solid ice persisting to at least -11 °C. The gradual nature of this transition and the observed temperature dependence of the apparent viscosity and hypersound attenuation is attributed to water-glycoprotein interaction, primarily that related to water binding to glycoprotein, reducing the ability of these bound water molecules to reconfigure and to crystallize to form ice. This work gives new insight into role of bound water in biologically-important protein-water systems and also demonstrates the utility of Brillouin spectroscopy in the study of this unique class of natural materials, extending further the range of systems to which this technique has been productively applied.

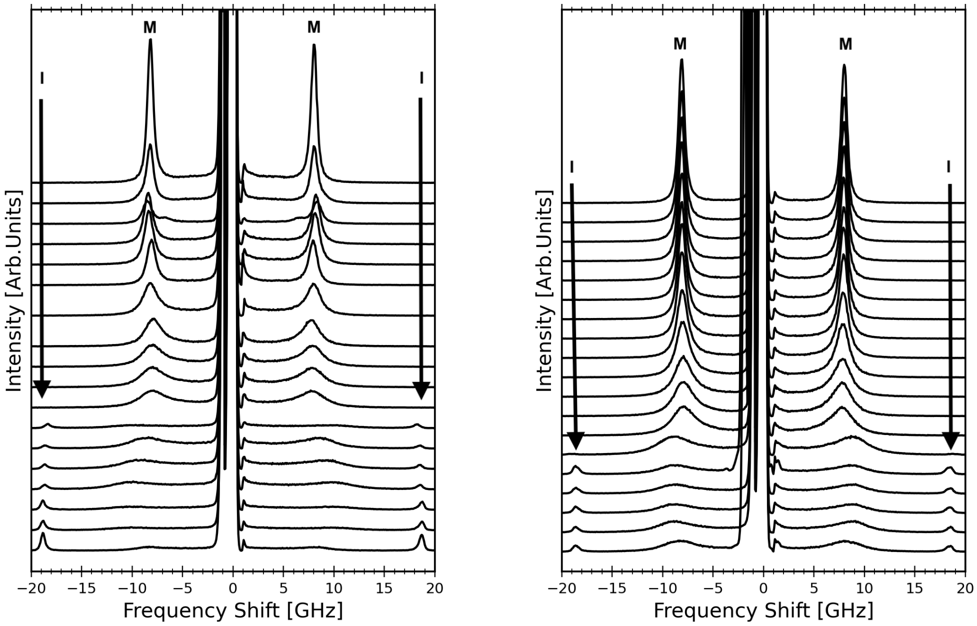

Figure 4.11: Brillouin spectra of a natural snail mucus collected at the indicated temperatures. Left - Sample #1; Right - Sample #3.

4.7 Supplementary Material for: Temperature Dependence of the Viscoelastic Properties of a Natural Gastropod Mucus by Brillouin Light Scattering Spectroscopy

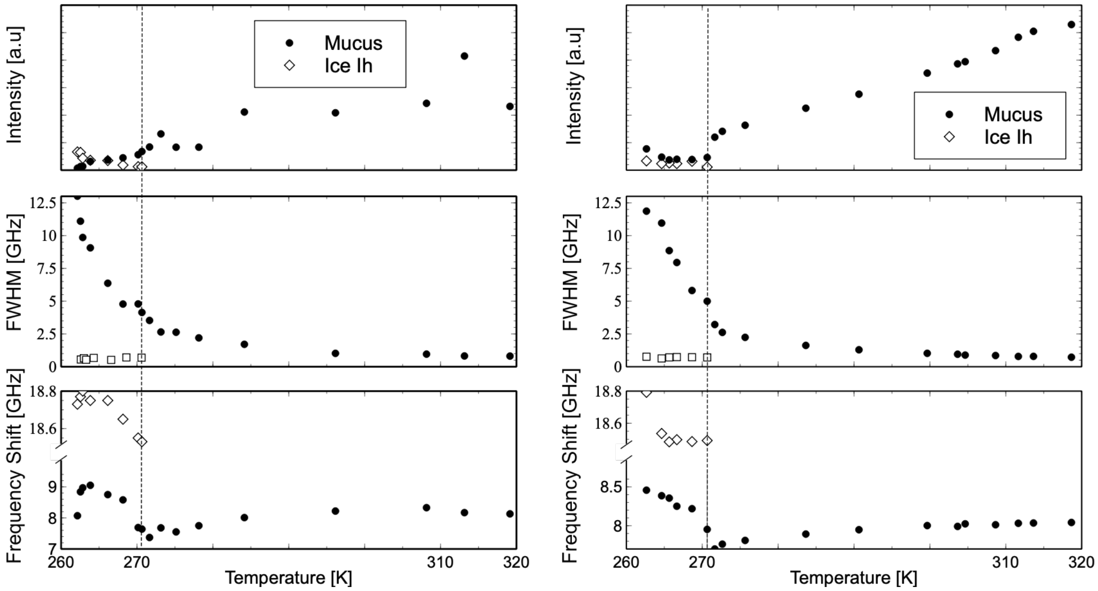

Figure 4.12: Temperature dependence of integrated intensity, linewdith (FWHM), and frequency shift of Brillouin peaks for a natural snail mucus. Left - Sample #1; Right - Sample #3. The dashed vertical line indicates the phase transition at -2.5 °C.

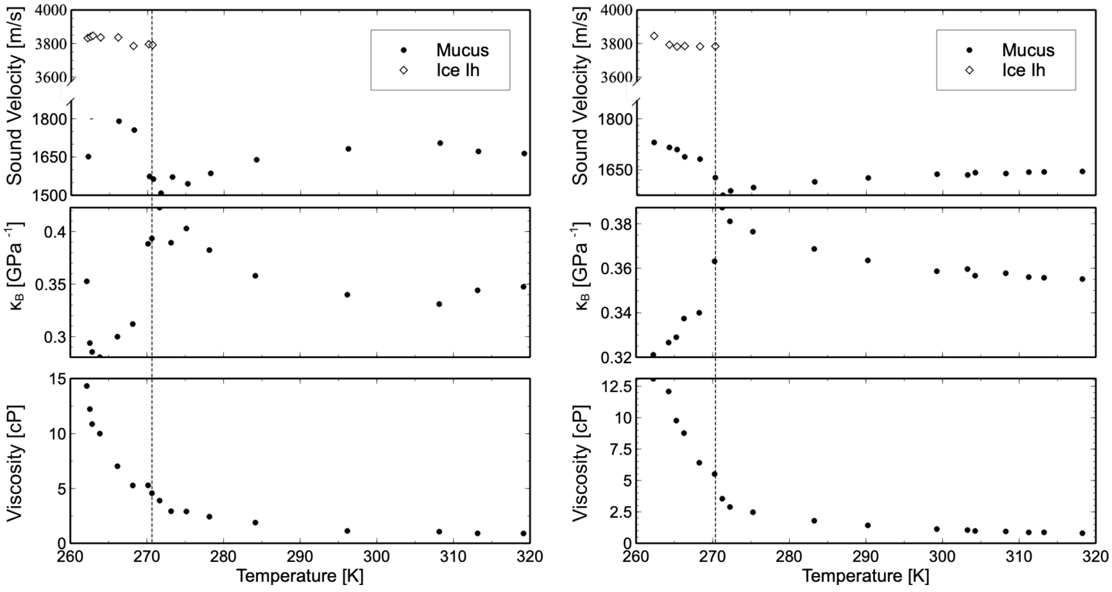

Figure 4.13: Temperature dependence of hypersound velocity, adiabatic compressibility, and apparent viscosity of a natural snail mucus. Left - Sample #1; Right - Sample #3. The dashed vertical line indicates the phase transition at -2.5 °C.

Table 4.5: Brillouin peak frequency shift (f_M, f_I), full width at half-maximum (Δf_M, Δf_I), and intensity (I_M, I_I) for Sample #1 at the indicated temperatures. M - liquid mucus phase; and I - ice-like solid phase.

T [±0.5 K]	T [±0.5°C]	f_M [±0.3 GHz]	f_I [±0.1 GHz]	Δf_M [GHz]	Δf_I [±0.3 GHz]	I_M [Arb. Units]	I_I [Arb. Units]
324.0	51.0	8.1	—	0.7(3)	—	13080(10)	—
319.0	46.0	8.1	—	0.8(3)	—	5800(10)	—
313.0	40.0	8.2	—	0.8(3)	—	10374(10)	—
308.0	35.0	8.3	—	1.0(3)	—	6080(10)	—
296.0	23.0	8.2	—	1.0(3)	—	5220(10)	—
284.0	11.0	8.0	—	1.7(3)	—	5280(10)	—
278.0	5.0	7.8	—	2.2(3)	—	2090(10)	—
275.0	2.0	7.6	—	2.6(3)	—	2090(10)	—
273.0	0.0	7.7	—	2.7(4)	—	3200(20)	—
272.0	-1.5	7.4	—	3.5(5)	—	2110(20)	—
271.0	-2.5	7.6	18.5	4.1(5)	0.5	1700(20)	—
270.0	-3.0	7.7	18.6	4.8(3)	0.5	1410(20)	320(20)
268.0	-5.0	8.6	18.5	5(1)	0.5	1130(20)	460(20)
266.0	-7.0	8.8	18.8	6(2)	0.6	930(20)	870(20)
263.7	-9.3	9.1	18.8	9(2)	0.6	790(20)	900(20)
262.7	-10.3	9.0	18.8	10(2)	0.5	350(20)	1090(10)
262.4	-10.6	8.8	18.9	11(3)	0.5	230(30)	1620(10)
262.0	-11.0	8.1	18.7	13(4)	0.5	180(30)	1660(10)

Table 4.6: Brillouin peak frequency shift (f_M, f_I), full width at half-maximum (Δf_M, Δf_I), and intensity (I_M, I_I) for Sample #2 at the indicated temperatures. M - liquid mucus phase; and I - ice-like solid phase.

T [±0.5 K]	T [±0.5°C]	f_M [±0.3 GHz]	f_I [±0.1 GHz]	Δf_M [GHz]	Δf_I [±0.3 GHz]	I_M [Arb. Units]	I_I [Arb. Units]
322.0	49.0	8.1	—	0.6(2)	—	10070(10)	—
317.0	44.0	8.1	—	0.7(2)	—	9350(10)	—
316.0	43.0	8.0	—	0.7(2)	—	8720(10)	—
312.0	39.0	8.0	—	0.8(3)	—	7990(10)	—
310.0	37.0	8.0	—	0.8(2)	—	8150(10)	—
307.0	34.0	8.0	—	0.8(3)	—	6770(10)	—
306.0	33.0	8.0	—	0.9(3)	—	8130(10)	—
303.0	30.0	8.0	—	1.0(3)	—	6830(10)	—
301.0	28.0	8.0	—	0.9(3)	—	7800(10)	—
298.0	25.0	8.0	—	1.0(3)	—	6500(10)	—
296.0	23.0	8.0	—	0.9(3)	—	8330(20)	—
288.0	15.0	7.9	—	1.4 (3)	—	4770(10)	—
280.0	7.0	7.8	—	1.9(3)	—	3710(20)	—
274.0	1.0	7.7	—	2.6(3)	—	2910(20)	—
272.0	-1.0	7.7	—	2.9(4)	—	2710(30)	—
270.5	-2.5	7.6	—	3.6(4)	—	2220(30)	—
270.0	-3.0	7.9	18.6	5.8(5)	0.7	1080(30)	320(10)
267.0	-6.0	8.2	18.6	7.4(5)	0.7	1120(30)	350(10)
266.0	-7.0	8.6	18.7	9(2)	0.5	920(30)	370(10)
264.0	-9.0	8.4	18.7	10(2)	0.7	910(40)	380(10)
262.7	-10.3	8.6	18.8	11(2)	0.5	430(40)	890(10)
262.4	-10.6	8.6	18.7	12(3)	0.7	430(40)	750(10)
262.0	-11.0	8.4	18.8	13(3)	0.6	310(40)	1650(10)

Table 4.7: Brillouin peak frequency shift (f_M, f_I), full width at half-maximum (Δf_M, Δf_I), and intensity (I_M, I_I) for Sample #3 at the indicated temperatures. M - liquid mucus phase; and I - ice-like solid phase.

T [±0.5 K]	T [±0.5°C]	f_M [±0.3 GHz]	f_I [±0.1 GHz]	Δf_M [GHz]	Δf_I [±0.3 GHz]	I_M [Arb. Units]	I_I [Arb. Units]
323.0	50.0	8.1	—	0.7(3)	—	14570(20)	—
318.0	45.0	8.0	—	0.7(3)	—	13240(20)	—
313.0	40.0	8.0	—	0.8(3)	—	12620(20)	—
311.0	38.0	8.0	—	0.8(3)	—	12070(20)	—
308.0	35.0	8.0	—	0.9(6)	—	10860(20)	—
304.0	31.0	8.0	—	0.9(5)	—	9860(20)	—
303.0	30.0	8.0	—	1.0(5)	—	9660(20)	—
299.0	26.0	8.0	—	1.0(4)	—	8820(20)	—
290.0	17.0	7.9	—	1.3(5)	—	6910(20)	—
283.0	10.0	7.9	—	1.6(5)	—	5630(30)	—
275.0	2.0	7.8	—	2.2(6)	—	4080(30)	—
272.0	-1.0	7.8	—	2.6(5)	—	3530(30)	—
271.0	-2.5	7.7	—	3.2(6)	—	3000(20)	—
270.0	-3.0	8.0	18.5	5(1)	0.7	1150(30)	290(10)
268.0	-5.0	8.2	18.5	6(2)	0.7	970(30)	810(10)
266.0	-7.0	8.3	18.5	8(2)	0.7	990(30)	600(10)
265.0	-8.0	8.4	18.5	9(2)	0.7	930(30)	650(10)
264.0	-9.0	8.4	18.6	11(3)	0.6	1190(30)	590(10)
262.0	-11.0	8.5	18.8	12(4)	0.8	1940(30)	840(10)

Bibliography

[1] M. W. Denny. The role of gastropod pedal mucus in locomotion. *Nature*, 285(5761):160–161, 1980.

[2] M. W. Denny. Mechanical properties of pedal mucus and their consequences for gastropod structure and performance. *Am. Zool.*, 24(1):23–36, 1984.

[3] P. Verdugo, I. Deyrup-Olsen, M. Aitken, M. Villalon, and D. Johnson. Molecular mechanism of mucin secretion: I. the role of intragranular charge shielding. *J. Dent. Res.*, 66(2):506–508, 1987.

[4] Y. Liao, N. A. Clark, and P. S. Pershan. Brillouin scattering from smectic liquid crystals. *Phys. Rev. Lett.*, 30(14):639–641, 1973.

[5] C. Grammes, J. K. Kruger, K. P. Bohn, J. Baller, C. Fischer, C. Schorr, D. Rogez, and P. Alnot. Universal relaxation behaviour of classical liquid crystals at hypersonic frequencies. *Phys. Rev. E*, 51(1):430–440, 1995.

[6] L. Ye, J. Liu, P. Sheng, J. S. Huang, and D. A. Weitz. Sound propagation in colloidal systems. *J. de Phys. IV*, 3:183–196, 1993.

[7] K. Meister, S. Ebbinghaus, Y. Xu, A. DeVries, M. Gruebele, D. M. Leitner, and M. Havenith. Long-range protein-water dynamics in hyperactive insect antifreeze proteins. *Proc. Natl. Acad. Sci.*, 110(5):1617–1622, 2013.

[8] J. Li, A. D. Celiz, J. Yang, Q Yang, I. Wamala, W. Whyte, B. R. Seo, N. V. Vasilyev, J. J. Vlassak, and Z. Suo. Tough adhesives for diverse wet surfaces. *Science*, 357(6349):378–381, 2017.

[9] V. Bouvet and R. N. Ben. Antifreeze glycoproteins: Structure, conformation, and biological applications. *Cell Biochem. Biophys.*, 39:133–144, 2003.

[10] C. S. Kwan, A. R. Cerullo, and A. B. Braunschweig. Design and synthesis of mucin-inspired glycopolymers. *ChemPlusChem*, 85:2704–2721, 2020.

[11] J. Rouch, C. C. Lai, and S. H. Chen. Brillouin scattering studies of normal and supercooled water. *J. Chem. Phys.*, 65(10):4016–4021, 1976.

[12] J. G. Dil. Brillouin scattering in condensed matter. *Rep. Prog. Phys.*, 45(3):285, 1982.

[13] M. Bailey, M. Alunni-Cardinali, N. Correa, S. Caponi, T. Holsgrove, H. Barr, N. Stone, C. P. Winlove, D. Fioretto, and F. Palombo. Viscoelastic properties of biopolymer hydrogels determined by brillouin spectroscopy: A probe of tissue micromechanics. *Sci. Adv.*, 6(44):eabc1937, 2020.

[14] D. F. Hanlon, M. J. Clouter, and G. T. Andrews. Influence of hydration and dehydration on the viscoelastic properties of snail mucus by brillouin spectroscopy, 2023.

[15] R. E. Gagnon, H. Kiefte, M. J. Clouter, and E. Whalley. Pressure dependence of the elastic constants of ice ih to 2.8 kbar by Brillouin spectroscopy. *J. Chem. Phys.*, 89:4522–4528, 1988.

[16] P. H. Gammon, H. Kiefte, M. J. Clouter, and W. W. Denner. Elastic constants of artificial and natural ice samples by brillouin spectroscopy. *J. Glaciol.*, 29(103):433–460, 1983.

[17] James D Brownridge. When does hot water freeze faster then cold water? a search for the mpemba effect. *Am. J. Phys.*, 79(1):78–84, 2011.

[18] G. T. Andrews. Acoustic characterization of porous silicon. In L. Canham, editor, *Handbook of Porous Silicon*, chapter 53, pages 691–703. Springer International, 2018.

[19] E. Gugliando, M. Cordaro, R. Fusco, A. F. Peritore, R. Siracusa, T. Genovese, R. D'Amico, D. Impellizzeri, R. DiPaola, S. Cuzzocrea, and R. Crupi. Protective effect of snail secretion filtrate against ethanol-induced gastric ulcer in mice. *Sci. Rep.*, 11:3638, 2021.

[20] C. L. O'Connor and J. P Schlupf. Brillouin scattering in water: the landau—placzek ratio. *J. Chem. Phys.*, 47(1):31–38, 1967.

[21] A. H. Harvey, J. S. Gallagher, and J. M. H. Levelt Sengers. Revised formulationfor the refractive index of water and steam as a function of wavelength, temperature, and density. *J. Phys. Chem. Ref. Data*, 27(4):761–774, 1998.

[22] D. E. Hare and C. M. Sorensen. The density of supercooled water. ii. bulk samples cooled to the homogeneous nucleation limit. *J. Chem. Phys.*, 87(8):4840–4845, 1987.

[23] D. E. Hare and C. M. Sorensen. Optical constants of ice from the ultraviolet to the microwave. *Appl. Opt.*, 23(8):1206–1225, 1984.

[24] P. H. Gammon, H. Kiefte, and M. J. Clouter. Elastic constants of ice samples by Brillouin spectroscopy. *J. Phys. Chem.*, 87(21):4025–4029, 1983.

[25] P. H. Gammon, H. Kiefte, and M. J. Clouter. Elastic constants of ice by Brillouin spectroscopy. *J. Glaciol.*, 25(91):159–168, 1980.

[26] R. E. Gagnon, H. Kiefte, M. J. Clouter, and E. Whalley. Acoustic velocities and densities of polycrystalline ice ih, ii, iii, v, and vi by Brillouin spectroscopy. *J. Chem. Phys.*, 92(3):1909–1914, 1990.

[27] J. Teixeira and J. Leblond. Brillouin scattering from supercooled water. *J. de Phys. Lett.*, 39(7):83–85, 1978.

[28] P. Spickler, F. Ibrahim, S. Fast, D. Tannenbaum, S. Yun, and F. B. Stumpf. Ultrasonic velocity and absorption in binary solutions of poly(ethylene oxide) with water. *J. Acoust. Soc. Am.*, 83(4):1388–1389, 1988.

[29] P. Spickler, I. Abdelraziq, S. Yun, and F. B. Stumpf. Velocity and absorption of ultrasound in binary solutions of polyvinylpyrrolidone and water. *J. Acoust. Soc. Am.*, 85(3):1363–1364, 1989.

[30] J. H. So, R. Esquivel-Sirvent, S. S. Yun, and F. B. Stumpf. Ultrasonic absorption and velocity measurements for poly (vinyl alcohol) and water solutions. *J. Acoust. Soc. Am.*, 96(6):3807–3808, 1994.

[31] J. H. So, R. Esquivel-Sirvent, S. S. Yun, and F. B. Stumpf. Ultrasonic velocity and absorption measurements for poly(acrylic acid) and water solutions. *J. Acoust. Soc. Am.*, 98(1):659–660, 1995.

[32] R. Esquivel-Sirvent, B. Tan, I. Abdelraziq, S. S. Yun, and F. B. Stumpf. Absorption and velocity of ultrasound in binary solutions of poly (ethylene glycol) and water. *J. Acoust. Soc. Am.*, 93(2):819–820, 1993.

[33] R. Esquivel-Sirvent, S. S. Yun, and F. B. Stumpf. Absorption and velocity of ultrasound in binary solutions of poly (sodium 4-styrenesulfonate) and water. *J. Acoust. Soc. Am.*, 95(1):557–558, 1994.

[34] M. F. Haque and F. B. Stumpf. Velocity of ultrasound in binary solutionso of polyacrylamide with water. *J. Acoust. Soc. Am.*, 73(1):365–366, 1983.

[35] J. A. Raymond and A. L. DeVries. Adsorption inhibition as a mechanism of freezing resistance in polar fishes. *Proc. Natl. Acad. Sci.*, 74:2589–2593, 1977.

[36] M. J. Vaughan, K. van Wijk, D. J. Prior, and M. H. Bowman. Measurement of the bulk viscosity of liquid by Brillouin scattering. *The Cryosphere*, 10:2821–2829, 2016.

[37] MJ Holmes, NG Parker, and MJW Povey. Temperature dependence of bulk viscosity in water using acoustic spectroscopy. In *J. Phys.: Conf. Series*, volume 269, page 012011. IOP Publishing, 2011.

[38] Peter G Brewer, Edward T Peltzer, and Kathryn Lage. Life at low reynolds number re-visited: The apparent activation energy of viscous flow in sea water. *Deep Sea Research Part I: Oceanographic Research Papers*, 176:103592, 2021.

[39] Marco Paolantoni, Paola Sassi, Assunta Morresi, and Sergio Santini. Hydrogen bond dynamics and water structure in glucose-water solutions by depolarized rayleigh scattering and low-frequency raman spectroscopy. *J. Chem. Phys.*, 127(2):07B606, 2007.

[40] L Lupi, L Comez, C Masciovecchio, A Morresi, M Paolantoni, P Sassi, F Scarponi, and D Fioretto. Hydrophobic hydration of tert-butyl alcohol studied by brillouin light and inelastic ultraviolet scattering. *J. Chem. Phys.*, 134(5):02B603, 2011.

[41] F Bencivenga, A Cimatoribus, A Gessini, MG Izzo, and C Masciovecchio. Temperature and density dependence of the structural relaxation time in water by inelastic ultraviolet scattering. *J. Chem. Phys.*, 131(14):144502, 2009.

[42] GDLG Monaco, D Fioretto, L Comez, and G Ruocco. Glass transition and density fluctuations in the fragile glass former orthoterphenyl. *Phys. Rev. E*, 63(6):061502, 2001.

[43] M Pochylski, F Aliotta, Z Błaszczak, and J Gapiński. Structural relaxation processes in polyethylene glycol/ccl4 solutions by brillouin scattering. *J. Phys. Chem. B*, 109(9):4181–4188, 2005.

[44] Francesca Palombo and Daniele Fioretto. Brillouin light scattering: applications in biomedical sciences. *Chem. Rev.*, 119(13):7833–7847, 2019.

[45] L Comez, M Paolantoni, P Sassi, S Corezzi, A Morresi, and D Fioretto. Molecular properties of aqueous solutions: a focus on the collective dynamics of hydration water. *Soft Matter*, 12(25):5501–5514, 2016.

[46] Jean-Pierre Hansen and Ian Ranald McDonald. *Theory of Simple Liquids: With Applications to Soft Matter*. Academic press, 2013.

[47] Lucia Comez, Claudio Masciovecchio, Giulio Monaco, and Daniele Fioretto. Progress in liquid and glass physics by brillouin scattering spectroscopy. In *Solid State Physics*, volume 63, pages 1–77. Elsevier, 2012.

[48] L Comez, L Lupi, M Paolantoni, F Picchiò, and D Fioretto. Hydration properties of small hydrophobic molecules by brillouin light scattering. *J. Chem. Phys.*, 137(11):114509, 2012.

[49] S. Ebbinghaus, K. Meister, B. Born, A. L. DeVries, M. Gruebele, and M. Havenith. Antifreeze glycoprotein activity correlates with long-range protein-water dynamics. *J. Am. Chem. Soc.*, 132(35):12210–12211, 2010.

[50] Z. Jia, C. I. DeLuca, H. Chao, and P. L. Davies. Structural basis for the binding of a globular antifreeze protein to ice. *Nature*, 384:285–288, 1996.

[51] C. A. Knight, C. C. Cheng, and A. L. DeVries. Adsorption of α-helical antifreeze peptides on specific ice crystal surface planes. *Biophys. J.*, 59:409–418, 1991.

[52] V. Conti-Nibali, G. D'Angelo, A. Paciaroni, D. J. Tobias, and M. Tarek. On the coupling between the collective dynamics of proteins and thier hydration water. *J. Phys. Chem. Lett.*, 5:1181–1186, 2014.

Chapter 5

Influence of Hydration and Dehydration on the Viscoelastic Properties of Snail Mucus by Brillouin Spectroscopy

D. F. Hanlon, M. J. Clouter, and G. T. Andrews

Co-Authorship Statement

We, the authors of this manuscript, have contributed collectively to the research, writing, and preparation of this work. Each author's contribution is outlined below:

D. F. Hanlon: Writing, Data Collection, Data Analysis, and Editing.

M. J. Clouter: Writing, Data Collection, Data Analysis, Editing, and Supervision.

G. T. Andrews: Writing, Data Collection, Data Analysis, Editing, Supervision, Conceived and Administered Experiment.

5.1 Abstract

Brillouin spectroscopy was used to probe the viscoelastic properties of diluted snail mucus at GHz frequencies over the range -11 °C ≤ T ≤ 52 °C and of dehydrated mucus as a function of time. Two peaks were observed in the spectra for diluted mucus: the longitudinal acoustic mode of the liquid mucus peak varies with dilution but fluctuates around the typical value of 8.0 GHz. A second peak due to ice remained unchanged with varying dilution and was seen at 18.0 GHz and appeared below the dilutions "freezing" point depression. Only a single peak was found in all the dehydrated mucus spectra and was also attributed to the longitudinal acoustic mode of liquid mucus. Anomalous changes in the protein concentration dependence of the frequency shift, linewidth, and "freezing" point depression and consequently, hypersound velocity, compressibility, and apparent viscosity suggest that the viscoelastic properties of this system is influenced by the presence of water. Furthermore, this research uncovered three unique transitions within the molecular structure. These transitions included the first stage of glycoprotein cross-linking, followed by the steady depletion of free water in the system, and eventually resulted in the creation of a gel-like state when all remaining free water was evaporated.

5.2 Introduction

In recent years, there has been a growing interest in exploring the mechanical properties of polymer-water solutions, driven by their significance in understanding the functional characteristics of proteins [1–4]. Previous research however has primarily focused on rheological studies of natural snail mucus [5, 6]. Recent studies on natural snail mucus used Brillouin light scattering spectroscopy to investigate the effect of temperature on its viscoelastic properties [7]. The findings in that work revealed that snail mucus exhibits increased viscoelastic properties, such as the sound velocity, storage and loss moduli, as well as apparent viscosity, in comparison to water. The study also discovered a phase transition in which the viscous liquid state of snail mucus shifts to a condition in which both liquid mucus and solid ice phases coexist. This work sheds light on the peculiar behaviour of snail mucus under different temperature conditions. The results of this study imply that the glycoprotein-water interaction is responsible for the increased viscoelastic behaviour and phase change observed in snail mucus. The results of this Brillouin scattering investigation, as well as prior rheological experiments, clearly indicate that the cross-linked network of glycoproteins in snail mucus is the major reason of the increase in mechanical properties such as the speed of sound, and viscosity reported in snail mucus [5–7]. The previous Brillouin light scattering study, while it does investigate the temperature dependence of the system, it does not explore how the glycoprotein concentration influences the mechanical properties of snail mucus. While a number of studies in the past have explored the viscoelastic properties of polymer-water systems, the impact of glycoprotein concentration on the viscoelastic properties such as complex modulus, sound velocity, and apparent viscosity still remains poorly understood [1–4].

Snail mucus is a polymer-water solution composed of long chains of high molecular weight glycoproteins in water. These glycoproteins are known to to cross-link in the mucus. The direct mechanism for cross-linking in this specific system is unknown but is likely due to covalent and non-covalent interactions such as through disulfide and hydrogen bonds. Protein concentrations in these solutions were previously reported in the literature to range from 3 - 7% proteins by weight, with the remaining composition consisting of water [5, 6, 8]. The interaction between proteins and water plays a significant role in the functionality of these polymer-water solutions and holds important implications for various technological advancements. Active research is being conducted in the field of hydrogels, which are being explored for their potential as non-toxic medical adhesives [9]. A comprehensive understanding of the limitations associated with these hydrogels is essential for their effective fabrication in medical applications. Furthermore, the cryoprotectants field is actively exploring polymer-water solutions, particularly antifreeze glycoproteins, as potential substitutes for traditional cryoprotectants. These solutions exhibit the capability to significantly reduce the freezing temperature, even at low concentrations, thereby presenting exciting prospects for cryopreservation applications [10, 11]. In recent years, there has been a increased research focused on protein-water solutions to gain a deeper understanding of the dynamics of water in the vicinity of proteins with emphasis on understanding the interesting behavior of water molecules surrounding proteins and their interactions [2–4, 12, 13].

In this paper, Brillouin light scattering spectroscopy was used to characterize the temperature dependence of diluted snail mucus as a function of glycoprotein concentration over the range -11 °C to 52 °C. We report values for sound velocity, storage (bulk) moduli, apparent viscosity, and hypersound absorption for all dilutions as a function of temperature. Additionally, we show the influence of hydration on the previously discovered freezing point depression attributed to the presence of glycoproteins [7]. Furthermore, we investigate the influence of dehydration on the viscoelastic properties of snail mucus by allowing the mucus to naturally dehydrate over the course of ~ 400 hours. The results of these two experiments build upon previously published data on the viscoelastic properties of natural snail mucus, offering new insights into the physics of aqueous glycoprotein solutions and shedding light on the role of glycoproteins in the phase behavior of these systems [7]. In a wider context, the present study enhances our understanding of phonon dynamics in complex fluids, unraveling the complex interplay between water and biomacromolecules, and illuminating the significance of glycoproteins in biological systems.

5.3 Methodology

5.3.1 Brillouin Light Scattering Spectroscopy

Brillouin Scattering in Liquids

Brillouin light scattering spectroscopy is an inelastic light scattering technique which measures random thermal density fluctuations in liquids. The intensity of light inelastically scattered by aqueous solutions given by $\mathrm{I}_q(\omega)$, with exchanged wave vector q, is dominated by density fluctuations in the medium, which can be derived from the theoretical framework of hydrodynamics [14–16]. The intensity can be represented with the following expression,

$$I_q(\omega) \propto S_q = \frac{S_q M_0}{\pi \omega_B} \frac{M''}{[M' - \rho\omega_B^2/q^2]^2 + [M'']^2}, \tag{5.1}$$

where S_q is the static structure factor, ρ is the mass density, M_0 is the relaxed (zero-frequency) longitudinal acoustic modulus, $q = (4\pi/\lambda)n\sin(\theta/2)$, n is the refractive index of the medium, (here assumed constant at $n = 1.34$ [17]) and θ is the scattering angle. Additionally, ω is the angular frequency of the density fluctuations, and ω_B is the angular frequency of the density fluctuations obtained through Brillouin scattering. The complex longitudinal modulus, $M(\omega) = M'(\omega) + iM''(\omega)$, often referred to as the complex modulus, can be obtained directly via Brillouin spectroscopy using the following relations [1],

$$M = M' + iM'' = \frac{\lambda_i^2 \rho}{4n^2} f_B^2 + i\frac{\lambda_i^2 \rho}{8\pi n^2} f_B \Gamma_B, \tag{5.2}$$

where Γ_B is the full width at half maximum (FWHM) and M' is referred as storage modulus and is a measure of how much energy is stored elastically in the system. The loss modulus, M'', is a measure of how much energy is lost through heat in the system. M' and M'' can be expressed in terms of sound velocity v and apparent viscosity $\eta = 4\eta_s/3 + \eta_b$, where η_s and η_b are the shear and bulk viscosity, respectively, can be represented by the following,

$$M' = \rho v^2 \tag{5.3}$$

and

$$M'' = 2\pi\eta f_B \tag{5.4}$$

For a 180° backscattering geometry used in the present work, application of energy and momentum conservation to the scattering process reveals that the phonon velocity, v, and frequency shift of the incident light, f, are related by

$$v = \frac{f\lambda_i}{2n}, \tag{5.5}$$

where n is the refractive index of the target material at the incident light wavelength λ_i.

The spectral width of the Brillouin peaks is determined by the time that each fluctuation interacts with the incident light, thus measuring its lifetime (thermal relaxation) or the attenuation of these fluctuations [18]. Using both the frequency shift and FWHM, the frequency-independent sound absorption coefficient can be calculated using the following [19],

$$\frac{\alpha}{f^2} = \frac{\Gamma_B}{2v f_B^2}. \tag{5.6}$$

where, f_B, and Γ_B are directly obtained from the Brillouin spectra, and v is is calculated from Eq. 5.5.

Apparatus

Brillouin spectra were obtained using a 180° backscattering geometry using the experimental setup described previously in Ref. [20]. A Nd:YVO$_4$ single mode laser provided light of wavelength λ_i = 532 nm and power of 100 mW, which was directed onto the samples inside a temperature-controlled sample chamber described in great detail previously [7]. A high-quality anti-reflection-coated camera lens of focal length f = 5 cm and $f/\#$ = 2.8 served to both focus incident light onto the sample and to collect light scattered by it. After exiting this lens, the scattered light was focused by a 40 cm lens onto the 450 μm-diameter input pinhole of an actively-stabilized 3+3 pass tandem Fabry-Perot interferometer (JRS Scientific Instruments). The interferometer had a free spectral range of 30 GHz, and possessed a finesse of approximately 100. The light transmitted by the interferometer was directed onto a pinhole with a diameter of 700 μm and subsequently detected by a low-dark count ($\lesssim 1$ s^{-1}) photomultiplier tube where it was converted to an electrical signal and sent to a computer for storage and display.

Spectral Peak Analysis

Peak parameters including frequency shifts, and linewidths (FWHM), were obtained by fitting Lorentzian functions to the Stokes and anti-Stokes peaks and averaging the resulting parameters of best-fit. To obtain spectral linewidths, the instrumental linewidth of 0.3 GHz was subtracted from FWHM values obtained from the fits. Estimated uncertainties in peak parameters were also obtained from the uncertainty in the fits.

5.3.2 Attenuated Total Reflectance IR Spectroscopy

Theory

Fourier Transform Infrared (FTIR) spectroscopy, a type of vibrational spectroscopy, is a technique used to obtain an infrared spectrum of absorbance or emission of a solid, liquid or gas [21]. This technique allows for the identification and characterization of various chemical compounds which makes it useful in understanding the structure of complex liquid systems and is often used in conjunction with other spectroscopy techniques in order to characterize different samples [21–24]. The technique employs a Michelson interferometer to acquire IR spectra of the material. FTIR data is commonly gathered through an attenuated total reflectance (ATR) method. The ATR technique utilizes a crystal prism, such as diamond or zinc selenide, in direct contact with the sample [25]. In this method, the infrared radiation is directed onto the prism at a precise angle, subsequently undergoing multiple internal reflections by the prism before being ultimately absorbed by the sample [25].

Apparatus

All data was collected using a Vertex 70v vacuum Fourier transform infrared (FTIR) spectrometer (Bruker, Billerica, MA, USA) with Platinum Diamond attenuated total reflectance (ATR) attachment and a globar (blackbody) light source. Data was collected using a KBr beam splitter (4000–400 cm^{-1}) with 2 cm^{-1} resolution.

Before each measurement, a background spectrum was first collected to calibrate the system. Each sample was collected by using a pipette to extract the mucus, which was then directly placed onto the ATR crystal. Approximately 0.5 ml of mucus was used for each sample to ensure complete coverage of the crystal surface.

Spectral Analysis

The data collection procedure involved initially collecting FTIR spectra on ultra-pure water, as depicted in Fig. 5.1. This spectra served as a "baseline" for all subsequent spectra obtained for diluted and dehydrated mucus. ATR spectra were initially collected on pure snail mucus and showed very good agreement with spectra previously obtained for gastropod mucus. Furthermore, ATR spectra were collected on all diluted mucus samples. As for the dehydrated mucus, spectra were only collected after a noticeable change in Brillouin data was observed. Additionally, the presence of proteins in the snail mucus is indicated by the arrow in Fig. 5.1.

FTIR data in this work are displayed according to the common convention of ATR intensity versus wave number, where the wave numbers are displayed with decreasing values from left to right. The concentration of pure mucus, diluted and dehydrated mucus was estimated by comparing the integrated intensity of water absorbance bands to the same bands visible in spectra of diluted and dehydrated mucus. The IR spectra were normalized to spectrum for ultra-pure water. Figure 5.1 shows FTIR spectra of ultra-pure water and pure mucus. Both spectra show three prominent absorbance bands ν_1, ν_2 and ν_3 (see Fig. 5.1) due to the symmetric O-H stretching, O-H bending (scissors) vibration and a combination band of ν_2 plus an additional motion of the molecule. These absorbance bands act as a fingerprint for water and can help in identifying the presence of water in various systems. Additionally, we see the presence of absorbance bands likely due to the proteins, as indicated by the arrow in Fig. 5.1.

Concentration Determination

One of the primary objectives of utilizing FTIR in this study was to estimate the concentration of water and proteins within the snail mucus. Prior research suggests that an accurate concentration can be determined by comparing the integrated intensity of the spectral water peak with that of an unidentified peak of some system containing water [26]. For example, Fig. 5.1 shows very similar ATR spectra, and by comparing the absorbance bands of water with those peaks at the same position in the mucus we can determine the concentration of protein and water present. The intensity of these absorbance peaks gives a sense of the abundance of molecules absorbing the IR radiation [27]. To obtain the integrated intensity, a Gaussian profile was used to fit to the absorbance bands shown in Fig. 5.2 since it has been used to properly fit the bands of cross-linked networks [28] (see Table S1 in Supplementary file for values extracted from ATR spectra).

In general, the shifts of all vibrational modes remained relatively constant, varying by only a few tens of wavenumbers. The FWHM for the ν_1 generally decreases with decreasing water concentration, ν_2 remains constant for most of the concentrations, and ν_3 increases with increasing concentration for those spectra where the peak is observed. The most obvious changes in Fig. 5.2 are with the spectral intensity. The vibrational mode ν_1 is the most intense throughout all spectra, and shows a general decrease from ultra-pure water to the spectra containing 45% water. The intensity of the ν_2 vibrational mode is relatively constant, showing only slight variations between 15-40 counts over the whole range studied. As well, the intensity of the vibrational mode at 2130 cm^{-1} remains constant throughout.

Density Determination

The density of each diluted and dehydrated mucus solution was determined using water and protein concentrations determined from ATR analysis and the following expression for the density of a two-component solution [1]:

$$\rho = \frac{m_W + m_M}{\frac{m_w}{\rho_w} + \frac{m_M}{\rho_M}}, \tag{5.7}$$

where m_W and m_M denote the mass of water and dry mucus, respectively, and ρ_W = 0.997 g/cm^3 [29] and ρ_M = 1.571 g/cm^3 are the corresponding mass densities. The dry mucus density ρ_M was obtained from Eq. 5.7 using the known density of natural snail mucus (ρ = 1.040 g/cm^3) determined in a previous study [7] and compositional information obtained through ATR analysis.

5.4 Dilution Experiments

5.4.1 Sample Preparation

The diluted snail mucus samples utilized in this study were prepared by combining natural snail mucus with ultra-pure water. To prevent dehydration, the mucus was initially stored in a sealed container. Using a syringe, 1 ml of mucus was extracted from the parent container and transferred to a glass sample cell that was sealed at one end. Ultra-pure water was added to the cell in 0.5 ml increments for each dilution. After water was added, the mucus-water solution was stirred with a stirring stick for 10 minutes to ensure proper mixing. This standardized procedure was followed for all

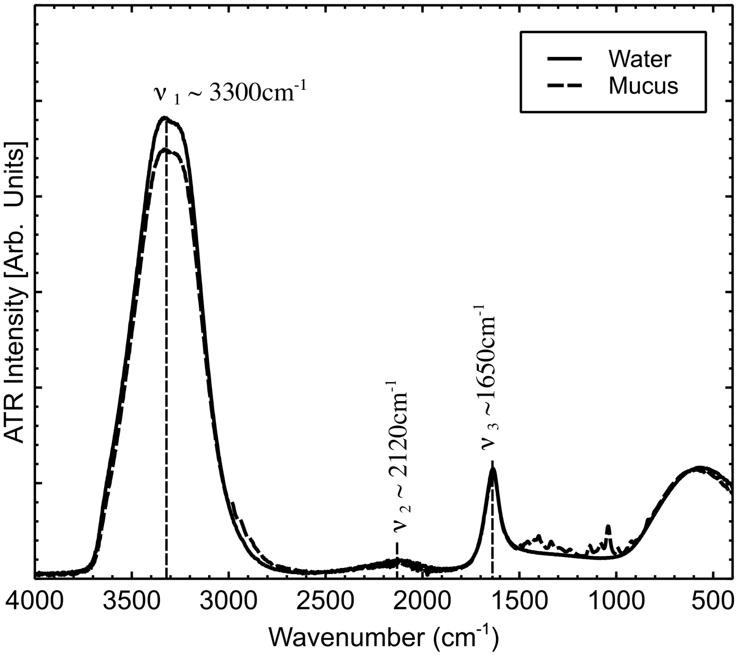

Figure 5.1: ATR spectra collected on ultra-pure water and pure snail mucus at room temperature.

dilutions to maintain consistency.

Following the mixing of solutions, the samples were left undisturbed to equilibrate for 6 hours. Brillouin spectra were collected as a function of temperature after each dilution. It should be noted that the glass sample cell had physical limitations, and the maximum amount of water that could be added was 2.5 ml. Additionally, an alternative sample was prepared by initially adding 0.5 ml of mucus first and then adding 1.5 ml of water. Once each sample was prepared, the glass sample cell was placed into the previously discussed temperature-controlled sample chamber [7].

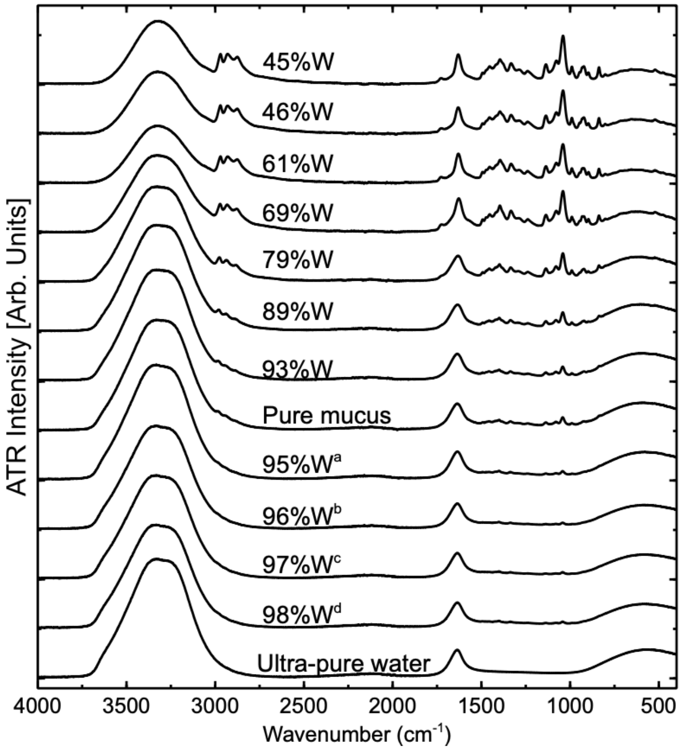

Figure 5.2: ATR-FTIR spectra of natural snail mucus. ATR spectra collected on diluted snail mucus are indicated by the superscripts $a - d$. The remaining spectra were collected on dehydrating mucus as a function of time.

5.4.2 Results: Raw Spectral Signatures

Figure 5.3 shows representative series of Brillouin spectra collected on diluted snail mucus for temperature ranging from -11.0°C - 50.0°C. Figure 5.4 shows the anti-stokes Brillouin peak for liquid mucus for all dilutions at room temperature displaying the general difference in spectra for each dilution. As evident from Fig. 5.4, as the dilution increases, the Brillouin shift decreases. In all dilutions there were two sets of Brillouin peaks present in the spectra, one of which occured at a shift of ~ 8.0 GHz which decreased to a value similar to that of water as the dilution increased. This peak was present over the entire temperature range for all dilutions; however, the spectral intensity of this peak decreased with increasing dilution for temperatures below the corresponding "freezing" point. A second peak occured at approximately

Table 5.1: Sample descriptions for Diluted Snail Mucus

	Dilution #1	Dilution #2	Dilution #2	Dilution #4
Total Volume (mL)	1.5 ± 0.1	2.0 ± 0.1	2.5 ± 0.1	1.5 ± 0.1
Protein Concentration (wt %)	5 ± 0.7	4 ± 0.6	3 ± 0.5	2 ± 0.2
Water Concentration (wt %)	95 ± 0.7	96 ± 0.6	97 ± 0.5	98 ± 0.2
Density (g/cm^3)	1.027 ± 0.007	1.020 ± 0.005	1.017 ± 0.005	1.013 ± 0.003

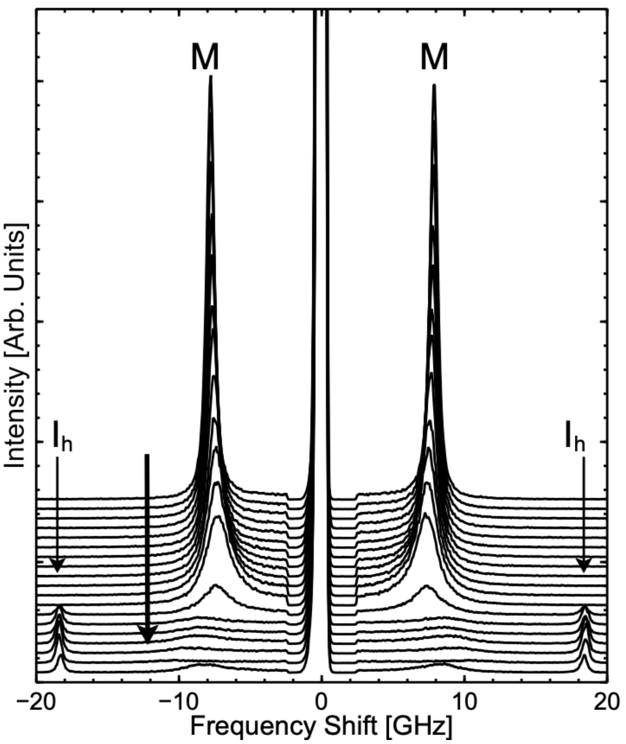

Figure 5.3: Temperature dependence of Brillouin spectra for diluted gastropod mucus with 5 wt% protein and 95 wt% water (Dilution #1 in Table 5.1). Direction of decreasing temperature is indicated by the large arrow second from left. **M** and $\mathbf{I}_\mathrm{h}$ identify peaks due to mucus and ice, respectively.

18.0 GHz and has previously been deemed due to the longitudinal acoustic modes of ice I_h [7]. Throughout this manuscript, the term "freezing" point is to indicate the point at which this "ice peak" appears in the spectrum.

Figure 5.5 shows the frequency shift as a function of temperature for all dilutions. For all dilutions there is a slight increase in the frequency shift for increasing temperatures greater than its freezing point. Below their respective freezing points however, dilutions 1-3 (see Table 5.1) all show a rapid increase in frequency shift with decreasing temperature. Dilution 4 on the other hand shows that below its "freezing" temperature, the frequency shift follows a similar trend to that of pure water, and decreases with decreasing temperature the data available in this region. This result suggests

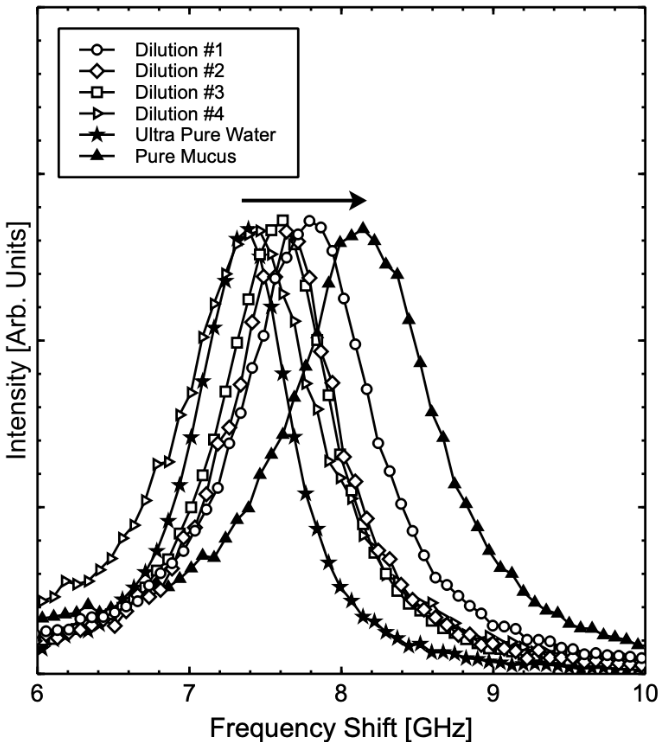

Figure 5.4: Room temperature Brillouin spectra (Anti-Stokes) of all diluted gastropod mucus samples. Arrow represents direction of increasing protein concentration.

that there is a transition occurring in dilution#4 that is disrupting the network of glycoproteins and water molecules present in snail mucus. This is further supported by the difference in frequency shift between the most dilute (Dilution #4) and least dilute (Dilution #1). This shows that for higher protein concentration (Dilution #1), the frequency shift resembles that of pure mucus Ref. [7], while the lowest protein concentration (Dilution #4) resembles that of ultra pure water Ref. [7]. Previous concentration dependent Brillouin studies on polymer gels shows a similar trend, that is at very low polymer concentrations the frequency shift is comparable to pure water, and at high concentrations the frequency shift is drastically different [30–32].

Figure 5.5 shows the FWHM as a function of temperature for all dilutions which for T ≥ 0 °C decreases with increasing temperature. Below, this temperature the FWHM in general increases. The inset figure shown in Fig. 5.5 shows the FWHM for

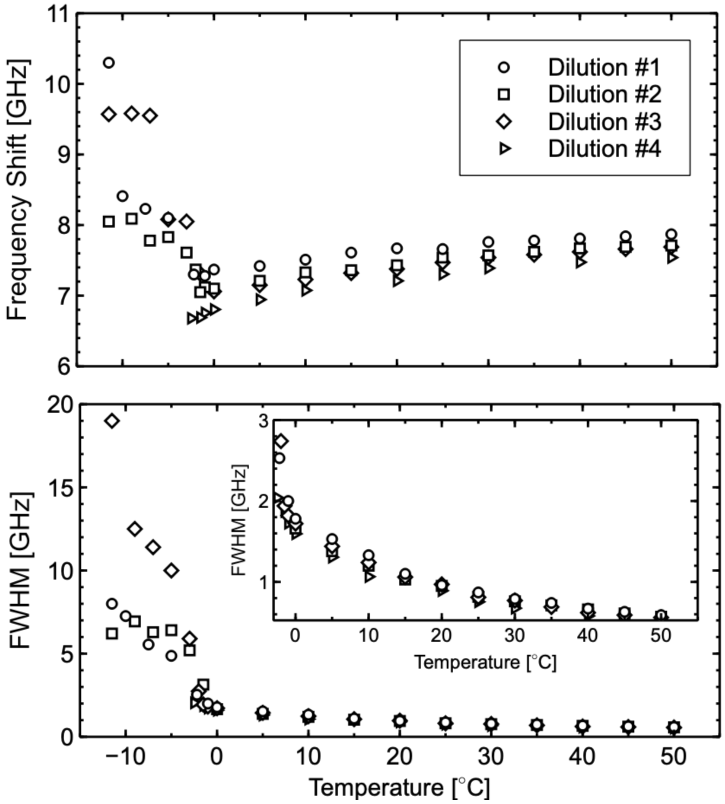

Figure 5.5: Plot of frequency shift, and FWHM of diluted snail mucus samples as a function of temperature.

temperature region T ≥ 0 °C. In this temperature region, the FWHM for all dilutions shows slight variations between one another which become more apparent towards T = 0 °C, and values are practically identical near T = 50.0 °C. In general, the FWHM decreases with increasing dilutions, this is best illustrated by the series of values at T = 5.0°C. This is consistent with the observation in the frequency shift data, that is as the dilution increases, the FWHM approaches values close to ultra pure water. Previous Brillouin scattering studies on aqueous polymer solutions had shown that polymer concentration has a significant influence on the FWHM [1, 32, 33]. In fact, Ref. [1] had stated that the polymer concentration has the largest influence on the Brillouin linewidth. Although the concentrations for these dilutions experiments are similar, there is a noticeable change in the FWHM between each dilution.

Following from the Brillouin frequency shift and linewidth, values of hypersound velocity, viscosity and sound absorption can be directly calculated using the raw spectral signatures obtained from Brillouin spectra.

5.4.3 Results: Viscoelastic Behaviour

Sound Velocity

Figure 5.6 shows the sound velocity for diluted mucus as a function of temperature and was calculated using Eq. 5.5. Examining the hypersound velocity obtained by Brillouin scattering can provide valuable insights into the viscoelastic properties within the diluted snail mucus samples. In general, the sound velocity exhibits interesting variations with temperature across the dilutions. At temperatures above the freezing point of each dilution, there is a gradual increase in hypersound velocity as the temperature increases. This behavior suggests a typical thermal expansion, where the molecules within the mucus exhibit increased vibrational energy and contribute to the propagation of sound waves at higher velocities. However, below their respective freezing points, dilutions 1-3 illustrate a pronounced increase in sound velocity with decreasing temperature. This notable change implies a structural transformation in the snail mucus network, likely induced by addition of ice in mucus. The transition occurring in these dilutions affects the arrangement and interaction of glycoproteins and water molecules, leading to an alteration in the sound velocity. In comparison to the other dilutions, dilution #4 demonstrates a distinct variation in sound velocity at temperatures below its freezing point where the velocity decreases with decreasing temperature. This finding implies that a phase transition is observed in Dilution #4 which indicates a break in the cross-linking network between glycoproteins and water molecules in snail mucus.

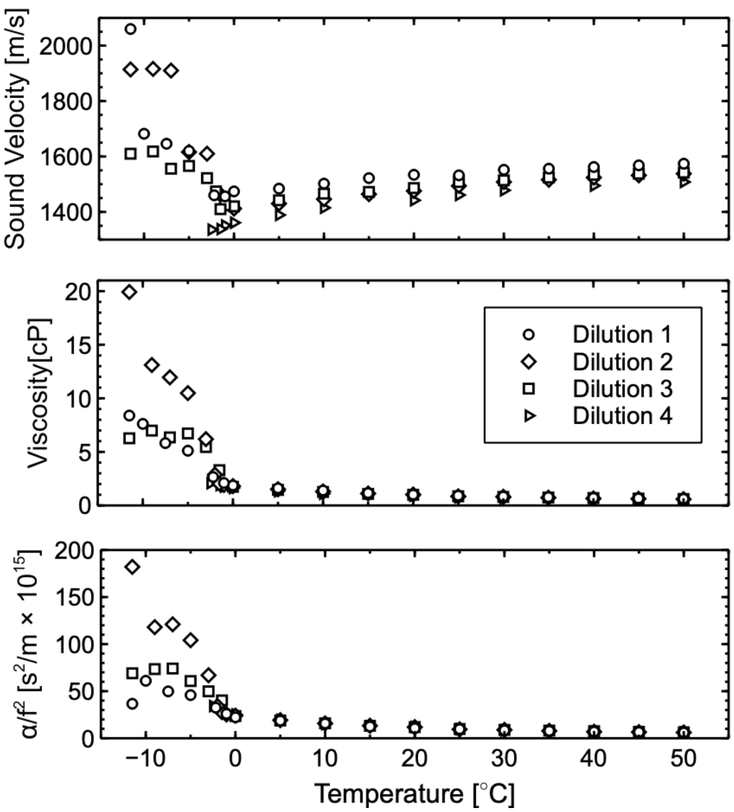

Figure 5.6: Hypersound velocity, apparent viscosity, and sound absorption for diluted mucus as a function of temperature.

Apparent Viscosity

Figure 5.6 shows the apparent viscosity for the diluted mucus sample as a function of temperature. In general, for T ≥ 0°C the apparent viscosity decreases with increasing temperature for all dilutions. Although it is hard to tell from Fig. 5.6, there is a systematic decrease in viscosity with increasing dilution. Below T = 0°C, the apparent viscosity does not show any consistent behaviour with dilution, likely due to the presence of ice crystallites in this region.

Fig. 5.7 shows the natural logarithm of the apparent viscosity of diluted snail mucus as a function of temperature calculated directly from Eq. 5.2 using the density (see Table 5.1) and FWHM. The viscosity decreases with increasing temperature in a

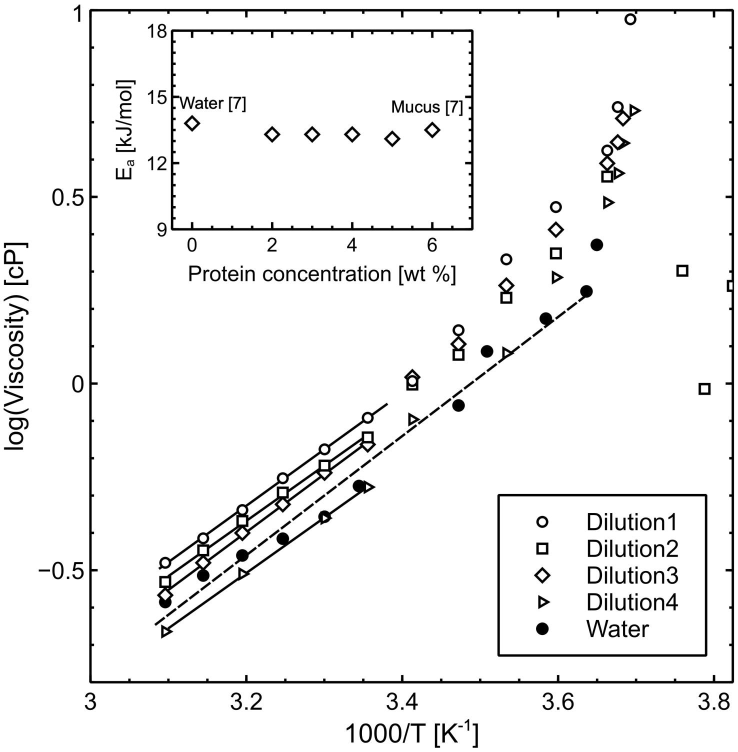

Figure 5.7: Natural logarithm of apparent viscosity of diluted snail mucus samples versus temperature. Solid lines: Best fits of Eq. 7.8 to high temperature data. Inset: Activation energy E_a obtained from the linear fits as a function of protein concentration.

similar manner to what has been previously reported for snail mucus along with other polymer-water systems [34–37].

In the high temperature region (25°C ≤ T ≤ 50°C), $\ln(\eta)$ depends linearly on $1/T$ so we fit an Arrhenius relationship of the form

$$\eta = \eta_0 e^{E_a/k_B T} \tag{5.8}$$

to this data and extracted the activation (enthalpy) energy E_a. Here, η_0 is a prefactor that contains the entropic contribution to the viscosity and k_B is the Boltzmann constant [4]. The resulting values for the activation energy E_a of all diluted mucus have values of ~ 13.3 ± 0.3 kJ/mol (see Table 6.2). Considering the data shown in Fig 5.7, dilutions 1 - 3 all exhibit similar values of the natural logarithm of apparent viscosity as the temperature decreases. However, the values for dilution 4 are approximately 2% smaller than the other dilutions and is very similar to the values of water previously reported [7]. This observed deviation we see in the natural logarithm of apparent viscosity between dilutions 3 and 4 is an indication of a structural change occurring in the mucus at the low protein concentration.

Because the activation energy E_a is consistent across all dilutions, as well as prior findings for snail mucus, the change in apparent viscosity was attributed to the pre-entropic component η_0 [7]. However, that study did not investigate the influence of protein concentration on the apparent viscosity or the activation energy. The concentration dependence of activation energy for polymer-water solutions previously studied displayed similar findings to those previously reported [2–4, 12]. That is, as concentration increases, the apparent viscosity increases, but E_a stays the same for the high temperature region ($T \geq 20^{\circ}C$). The results shown here further suggest that there is a slowing down of water dynamics near the protein as opposed to a strengthening in the H bonds present, and this is attributed to a decrease in configurational entropy. Otherwise, we should see an increase in the slope of Fig. 5.7. This entropy, as mentioned previously, is included in the pre-factor η_0. This result is consistent with previous studies that conduct similar Brillouin studies where the activation energy was determined for a number of different concentrations of diluted water–tert-butyl alcohol solutions [4]. Like the work presented in this manuscript, Ref. [4] also showed that the activation energy E_a for all dilutions had the same value.

The intermediate temperature region ($-2.5^{\circ}C \leq T \leq 25^{\circ}C$) displays a non-Arrhenius behaviour as is apparent in Fig. 5.7. Previously it was stated that the reasoning

Table 5.2: Best-fit parameters for fit of function $\ln(\eta) = \ln\eta_0 + E_a/k_BT$ to experimentally determined apparent viscosity.

Temperature Range	Dilution #	$\ln\eta_0$ (cP)	E_a kJ/mol	R^2
25.0°C ≤ T ≤ 52.0°C	1	-5.2	13.1 ± 0.2	0.992
	2	-5.4	13.3 ± 0.3	0.993
	3	-5.1	13.3 ± 0.3	0.994
	4	-5.2	13.3 ± 0.2	0.989

behind this could be due to the onset of cooperative motions at molecular level associated with a power law, or a Vogel–Fulcher-Taumann global dependence of viscosity [4]. Previous results obtained for snail mucus suggested that a factor that could be influencing the behaviour seen here could be attributed to the difference in density fluctuation relaxation times and structural relaxation times [2, 4].

Additionally, in the region below the freezing point, we can only say that the likely rapid increase in E_a is due the coexistence of ice and mucus, which has previously been reported [7].

Hypersound Absorption

Figure 5.6 presents the frequency-independent hypersound absorption coefficient, obtained through Eq. 5.6 as a function of temperature for diluted mucus. At temperatures above $T = 0$ °C, the absorption coefficient generally decreases with increasing temperature. Conversely, as the temperature decreases, the absorption coefficient tends to increase. However, it is important to note that the situation becomes more complex below $T = 0$ °C due to the presence of ice crystallites in the system. The presence of these crystallites introduces scattering effects that are not accounted for in the sound absorption formula. The observed decrease in sound absorption with

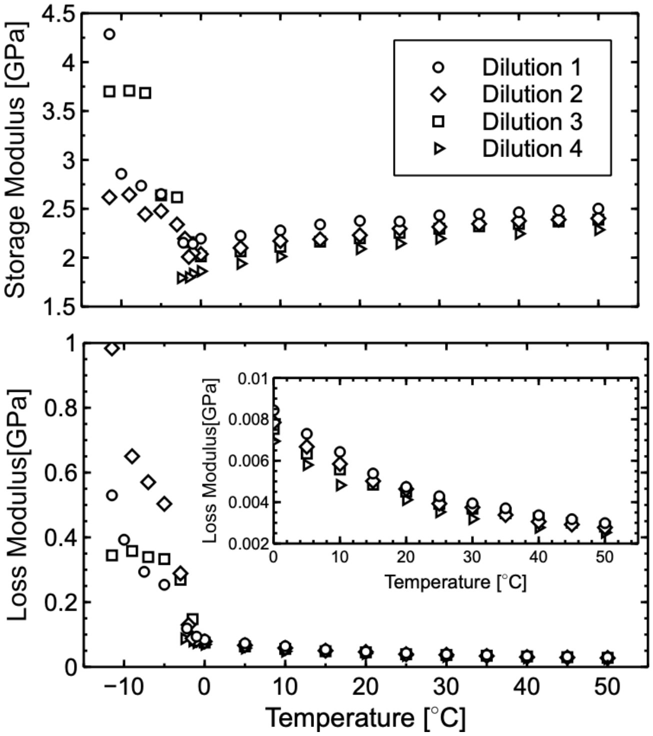

Figure 5.8: Storage and loss modulus as a function of temperature for all dilutions.

increasing temperature provides valuable insights into the dynamic behavior of the glycoprotein-water structure. It suggests that temperature has an influence on the acoustic properties of the system, indicating there are structural changes occurring in the system, although these changes are likely to be minimal over the dilution range studied. Other factors, such as the composition and concentration of glycoproteins, or the presence of other impurities such as bacterium, may have a stronger influence of the sound absorption.

Storage & Loss Modulus

Figure 5.8 shows the storage modulus calculated using the first term in Eq. 5.2 for all dilutions as a function of temperature. In general, for $T \geq 0$ °C the storage modulus shows a gradual increase in value for all dilutions with increasing temperature. Below

$T = 0$ °C, the storage modulus for dilutions 1-3 behave similarly, all showing a rapid increase with decreasing creasing temperature. However, the storage modulus for dilution 4 begins to decrease with decreasing temperature, similar to the behaviour previously observed for water [7].

Figure 5.8 also shows the loss modulus calculated used the second term in in Eq. 5.2 for all dilutions as a function of temperature. The loss modulus exhibits a general decrease in value for $T \geq 0$ °C for all dilutions. Furthermore, the loss modulus for dilutions 1-3 all increase with decreasing temperatures for $T \leq 0$ °C. The lpss modulus for Dilution 4 also increases with decreasing temperature, but we have limited data for this dilution below 0 °C because the liquid mucus Brillouin peaks became very weak.

Freezing Point Depression

Figure 5.9 illustrates the relationship between protein concentration (wt %) and freezing point depression. The observed behavior aligns with the Langmuir adsorption model, previously used to explain the adsorption of antifreeze glycoproteins onto ice crystal surfaces [38]. This model can be described by the following expression,

$$\Delta T = \frac{\Delta T_m K c}{1 + K c} \tag{5.9}$$

where, ΔT represents the freezing point depression, ΔT_m is the maximum freezing point depression, K is a measure of the strength of interaction between glycoprotein and ice, and c represents the concentration. Although the Langmuir model is typically used to describe the adsorption of molecules onto solid surfaces, we find it suitable for our system due to its ability to characterize and consider solute-solvent interactions. Consequently, we fit Equation 5.9 to our freezing point depression data, and the

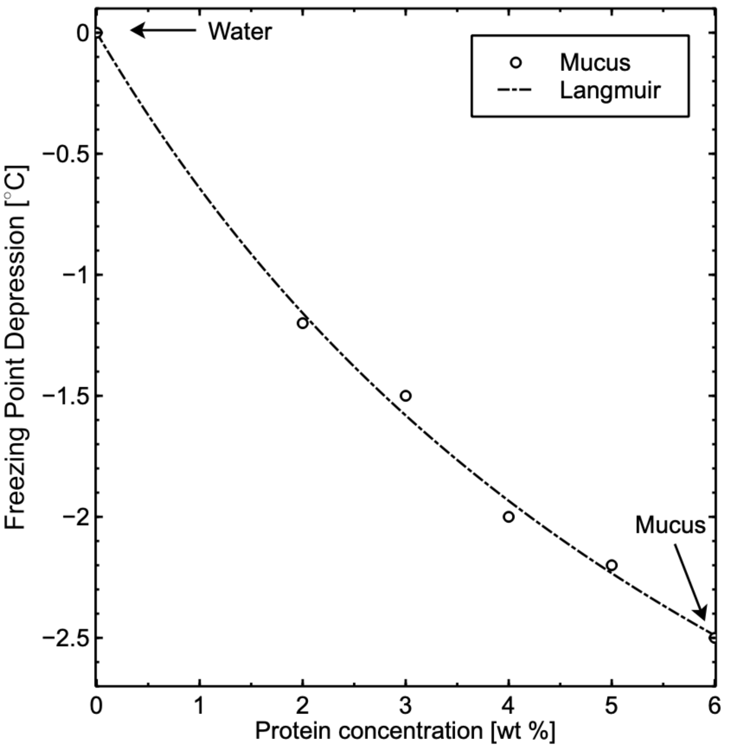

Figure 5.9: Plot of freezing point depression as a function of protein concentration. Dashed curve: Best fit of Eq. 5.9 to the experimental data.

resulting fit is displayed in Figure 5.9. The fitting yields $\Delta T_m = -5.85^{\circ}$C and $K = 0.123$ (wt$\%^{-1}$).

The trend that we see here in the freezing point depression is similar to previously studied sugar and water solutions and also similar to previous antifreeze glycoprotein studies [13, 39]. Although the relationship between the freezing point shown here for snail mucus and the sugar solutions are similar, the concentrations required for sugars to deplete ice growth were much higher sugar concentrations (wt %) to depress the freezing point by a similar amount to that of snail mucus. In fact, it took nearly five times as much sugar as it did glycoproteins to depress the freezing point to a value equal to that in snail mucus [39]. The freezing point depression, previously reported for antifreeze glycoproteins showed an overall increase as the concentration increased. As well, the magnitude of the increase was much higher for lower concentration solutions similar to the snail mucus. This is an indication that these glycoprotein systems influence the system in a similar way.

5.5 Dehydration Experiments

5.5.1 Sample Preparation

The dehydrated mucus was prepared by initially adding ~ 2 ml of natural snail mucus to a clear cuvette. The snail mucus was left unsealed at one end and allowed to dehydrate while room temperature Brillouin spectra were collected. Subsequently, before each Brillouin spectrum were collected, ATR-FTIR spectra were obtained for the dehydrated state to monitor the concentration. Temperature dependent Brillouin spectroscopy could not be completed due to the current limitations with the temperature-controlled sample chamber.

5.5.2 Results: Raw Spectral Signatures

Figure 5.10 shows room temperature Brillouin spectra collected on natural snail mucus as a function of time. Although this series of spectra was collected as a function of time, it is inherently a function of protein concentration as determined by the FTIR data (see Fig 5.2). Only a single peak was found in all spectra collected for the dehydrating mucus. For the purpose of this manuscript this will not be examined here.

Figure 5.11(top) shows the frequency shift for the dehydrated mucus as a function of time (concentration). As can be seen from this plot, there are two points where there is a dramatic change in the frequency shift. The first occurs at ~ 75 hours.

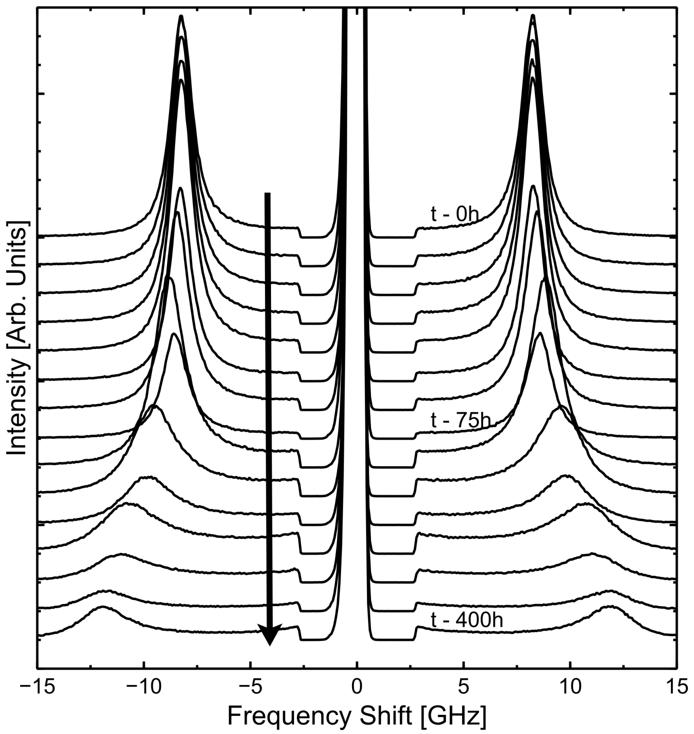

Figure 5.10: Room temperature Brillouin spectra collected on natural snail mucus dehydrating as a function of time. Arrow indicates direction of increasing time.

Before this point, there is an increase in frequency shift from 8.1 to 8.5 GHz, or at a rate of ~ 0.004 GHz/h. After this first point, there is a sudden increase in the frequency shift at a rate of ~ 0.02 GHz/h up to a shift of ~ 12 GHz at 300 hours, as indicated by the dashed line in Fig. 5.11. The second point occurs at a shift of 12 GHz where the frequency then remains constant. The general increase in frequency shift with increasing polymer concentration (time) is expected and consistent with previous Brillouin scattering studies on aqueous polymer solutions [1, 40–42].

Figure 5.11(bottom) shows the FWHM as a function of time for dehydrated mucus. Like the frequency shift data, there exists two points where there is a sudden change in the FWHM of the dehydrated mucus. The first point also occurs at ~ 75 hours, the same as the frequency shift. Above this point, like the frequency shift, there is a linear increase up to the the first transition point. Below the transition, the FWHM

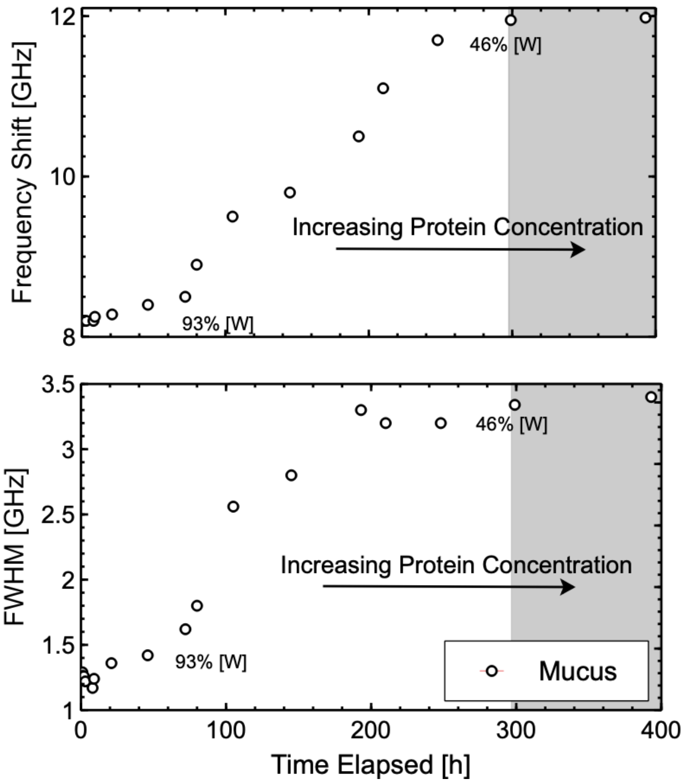

Figure 5.11: Plot of frequency shift and storage (top plot) modulus, and FWHM and apparent viscosity (bottom plot) as a function of time for the dehydrated mucus sample. Shaded region indicates the transition from a high to low hydrated state.

increases rapidly. However unlike the frequency shift result, the second transition point occurs at about 200 hours. The FWHM has been previously shown to be heavily influenced by polymer concentration [1, 33]. This polymer influence has been proposed previously by other Brillouin studies since the mobility of water molecules is restricted in the presence of the polymer hydration shell [2, 4].

It has been shown previously in similar Brillouin scattering studies on polymer-water systems that as the concentration in these systems increases, there is a transition from a high-hydration (liquid-like) to a gel like state that occurs [1, 42]. The shaded region indicated in Fig. 5.11 illustrates the point and region at which we believe this system transitions from a high hydration to a low hydration state. This transition will be further investigated in Section 5.6.

5.5.3 Results: Viscoelastic Behaviour

Sound Velocity

Figure 5.12(top) shows the sound velocity as a function of time for the dehydrated mucus. Just like the frequency shift and FWHM results displayed in Fig. 5.11, there exists two transition points where the behaviour of sound velocity changes. The first is at 75 hours, where before this transition point, there is a slight linear increase from ~ 1600m/s to 1700 m/s. After the transition the sound velocity displays a sharp linear increase in value from 1700 m/s to 2400 m/s where the second transition occurs. After the second transition at 300 hours the sound velocity plateaus and maintains a constant velocity of ~ 2400 m/s. This result is an indication that as the mucus dehydrates the structure of this system is becoming more rigid and “gel-like”. If this were not the case, then one would expect the sound velocity to increase only slightly since for liquids, especially those with high water content have sound velocities comparable to that of water [2, 4, 7].

Apparent Viscosity

Figure 5.12(middle) shows the apparent viscosity for dehydrated snail mucus calculated using Eq. 5.4. The apparent viscosity data exhibits two distinct transition points at approximately 75 and 200 hours. Above the first transition, there is a gradual linear increase in apparent viscosity. Subsequently, the apparent viscosity continues to rise linearly until reaching a value of approximately 3.5 cP at the second transition point. Beyond this second transition, the apparent viscosity remains relatively constant.

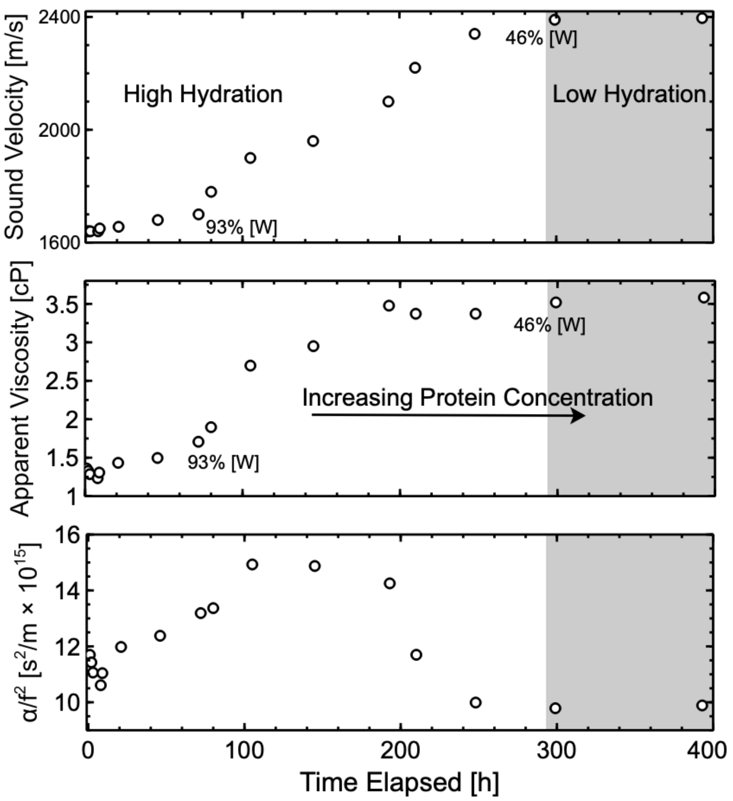

Figure 5.12: Sound velocity, apparent viscosity and sound absorption as a function of time for the dehydrated mucus sample. Shaded region shows the transition from a high to low hydrated state.

This data indicates that as the elapsed time increases, the viscosity generally increases. Furthermore, the apparent viscosity shows above and below the first transition point is different indicating the occurrence of a structural transition. These changes in apparent viscosity provide clear evidence of modifications in the structure of the glycoprotein-water network. The increase in viscosity might be associated with factors such as enhanced intermolecular interactions or strengthening of the cross-linked glycoprotein-water network.

Additionally, the fact that the viscosity remains constant after the second transition point suggests that the structure has reached a relatively stable state.

Hypersound Absorption

Figure 5.12(bottom) shows the hypersound absorption coefficient for dehydrated mucus calculated using Eq. 5.6. The observed behavior of the hypersound absorption coefficient for dehydrated mucus is unlike the sound velocity and viscosity data shown in this section the hypersound absorption shows an unusual behaviour. Initially, there is a gradual increase in the damping of sound waves, reaching a maximum absorption point at approximately 100 hours. Following this, there is a gradual decrease leading to a minimum hypersound absorption at around 250 hours, which then remains constant. This unusual behavior of the hypersound absorption highlights the complex nature of mucus dehydration and its impact on sound wave propagation properties.

This result is rather intriguing and shows that as the system transitions to a gel-like state the sound absorption by the glycoprotein-water network decreases. One possible reason that may account for the sound absorption behaviour is the increased structure associated with the gel state. In a liquid state, the molecules are relatively more mobile and can easily vibrate in response to sound waves. This molecular motion leads to effective sound energy dissipation and absorption. However, as the system transitions to a gel-like state, the increased molecular interactions and structural rigidity can restrict the movement of molecules. This restricted mobility reduces the ability of the gel state to effectively absorb sound energy.

Storage & Loss Modulus

Figure 5.13 shows the storage modulus as a function of time calculated using the first term in Eq. 5.2. The storage modulus shows two transition points just like the other quantities detailed in this work occurring at 75 and 300 hours. Before the first transition, the storage modulus increases linearly from ~ 2.9 GPa at 0 hours to about

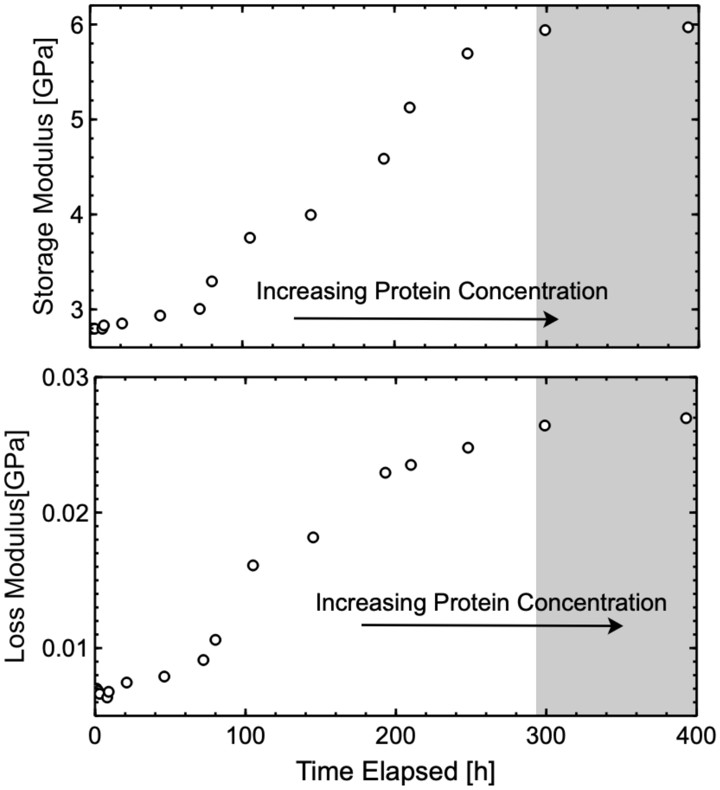

Figure 5.13: Storage and Loss modulus of dehydrating snail mucus as a function of time.

3.0 GPa at 75 hours. After the first transition, the storage modulus increases rapidly, up to about 6 GPa where it approaches the second transition. After the second transition, the storage modulus remains constant for the entirety of this experiment. The storage modulus as we know, is a measure of how much energy is stored elastically in the system. From this, Fig. 5.13 tells us that as the protein concentration increases, there is a general increase in the energy stored elastically in the mucus, where it eventually reaches a maximum value of 6 GPa at 300 hours.

Similarly, Fig. 5.13 also shows the loss modulus calculated using the second term in Eqn. 5.2 as a function of temperature. Like the storage modulus, the loss moduli shows a very similar behaviour. That is, there are two transitions present, both also at 75 hours and 300 hours. Before the first transition, there is a linear increase from

0.005 to 0.01 GPa in the loss modulus. After the first transition, there is non-linear increase up to a value of 0.03 GPa at 300 hours. Below the second transition (at 300 hours) the loss modulus appears to slightly increase. The loss modulus is a measure of how much energy is lost through heat in a system: the data presented here shows is that as the protein concentration increases, the amount of energy lost through heat also increases.

5.6 General Discussion

5.6.1 Structural Transition: Influence of Glycoproteins

This study on natural snail mucus has revealed the presence of at least three structural transitions, each characterized by a discontinuous change observed in both raw Brillouin scattering data and calculated viscoelastic properties. These transitions mark significant shifts in the physical properties of the mucus, indicating changes in the molecular arrangement, intermolecular forces or conformational dynamics in the glycoprotein-water network.

Figure 5.14 shows the frequency shift and FWHM obtained from room temperature Brillouin spectroscopy of both diluted and dehydrated snail mucus, plotted as a function of protein concentration obtained from ATR-FTIR data previously reported in this manuscript. As mentioned above, we observe three distinct transitions in the raw spectral data, along with calculated quantities throughout this manuscript. The first transition occurs at approximately 3% protein concentration. Both the frequency shift and FWHM show a sharp increase in value at this point. Despite only having one data point for diluted mucus (dilution 4) above this point, the frequency shift and FWHM are significantly different than for dilutions 1 - 3. Additionally, if we consider

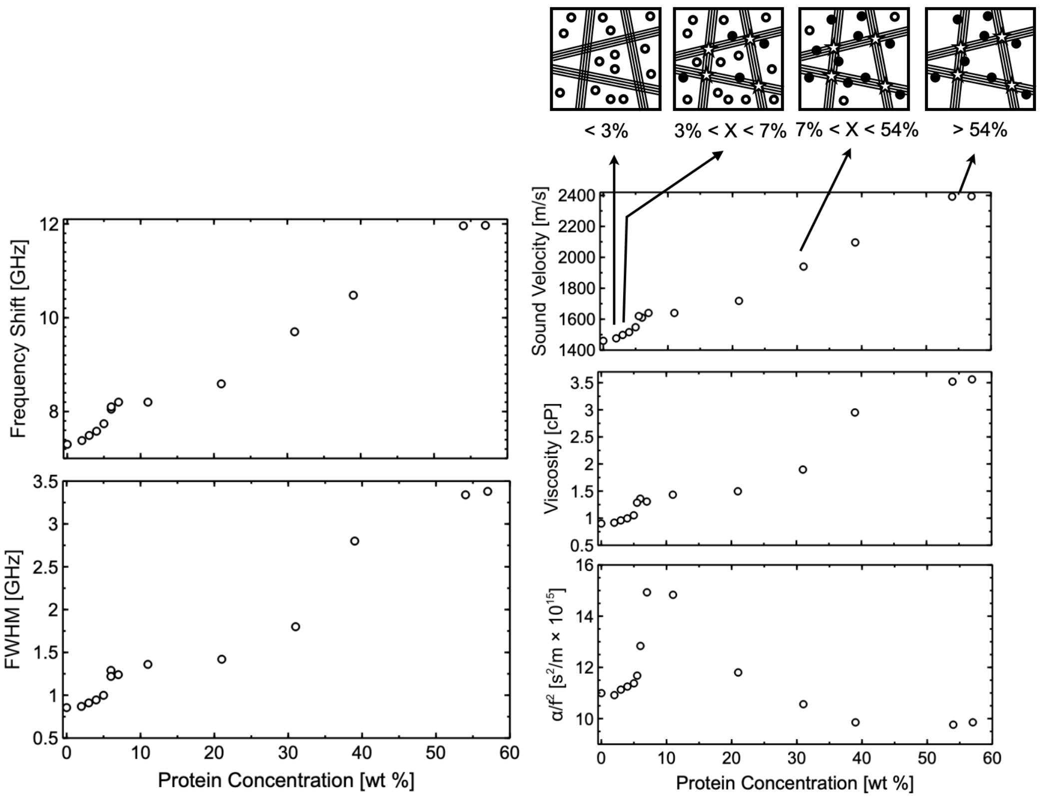

Figure 5.14: Plots of room-temperature Brillouin peak frequency shift and FWHM (left panel) and derived viscoelastic properties (right panel) as a function of protein concentration in snail mucus solutions. Additionally, a simple schematic is provided to illustrate the observed structural transitions. These transitions, along with the concentration at which they occur is depicted in the right panel. The symbols in this figure correspond to ○ - free water, ● - bound water, ☆ - cross-links and lines represent glycoproteins.

the temperature dependence of frequency shift and FWHM shown previously (see Fig 5.11) we can see that data for dilution 4 resemble that of pure water obtained previously by Brillouin spectroscopy [7]. The dilution data presented throughout this work suggest that this first transition is likely attributed to the proteins becoming first cross-linked in the system. Further support for this is through the calculated viscoelastic properties, speed of sound, apparent viscosity and sound absorption as shown in the right panel of Fig. 5.14. Furthermore, the temperature dependence of the viscoelastic properties for each dilution previously shown (see Figures 5.6 - 5.8) all increase in value as the protein concentration increases, a particularly strong increase is observed between 2 and 3% protein concentration. Perhaps, the most obvious increase in the viscoelasticity is observed in Fig. 5.7, where there is a clear difference between the natural logarithm of apparent viscosity for dilution 3 and 4. Recall, that this change was associated with the entropic pre-factor η_0, which is subject to conformational changes [2, 4]. It has been stated before that cross-linked protein-water systems increase the elastic and acoustic properties of the system [1, 5–7] which would also support our idea proposed here.

The second transition we observe occurs at a protein concentration of approximately 7% and has been attributed to the depletion of any free water in the snail mucus. Bound and free water exist in polymer gel networks naturally and together make up the entire water content in such systems [43–45]. Bound water refers to the water molecules that are tightly associated or “bound” to the protein-water network, while free water, on the other hand, represents the water that is not bound to the network and is “free” to move in the system. The greater amount of bound water in a system can increase the cross-linking density which in turn causes the molecular structure to be more rigid [45]. The observed behavior in both the raw Brillouin data and calculated viscoelastic quantities supports the notion that this transition is caused by the initial depletion of free water in the mucus. First considering, Fig. 5.14, we can see a general increase in both the frequency shift and FWHM as the protein concentration increases after a protein concentration of 7% up to ~ 50%. The increase in both frequency shift and FWHM with protein concentration in this region is a clear indication of increased rigidity. Additionally, the viscoelastic properties presented in Fig. 5.14 show an increase in the sound velocity and viscosity with increasing concentration, while α/f^2 decreases with increasing concentration. The increase in both sound velocity and viscosity observed in this region signifies a significant shift in the molecular structure, indicating a transition towards increased rigidity. The rise in sound velocity, is a measure of how quickly sound propagates through a medium, highlighting the increased stiffness of the glycoprotein-water network. Simultaneously, the increased apparent viscosity, a measure of a fluid's resistance to flow, further supports this transition by indicating a greater resistance to molecular rearrangements. Moreover, the decrease in the sound absorption in this region provides more justification for this claim. In pure liquids, molecules have higher mobility, allowing them to vibrate and dissipate sound energy effectively. The random arrangement of molecules in a liquid state provides more opportunities for sound waves to interact with the medium and be absorbed. Thus, as the protein concentration in the system increases, and the internal molecular structure becomes more rigid, then the molecular mobility will be restricted leading to a lower sound absorption.

Lastly, the third transition observed in this work occurs at a protein concentration of 54% and has been deemed due to the transition to a gel state and it is suggested that some of the remaining bound water be evaporated at this state. As illustrated by the raw spectral data in Fig. 5.14, there is a clear and distinct transition occurring at a protein concentration of 54%, where both the frequency shift and FWHM go from increasing to a constant value. Due to the relatively high frequency shift and FWHM in this region, along with the fact that there is still a considerable amount of water left in the system, as determined by the ATR data, this transition was therefore attributed to a gel-like state. Further support for this is based on the calculated viscoelastic properties shown in Fig. 5.14. The sound velocity, viscosity and sound absorption all show their respective values remain constant for this high protein concentration region. One would expect that for a gel state, the structure would be more rigid mainly for two reasons. Firstly, a decrease in the overall water content typically results in increased rigidity of the gel-like structure. Secondly, the reduction in free water, with only bound water being incorporated into the glycoprotein network, can contribute to an increase in structural rearrangement and therefore greater rigidity. In the gel state, as the free water content decreases, the molecular interactions among glycoproteins and bound water become more pronounced. This increased interaction contributes to a more structured and rigid gel network. Moreover, the presence of bound water molecules in the gel network restricts the movement of proteins and other components. Previous Brillouin scattering studies on gelatin gels as a function of protein concentration show behaviour similar to that what is shown here [1]. For example, in that Brillouin study, there is a plateau at high concentration values, like that shown here. Likewise, the FWHM shows a brief plateau at concentrations near 50% protein, similar to our results.

5.7 Conclusion

Brillouin light scattering spectroscopy was employed to investigate the viscoelastic properties and phase behavior of diluted and dehydrated snail mucus. The temperature range of -11°C $\leq T \leq$ 52 °C was explored for all dilutions of the snail mucus, while the dehydrated mucus was examined with respect to time and corresponding protein concentration. Intriguingly, deviations in both temperature and concentration dependencies of spectral peak parameters and derived viscoelastic properties validate the previously identified liquid-to-solid phase transition at -2.5°C, while additionally revealing a correlation between concentration and this transition temperature T_{pt}. Collectively, both the dilution and dehydration data suggest three distinct structural transitions occurring at protein concentrations of 3%, 7% and 54%. These transitions were attributed to the initiation of cross-linking in the glycoprotein water network, depletion of free water, and the transition to a gel state. These results support previous Brillouin studies on gels and provide further evidence of the intricate role of glycoproteins within these systems [1]. Notably, this research offers fresh insights into the significance of hydration water in protein-water systems of biological relevance. Furthermore, it underscores the effectiveness of Brillouin spectroscopy in studying this unique class of natural materials, expanding the range of systems to which this technique has proven to be highly valuable.

5.8 Supplementary Material for: Influence of Hydration and Dehydration on the Viscoelastic Properties of Snail Mucus by Brillouin Spectroscopy

Table 5.3: Raw data obtained from ATR spectra collected on diluted and dehydrated mucus. ν_{1-3} is the spectral peak position, Γ_{1-3} is the full width at half maximum (FWHM) for each correspond vibrational mode, and I_{1-3} is the integrated intensity for each vibrational mode.

[W]	ν_1 [cm^{-1}]	ν_2 [cm^{-1}]	ν_3 [cm^{-1}]	Γ_1 [cm^{-1}]	Γ_2 [cm^{-1}]	Γ_3 [cm^{-1}]	I_1 [a.u]	I_2 [a.u]	I_3 [a.u]
45%W	3340 ± 30	1610 ± 10	N.V	350 ± 10	50 ± 10	N.V	220 ± 20	15 ± 5	N.V
46%W	3340 ± 30	1620 ± 10	N.V	350 ± 10	50 ± 10	N.V	220 ± 20	15 ± 5	N.V
61%W	3330 ± 20	1620 ± 10	N.V	380 ± 10	70 ± 10	N.V	310 ± 20	20 ± 5	N.V
69%W	3330 ± 30	1620 ± 10	N.V	390 ± 10	70 ± 10	N.V	320 ± 20	20 ± 5	N.V
79%W	3330 ± 30	1620 ± 10	2120 ± 40	400 ± 10	100 ± 10	420 ± 50	470 ± 20	30 ± 5	20 ± 5
93%W	3330 ± 10	1630 ± 10	2130 ± 50	410 ± 10	100 ± 10	400 ± 50	490 ± 20	35 ± 5	20 ± 5
Mucus	3330 ± 10	1630 ± 10	2140 ± 50	410 ± 10	100 ± 10	350 ± 20	500 ± 20	40 ± 5	19 ± 5
95%W	3320 ± 10	1630 ± 20	2140 ± 40	410 ± 10	100 ± 10	360 ± 20	510 ± 20	30 ± 5	17 ± 5
96%W	3320 ± 20	1640 ± 20	2130 ± 50	410 ± 10	100 ± 10	360 ± 20	510 ± 20	30 ± 5	19 ± 5
97%W	3320 ± 20	1640 ± 20	2130 ± 50	410 ± 10	100 ± 10	360 ± 20	510 ± 20	25 ± 5	18 ± 5
98%W	3310 ± 20	1650 ± 20	2130 ± 40	410 ± 10	100 ± 10	360 ± 20	510 ± 20	25 ± 5	18 ± 5
100%W	3310 ± 20	1650 ± 20	2130 ± 40	410 ± 10	100 ± 10	360 ± 20	530 ± 20	20 ± 5	18 ± 5

Table 5.4: Brillouin peak frequency shift (f_B) and full width at half-maximum (Δf_B) for Dilution #1 at the indicated temperatures.

Temperature (K)	Temperature (˚C)	f_B (GHz)	Δf_B (GHz)
323.0 ± 0.5	50.0 ± 0.5	7.9 ± 0.3	0.6 ± 0.3
318.0 ± 0.5	45.0 ± 0.5	7.8 ± 0.3	0.6 ± 0.3
313.0 ± 0.5	40.0 ± 0.5	7.8 ± 0.3	0.7 ± 0.3
308.0 ± 0.5	35.0 ± 0.5	7.8 ± 0.3	0.7 ± 0.3
303.0 ± 0.5	30.0 ± 0.5	7.8 ± 0.4	0.8 ± 0.3
298.0 ± 0.5	25.0 ± 0.5	7.7 ± 0.4	0.9 ± 0.3
293.0 ± 0.5	20.0 ± 0.5	7.7 ± 0.5	1.0 ± 0.3
288.0 ± 0.5	15.0 ± 0.5	7.6 ± 0.5	1.1 ± 0.5
283.0 ± 0.5	10.0 ± 0.5	7.5 ± 0.5	1.3 ± 0.5
278.0 ± 0.5	5.0 ± 0.5	7.4 ± 0.5	1.5 ± 0.7
273.0 ± 0.5	0.0 ± 0.5	7.4 ± 0.6	1.8 ± 0.7
272.0 ± 0.5	-1.0 ± 0.5	7.3 ± 0.6	2.0 ± 0.8
270.8 ± 0.5	-2.2 ± 0.5	7.3 ± 0.6	2.5 ± 0.9
268.0 ± 0.5	-5.0 ± 0.5	8.1 ± 0.7	4.9 ± 1.0
265.5 ± 0.5	-7.5 ± 0.5	8.2 ± 0.7	5.6 ± 1.1
263.0 ± 0.5	-10.0 ± 0.5	8.4 ± 0.9	7.3 ± 1.2
261.5 ± 0.5	-11.5 ± 0.5	10.3 ± 1.2	8.0 ± 1.4

Table 5.5: Brillouin peak frequency shift (f_B) and full width at half-maximum (Δf_B) for Dilution #2 at the indicated temperatures.

Temperature (K)	Temperature (°C)	f_B (GHz)	Δf_B (GHz)
323.0 ± 0.5	50.0 ± 0.5	7.7 ± 0.3	0.6 ± 0.3
318.0 ± 0.5	45.0 ± 0.5	7.7 ± 0.4	0.6 ± 0.3
313.0 ± 0.5	40.0 ± 0.5	7.7 ± 0.4	0.6 ± 0.3
308.0 ± 0.5	35.0 ± 0.5	7.6 ± 0.4	0.7 ± 0.3
303.0 ± 0.5	30.0 ± 0.5	7.6 ± 0.4	0.8 ± 0.3
298.0 ± 0.5	25.0 ± 0.5	7.5 ± 0.4	0.8 ± 0.5
293.0 ± 0.5	20.0 ± 0.5	7.4 ± 0.4	1.0 ± 0.5
288.0 ± 0.5	15.0 ± 0.5	7.4 ± 0.5	1.1 ± 0.7
283.0 ± 0.5	10.0 ± 0.5	7.3 ± 0.4	1.2 ± 0.7
278.0 ± 0.5	5.0 ± 0.5	7.2 ± 0.5	1.4 ± 0.8
273.0 ± 0.5	0.0 ± 0.5	7.1 ± 0.5	1.7 ± 0.8
272.0 ± 0.5	-1.0 ± 0.5	7.1 ± 0.5	1.8 ± 0.9
271.5 ± 0.5	-1.5 ± 0.5	7.1 ± 0.5	1.9 ± 0.9
271.0 ± 0.5	-2.0 ± 0.5	7.4 ± 0.5	2.7 ± 0.9
268.0 ± 0.5	-3.0 ± 0.5	7.6 ± 0.5	5.9 ± 0.9
266.0 ± 0.5	-5.0 ± 0.5	7.8 ± 0.5	10.0 ± 1.1
264.0 ± 0.5	-7.0 ± 0.5	7.8 ± 0.5	11.4 ± 1.3
262.0 ± 0.5	-9.0 ± 0.5	8.1 ± 0.5	12.5 ± 1.4
260.5 ± 0.5	-11.5 ± 0.5	8.1 ± 0.5	19.0 ± 2.0

Table 5.6: Brillouin peak frequency shift (f_B) and full width at half-maximum (Δf_B) for Dilution #3 at the indicated temperatures.

Temperature (K)	Temperature (˚C)	f_B (GHz)	Δf_B (GHz)
323.0 ± 0.5	50.0 ± 0.5	7.7 ± 0.3	0.57 ± 0.3
318.0 ± 0.5	45.0 ± 0.5	7.7 ± 0.3	0.6 ± 0.3
313.0 ± 0.5	40.0 ± 0.5	7.6 ± 0.4	0.7 ± 0.3
308.0 ± 0.5	35.0 ± 0.5	7.6 ± 0.4	0.7 ± 0.4
303.0 ± 0.5	30.0 ± 0.5	7.5 ± 0.4	0.8 ± 0.4
298.0 ± 0.5	25.0 ± 0.5	7.5 ± 0.5	0.8 ± 0.5
293.0 ± 0.5	20.0 ± 0.5	7.4 ± 0.5	1.0 ± 0.5
288.0 ± 0.5	15.0 ± 0.5	7.3 ± 0.6	1.0 ± 0.6
283.0 ± 0.5	10.0 ± 0.5	7.2 ± 0.6	1.2 ± 06
278.0 ± 0.5	5.0 ± 0.5	7.2 ± 0.7	1.4 ± 0.7
273.0 ± 0.5	0.0 ± 0.5	7.1 ± 0.7	1.7 ± 0.7
271.5 ± 0.5	-1.5 ± 0.5	7.3 ± 0.8	3.1 ± 1.0
270.0 ± 0.5	-3.0 ± 0.5	8.1 ± 0.8	5.2 ± 1.1
268.0 ± 0.5	-5.0 ± 0.5	8.1 ± 0.8	6.4 ± 1.2
266.0 ± 0.5	-7.0 ± 0.5	9.6 ± 0.9	1.3 ± 0.7
264.0 ± 0.5	-9.0 ± 0.5	9.6 ± 0.9	1.1 ± 0.7
261.5 ± 0.5	-11.5 ± 0.5	9.6 ± 0.9	1.2 ± 0.7

Table 5.7: Brillouin peak frequency shift (f_B) and full width at half-maximum (Δf_B) for Dilution #4 at the indicated temperatures.

Temperature (K)	Temperature (˚C)	f_B (GHz)	Δf_B (GHz)
323.0 ± 0.5	50.0 ± 0.5	7.5 ± 0.3	0.5 ± 0.3
313.0 ± 0.5	40.0 ± 0.5	7.5 ± 0.3	0.6 ± 0.3
303.0 ± 0.5	30.0 ± 0.5	7.4 ± 0.3	0.7 ± 0.4
298.0 ± 0.5	25.0 ± 0.5	7.3 ± 0.3	0.8 ± 0.4
293.0 ± 0.5	20.0 ± 0.5	7.2 ± 0.4	0.9 ± 0.4
283.0 ± 0.5	10.0 ± 0.5	7.1 ± 0.4	1.1 ± 0.5
278.0 ± 0.5	5.0 ± 0.5	6.9 ± 0.4	1.3 ± 0.5
273.0 ± 0.5	0.0 ± 0.5	6.8 ± 0.4	1.6 ± 0.6
271.5 ± 0.5	-1.0 ± 0.5	6.8 ± 0.4	1.7 ± 0.6
271.0 ± 0.5	-1.5 ± 0.5	6.7 ± 0.5	1.9 ± 0.7
269.5 ± 0.5	-2.5 ± 0.5	6.7 ± 0.5	2.0 ± 0.7

Table 5.8: Brillouin peak frequency shift and full width at half-maximum for dehydrated mucus at indicated elapsed time.

Time Elapsed Hours	Frequency Shift [GHz]	FWHM [GHz]
1	8.2 ± 0.3	1.3 ± 0.4
2	8.2 ± 0.3	1.3 ± 0.4
3	8.2 ± 0.3	1.2 ± 0.5
8	8.2 ± 0.3	1.2 ± 0.5
9	8.3 ± 0.4	1.2 ± 0.5
21	8.3 ± 0.4	1.4 ± 0.6
46	8.4 ± 0.4	1.4 ± 0.6
72	8.5 ± 0.4	1.6 ± 0.7
80	8.9 ± 0.5	1.8 ± 0.7
104	9.5 ± 0.5	2.6 ± 0.7
150	9.8 ± 0.5	2.8 ± 0.7
175	10.5 ± 0.6	3.3 ± 0.7
220	11.1 ± 0.6	3.2 ± 0.8
245	11.7 ± 0.7	3.2 ± 0.8
293	12.0 ± 0.9	3.3 ± 0.9
393	12.0 ± 0.9	3.4 ± 0.9

Bibliography

[1] M. Bailey, M. Alunni-Cardinali, N. Correa, S. Caponi, T. Holsgrove, H. Barr, N. Stone, C. P. Winlove, D. Fioretto, and F. Palombo. Brillouin-derived viscoelastic parameters of hydrogel tissue models. *arXiv preprint arXiv:1912.08292*, 2019.

[2] L Comez, L Lupi, M Paolantoni, F Picchiò, and D Fioretto. Hydration properties of small hydrophobic molecules by brillouin light scattering. *The Journal of Chemical Physics*, 137(11):114509, 2012.

[3] L Comez, M Paolantoni, P Sassi, S Corezzi, A Morresi, and D Fioretto. Molecular properties of aqueous solutions: a focus on the collective dynamics of hydration water. *Soft Matter*, 12(25):5501–5514, 2016.

[4] L Lupi, L Comez, C Masciovecchio, A Morresi, M Paolantoni, P Sassi, F Scarponi, and D Fioretto. Hydrophobic hydration of tert-butyl alcohol studied by brillouin light and inelastic ultraviolet scattering. *The Journal of chemical physics*, 134(5):02B603, 2011.

[5] M. Denny. The role of gastropod pedal mucus in locomotion. *Nature*, 285(5761):160–161, 1980.

[6] M. W. Denny. Mechanical properties of pedal mucus and their consequences for gastropod structure and performance. *Am. Zool.*, 24(1):23–36, 1984.

[7] Dillon Hanlon, Maynard J Clouter, and G Todd Andrews. Temperature dependence of the viscoelastic properties of a natural gastropod mucus by brillouin light scattering spectroscopy. *Soft Matter*, 2023.

[8] P. Verdugo, I. Deyrup-Olsen, M. Aitken, M. Villalon, and D. Johnson. Molecular mechanism of mucin secretion: I. the role of intragranular charge shielding. *J. Dent. Res.*, 66(2):506–508, 1987.

[9] J. Li, A. D. Celiz, J. Yang, Q Yang, I. Wamala, W. Whyte, B. R. Seo, N. V. Vasilyev, J. J. Vlassak, and Z. Suo. Tough adhesives for diverse wet surfaces. *Science*, 357(6349):378–381, 2017.

[10] V. Bouvet and R. N. Ben. Antifreeze glycoproteins: Structure, conformation, and biological applications. *Cell Biochem. Biophys.*, 39:133–144, 2003.

[11] C. S. Kwan, A. R. Cerullo, and A. B. Braunschweig. Design and synthesis of mucin-inspired glycopolymers. *ChemPlusChem*, 85:2704–2721, 2020.

[12] G. Monaco, D. Fioretto, L. Comez, and G. Ruocco. Glass transition and density fluctuations in the fragile glass former orthoterphenyl. *Physical Review E*, 63(6):061502, 2001.

[13] S. Ebbinghaus, K. Meister, B. Born, A. L. DeVries, M. Gruebele, and M/ Havenith. Antifreeze glycoprotein activity correlates with long-range protein-water dynamics. *Journal of the American Chemical Society*, 132(35):12210–12211, 2010.

[14] L. Comez, C. Masciovecchio, G. Monaco, and D. Fioretto. Progress in liquid and glass physics by brillouin scattering spectroscopy. In *Solid state physics*, volume 63, pages 1–77. Elsevier, 2012.

[15] CJ Montrose, VA Solovyev, and TA Litovitz. Brillouin scattering and relaxation in liquids. *The Journal of the Acoustical Society of America*, 43(1):117–130, 1968.

[16] NJ Tao, G Li, and HZ Cummins. Brillouin-scattering study of the liquid-glass transition in cakno 3: Mode-coupling analysis. *Physical Review B*, 45(2):686, 1992.

[17] E. Gugliando, M. Cordaro, R. Fusco, A. F. Peritore, R. Siracusa, T. Genovese, R. D'Amico, D. Impellizzeri, R. DiPaola, S. Cuzzocrea, and R. Crupi. Protective effect of snail secretion filtrate against ethanol-induced gastric ulcer in mice. *Sci. Rep.*, 11:3638, 2021.

[18] JG Dil. Brillouin scattering in condensed matter. *Rep. Prog. Phys.*, 45(3):285, 1982.

[19] J. Rouch, C. C. Lai, and S. H. Chen. Brillouin scattering studies of normal and supercooled water. *J. Chem. Phys.*, 65(10):4016–4021, 1976.

[20] G. T. Andrews. Acoustic characterization of porous silicon. In L. Canham, editor, *Handbook of Porous Silicon*, chapter 53, pages 691–703. Springer International, 2018.

[21] P. R Griffiths. Fourier transform infrared spectrometry. *Science*, 222(4621):297–302, 1983.

[22] R. Arunkumar, C. J. Drummond, and T. L. Greaves. Ftir spectroscopic study

of the secondary structure of globular proteins in aqueous protic ionic liquids. *Frontiers in Chemistry*, 7:74, 2019.

[23] SP Lewis, AT Lewis, and PD Lewis. Prediction of glycoprotein secondary structure using atr-ftir. *Vibrational Spectroscopy*, 69:21–29, 2013.

[24] I Spiridon, C. A. Teaca, and R. Bodirlau. Structural changes evidenced by ftir spectroscopy in cellulosic materials after pre-treatment with ionic liquid and enzymatic hydrolysis. *BioResources*, 6(1):400–413, 2011.

[25] J. Grdadolnik. Atr-ftir spectroscopy: Its advantage and limitations. *Acta Chimica Slovenica*, 49(3):631–642, 2002.

[26] S. Yu Venyaminov and F. G Prendergast. Water (h2o and d2o) molar absorptivity in the 1000–4000 cm- 1range and quantitative infrared spectroscopy of aqueous solutions. *Analytical biochemistry*, 248(2):234–245, 1997.

[27] P. Larkin. *Infrared and Raman spectroscopy: principles and spectral interpretation*. Elsevier, 2017.

[28] Michael Bradley. Curve fitting in raman and ir spectroscopy: basic theory of line shapes and applications. *Thermo Fisher Scientific, Madison, USA, Application Note*, 50733, 2007.

[29] C. L.. O'Connor and J. P Schlupf. Brillouin scattering in water: the landau—placzek ratio. *J. Chem. Phys.*, 47(1):31–38, 1967.

[30] P Zhao and JJ Vanderwal. Brillouin scattering study of gelatin gel. *Polymer Gels and Networks*, 5(1):23–36, 1997.

[31] Y Scheyer, C Levelut, J Pelous, JC Cook, M Johnson, F Prochazka, and D Durand. Relaxations versus crosslink density in glass-and gel-forming polyurethane. *Physica B: Condensed Matter*, 234:445–447, 1997.

[32] M Pochylski, F Aliotta, Z Blaszczak, and J Gapiński. Structuring effects and hydration phenomena in poly (ethylene glycol)/water mixtures investigated by brillouin scattering. *The Journal of Physical Chemistry B*, 110(41):20533–20539, 2006.

[33] A. I. Van Den Bulcke, B. Bogdanov, N. De Rooze, E. H. Schacht, M. Cornelissen, and H. Berghmans. Structural and rheological properties of methacrylamide modified gelatin hydrogels. *Biomacromolecules*, 1(1):31–38, 2000.

[34] J. H. So, R. Esquivel-Sirvent, S. S. Yun, and F. B. Stumpf. Ultrasonic absorption and velocity measurements for poly (vinyl alcohol) and water solutions. *J. Acoust. Soc. Am.*, 96(6):3807–3808, 1994.

[35] J. H. So, R. Esquivel-Sirvent, S. S. Yun, and F. B. Stumpf. Ultrasonic velocity and absorption measurements for poly(acrylic acid) and water solutions. *J. Acoust. Soc. Am.*, 98(1):659–660, 1995.

[36] R. Esquivel-Sirvent, B. Tan, I. Abdelraziq, S. S. Yun, and F. B. Stumpf. Absorption and velocity of ultrasound in binary solutions of poly (ethylene glycol) and water. *J. Acoust. Soc. Am.*, 93(2):819–820, 1993.

[37] R. Esquivel-Sirvent, S. S. Yun, and F. B. Stumpf. Absorption and velocity of ultrasound in binary solutions of poly (sodium 4-styrenesulfonate) and water. *J. Acoust. Soc. Am.*, 95(1):557–558, 1994.

[38] TS Burcham, DT Osuga, Y Yeh, and RE Feeney. A kinetic description of antifreeze glycoprotein activity. *Journal of Biological Chemistry*, 261(14):6390–6397, 1986.

[39] T. Uraji, H. Kohno, H. Yoshimura, M. Shimoyamada, and K. Watanabe. Freezing point depression of polyol-aqueous solutions in the high concentration range. *Food Science and Technology International, Tokyo*, 2(1):38–42, 1996.

[40] D Sl Bedborough and DA Jackson. Brillouin scattering study of gelatin gel using a double passed fabry-perot spectrometer. *Polymer*, 17(7):573–576, 1976.

[41] A Bot, RPC Schram, and GH Wegdam. Brillouin light scattering from a biopolymer gel: Hypersonic sound waves in gelatin. *Colloid and polymer science*, 273:252–256, 1995.

[42] F. Palombo and D. Fioretto. Brillouin light scattering: Applications in biomedical sciences. *J. Chem. Rev.*, 119:7833, 2019.

[43] N. A Peppas and E. W Merrill. Development of semicrystalline poly (vinyl alcohol) hydrogels for biomedical applications. *Journal of biomedical materials research*, 11(3):423–434, 1977.

[44] N. A Peppas and A. R Khare. Preparation, structure and diffusional behavior of hydrogels in controlled release. *Advanced drug delivery reviews*, 11(1-2):1–35, 1993.

[45] A. S Hoffman. Hydrogels for biomedical applications. *Advanced Drug Delivery Reviews*, 64:18–23, 2012.

Chapter 6

Probing the Viscoelastic Properties of Aqueous Protein Solutions using Molecular Dynamics Simulations

Reproduced with permission from D. F. Hanlon, I. Saika-Voivod, M. Shajahan G. Razul and G. T. Andrews.

Submitted to Journal of Chemical Physics on September 22, 2023

Co-Authorship Statement

We, the authors of this manuscript, have contributed collectively to the research, writing, and preparation of this work. Each author's contribution is outlined below:

D. F. Hanlon: Writing, Data Collection, Data Analysis, Sample Preparation and Editing.

I. Saika-Voivod: Writing, Data Collection, Data Analysis, Editing, and Supervision.

M. Shajahan G. Razul: Writing, Data Collection, Data Analysis, Editing, and Supervision.

G. T. Andrews: Writing, Data Collection, Data Analysis, Editing, Supervision, Conceived and Administered Experiment.

6.1 Abstract

We performed molecular dynamics simulations to investigate the viscoelastic properties of binary aqueous protein solutions containing an antifreeze protein, a toxin protein, and bovine serum albumin. These simulations covered a temperature range from 280K to 340K. Our findings demonstrate that lower temperatures are associated with higher viscosity as well as a lower bulk modulus and speed of sound for all the systems studied. These results align with previous experimental studies conducted on protein-water solutions. Furthermore, we analyzed the influence of protein concentration on the viscoelastic properties of the antifreeze protein solution. We observed a consistent increase in the bulk modulus, speed of sound, and viscosity as the protein concentration increased. Remarkably, our molecular dynamics simulations results closely resemble the trends observed in Brillouin scattering experiments on aqueous protein solutions. The similarity thus validates the use of simulations in studying the viscoelastic properties of protein water solutions. Ultimately, this work provides motivation for the integration of computer simulations with experimental data and holds potential for advancing our understanding of both simple and complex systems.

6.2 Introduction

Water is vital for life on Earth yet there are still many properties of water and its interaction with other molecules that are not fully understood. In particular, there has been considerable recent interest in the viscoelastic properties of aqueous biomacromolecular solutions, especially water-protein solutions, due to their importance in understanding fundamental biophysical and biochemical processes.

Various experimental techniques have been used to study the viscoelastic properties of aqueous protein solutions [1–4]. A previous Brillouin scattering study examined aqueous solutions of lysozyme and bovine serum albumin (BSA) with varying concentrations [4]. The study found that increasing protein concentration increases both sound velocity and viscosity, determined by spectral peak position and peak full width at half maximum (FWHM), respectively. In a rheology study, the bulk and viscoelastic properties of BSA at low concentrations were investigated [3]. Both the Brillouin and rheology studies showed a strong dependence of viscoelasticity on protein concentration. Similarly, another study used Brillouin light scattering spectroscopy to examine the temperature dependence of the viscoelastic properties of snail mucus, a natural system consisting primarily of water and glycoprotein [1]. As the temperature increased, the speed of sound and storage modulus increased, while viscosity and hypersound attenuation decreased. Another notable feature present in the mucus data was a liquid-to-solid phase transition at around 270.5 K. Further experiments on diluted and dehydrated snail mucus showed significant variations in speed of sound, viscosity, and sound absorption as a function of protein concentration [5]. Rheology studies were also conducted on dehydrating snail mucus and revealed that the shear modulus increased with increasing degree of dehydration [2]. Overall, previous experimental studies have consistently demonstrated that the viscoelasticity of aqueous protein solutions is strongly influenced by protein concentration [1–4].

Somewhat surprisingly, molecular dynamics (MD) simulations have not been used much for investigating bulk viscoelastic properties such as bulk modulus, speed of sound, and viscosity of aqueous protein solutions nor fluids in general. Only a few MD studies have explored the dynamical properties of aqueous protein solutions containing collagen molecules and different co-solvents [6, 7]. Specifically, MD simulations have been employed to determine the viscosity and relaxation times of collagen molecules, aiming to explore their elastic behavior and investigate the possible role of cross-linked collagen molecules in viscoelastic properties, as previously hypothesized [6, 8, 9]. A likely reason for the limited studies on the viscoelastic properties of aqueous protein solutions is possibly due to the overall accuracy and reliability of the simulations which depend on a number of factors, including the choice of force field, system size, and simulation time.

In this paper we demonstrate the capabilities of MD simulations in exploring fundamental properties of fluids by obtaining bulk viscoelastic properties of protein-water systems over the temperature range 280 K $\leq T \leq$ 340 K. We found that the magnitude and temperature dependence of the bulk modulus, sound speed, and shear viscosity of simulated aqueous protein solutions containing an antifreeze protein, a toxin protein, and BSA are similar to those observed in previous experimental studies on aqueous protein solutions. The combination of MD simulations with experimental results therefore provides a more comprehensive understanding of the physics of molecular interaction in water-macromolecule solutions that could lead to advancements in fields such as drug discovery, materials science, biochemistry and biophysics.

6.3 Computational Details

Table 6.1 gives an overview of the simulated systems studied in the present work. These included aqueous solutions of an antifreeze glycoprotein found in eelpout, a cross-linking toxin protein found in *Vibrio cholerae*, and the widely studied bovine serum albumin [10–12]. The initial protein configurations were obtained from the Protein Data Bank (PDB). The naming convention employed to designate each system consists of the PDB ID of the protein followed by the weight percentage of that protein in the system. For instance, antifreeze protein 1MSI at 4 wt% is referred to as 1MSI-4. The antifreeze glycoprotein 1MSI was used due to its simple structure and the fact that antifreeze glycoprotein solutions have recently been the subject of experimental work [1, 5]. The toxin protein with PDB ID 4GQK was used primarily for its ability to cross-link. Lastly, BSA (PDB ID 4F5S) was used since it is an extensively studied molecule. Moreover, in addition to the specific reasons for using the chosen proteins, their collective inclusion enables a comprehensive study of proteins characterized by progressively higher molecular weights. This allows for the potential to provide insights into the influence of protein size on the viscoelastic properties of such systems.

The MD simulations were carried out in the isothermal-isobaric (NPT) ensemble using GROMACS v2022.3 [13–15]. We used the TIP4P/2005 water model (volume $4 \times 4 \times 4$ nm^3, density 0.992 g/cm^3) as a control system due to its ability to accurately represent the properties of water over the temperature range studied [16–18]. Proteins in the system interact using the All-Atom Optimized Potential for Liquid Simulations (OPLS-AA) [19] which was chosen due to its good description of liquid organic systems and ability to reproduce thermodynamic properties such as density and heat of vaporization, structural properties, as well as free energies of hydration [20]. The equations of motion were integrated with a time step of 2 fs using the leapfrog algorithm [21]. Temperature was held constant using a Nosé-Hoover thermostat with a time constant of 0.1 ps. The pressure was held constant using the Parrinello-Rahman barostat with a time constant of 2 ps. The viscoelastic properties of each

Table 6.1: Overview of protein-water systems used in the present molecular dynamics simulations. The temperature range studied was 280 K - 340 K.

System →	1MSI/Water[1]	4GQK/Water	4F5S/Water
Protein Data Bank ID	1MSI	4GQK	4F5S
Protein	Antifreeze Glycoprotein QAE(HPLC 12)	VgrG1-ACD with ADP	Bovine Serum Albumin
Weight of Protein (kDa)	7.4	44.3	133.3
# of Protein Molecules in System	1, 3, 5	2	1
# of Water Molecules in System	9970, 8110, 7190	52,030	258,840
Protein Concentration (wt %)	4, 12, 22	4	3
System Volume (nm^3)	6.5×6.5×6.5	12×12×12	20×20×20
System Density[2] (g/cm^3)	1.009, 1.025, 1.060	1.024	1.010
Rationale for Use	Simple structure & an antifreeze glycoprotein	Ability to cross-link in solution	Availability & a widely studied protein
Miscellaneous Notes	Antifreeze glycoprotein found in eelpout [10]	Toxin protein found in *Vibrio cholerae* [11]	Structure determined from Ref. [12]

[1] Given that this system comprises three distinct protein concentrations, we will adopt the following naming convention to designate each respective system along with its corresponding protein concentration: 1MSI-4, 1MSI-12, 1MSI-22, 4GQK-4, and 4F5S-3.

[2] Density of each system at 300 K

system (see Table 6.1) were investigated over the temperature range 280 K to 340 K. For each system, the size of simulation box and number of solute molecules vary due to the differing sizes of the proteins used and the desire to replicate approximate protein concentrations used in experimental work.

6.4 Results & Discussion

6.4.1 Bulk Modulus

Figure 6.2 shows the bulk modulus (K_s) for solutions studied in this work (see Table 6.1) obtained by analyzing the fluctuations in volume and pressure in the simulations. For most systems, the bulk modulus increases with increasing temperature until it reaches a maximum value near 330 K. However, exceptions to this trend are observed in 1MSI-12 and 1MSI-22, where the bulk modulus exhibits a maximum at 320 K and 300 K, respectively. The difference in the maximum bulk modulus for these two solutions is caused by the increased protein concentration in each system. Additionally, in the case of 1MSI solutions, higher protein concentrations lead to a larger bulk modulus. The presence of a maximum in the bulk modulus also suggests that the molecular structure in each system is most rigid at this temperature.

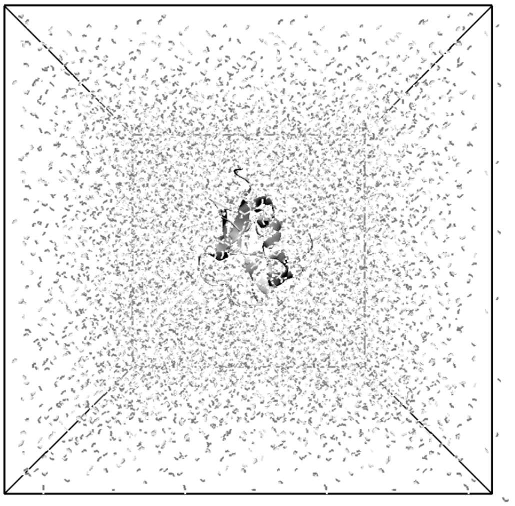

Figure 6.1: Representative simulation box of the 1MSI-4 system containing a single 1MSI protein (at center of box) and 2417 water molecules (grey flecks). Figure was produced using VMD v.1.9 [22].

Figure 6.3 illustrates the temperature at which the bulk modulus is at a maximum for each 1MSI solution. It is evident that as protein concentration increases, the temperature at which the maximum bulk modulus occurs decreases. The reason behind this phenomenon is due to the fact that the behavior of water and its bulk modulus (compressibility) is influenced by hydrogen bonds between water molecules and proteins and the presence of proteins has been known to disrupt these bonds [23].

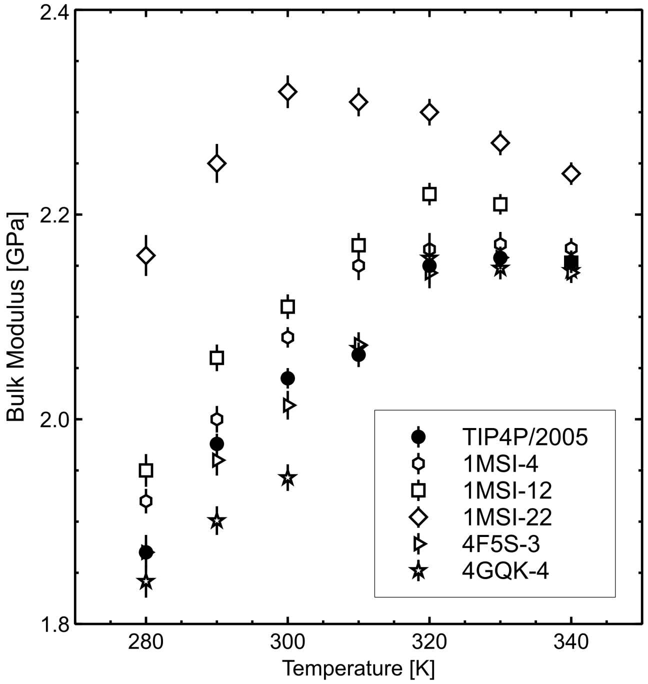

Figure 6.2: Temperature dependence of bulk modulus for water and aqueous protein solutions with different protein species and concentration.

6.4.2 Sound Velocity

The temperature dependence of the sound velocity for each of the protein-water systems was determined directly from the bulk modulus and the solution mass density ρ using the relation

$$v = \sqrt{\frac{K_s}{\rho}}. \tag{6.1}$$

As shown in Fig. 6.4, the behaviour is qualitatively similar for all systems. There is a steady increase in sound velocity with increasing temperature for temperatures at the lower end of the investigated range while at higher temperatures the velocity decreases with increasing temperature. The maximum in sound velocity occurs at ~ 330 K for systems with low protein concentrations (3-4%) and at slightly lower temperatures for those with higher concentrations (12% and 22%).

In the case of the 1MSI systems, the sound velocity displays a strong dependence

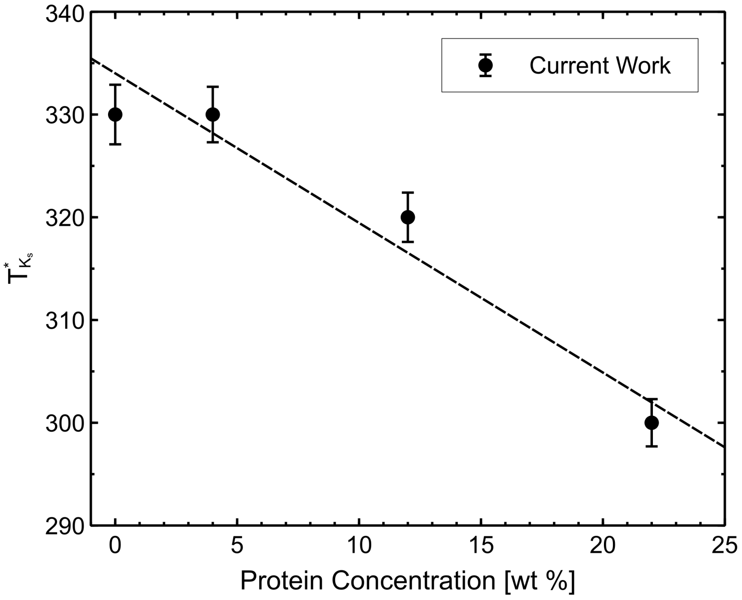

Figure 6.3: Temperature at which maximum bulk modulus occurs ($T^*_{K_s}$) as a function of concentration for 1MSI solutions. The line of best fit, represented by the dashed line with the equation $T^*_{K_s} = 337[X_p]$ - 1.68, where $[X_p]$ denotes the protein concentration. Uncertainty is approximately the size of the symbols.

on concentration. Specifically, an increase in protein concentration generally leads to a higher sound velocity, except for the values at 340 K, where 1MSI-4 exhibits a larger sound velocity than 1MSI-12. The reason for this unexpected behavior at 340 K is currently unknown. Additionally, as the concentration increases, the maximum sound velocity for the 1MSI systems occurs at lower temperatures. This can be seen in Fig. 6.3 which shows the temperature at which the maximum bulk modulus occurs, directly related to the speed of sound via Eq. 6.1. This indicates a complex interplay between concentration, temperature, and sound velocity within the 1MSI system. Notably, except at the highest temperatures, the sound velocities for the 1MSI systems are larger than those for water. Conversely, the 4F5S-3 and 4GQK-4 systems exhibit sound velocity values that closely resemble those of water, although these velocities are generally lower than those of water, despite having protein concentrations similar to 1MSI-4. This observation is interesting because it demonstrates the impact of

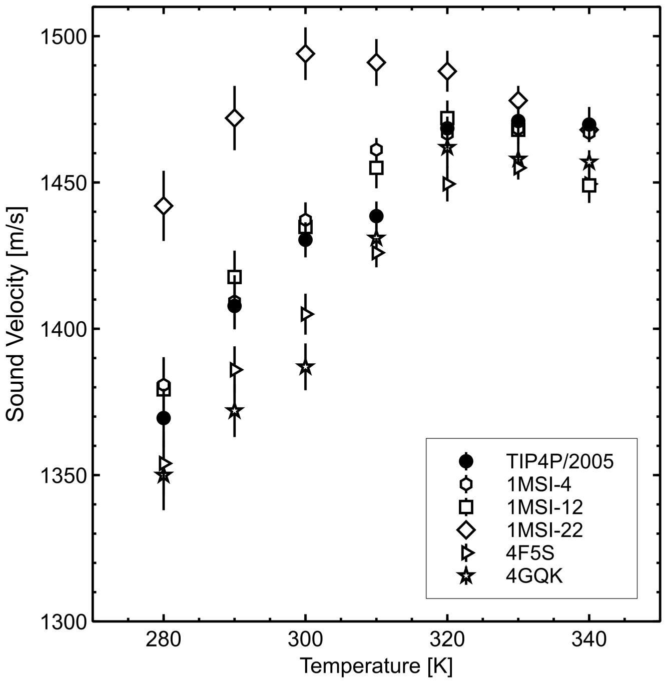

Figure 6.4: Temperature dependence of sound velocity of water and aqueous protein solutions with different protein species and concentration.

protein species on sound velocity in aqueous protein solutions, ranging from a decrease relative to v_{H_2O} to an increase relative to v_{H_2O}.

The sound velocities for 1MSI-4 and 1MSI-12 systems are similar for all temperatures but quite different from those of the 1MSI-22 system. Furthermore, the sound velocity for the 1MSI-22 system is also much greater than for all other systems, the difference being most obvious at lower temperatures ($T \leq 300$ K). This overall larger sound velocity for the 1MSI-22 system can be understood by noting that sound velocity is directly related to bulk modulus of the system. Therefore, with increased protein concentration, the liquid becomes less compressible than at lower concentrations resulting in an increased bulk modulus and consequently, sound velocity.

Another notable feature in the bulk modulus and sound velocity data is the near convergence of values for all systems near 340 K (see Fig. 6.4). At higher temperature

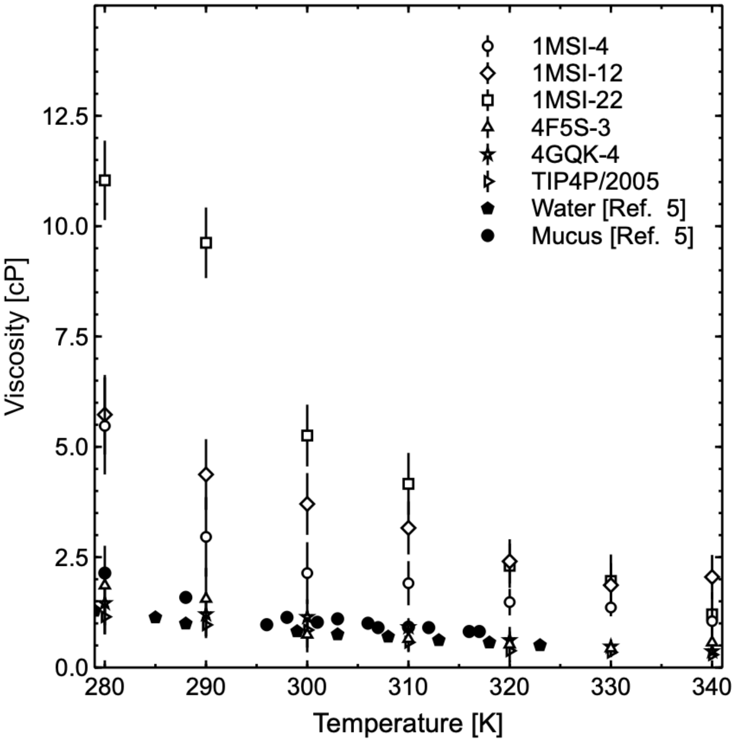

Figure 6.5: Shear viscosity of water and aqueous protein solutions versus temperature for proteins 4F5S, 4GQK, and 1MSI at concentrations of 4%, 12%, and 22%. Also shown for the purposes of comparison are apparent viscosity values for water and snail mucus, a natural system consisting primarily of water and glycoproteins, obtained from Brillouin scattering experiments [1].

this type of feature has been associated with protein denaturation and is consistent with nuclear magnetic resonance studies and MD simulations on lysozyme-water solutions that provide evidence for denaturation at ~ 340 K [24, 25]. However, it is worth noting that our investigation into the temperature dependent changes in the radius of gyration did not reveal any signs of protein denaturation occurring as there was no obvious change in the data.

6.4.3 Shear Viscosity

Figure 6.5 shows the shear viscosity as a function of temperature, calculated using the Einstein relation [13]

$$\eta = \lim_{t\to\infty} \frac{V}{k_B T} \frac{d}{dt} \left\langle \left(\int_{t_0}^{t_0+t} P_{xz}(t')dt' \right)^2 \right\rangle_{t_0}, \tag{6.2}$$

where V and T are the volume and temperature of the system, respectively. $P_{xz}(t')$ is the off-diagonal component of the pressure tensor at time t', k_B is the Boltzmann constant, t_0 is the starting time, and t represents the integration time. Our results for the TIP4P/2005 water model show a shear viscosity value of 0.85 ± 0.09 cP at 300 K, which is in good agreement with the previously obtained value of 0.855 cP at 298 K from Ref. [26].

Within uncertainty the viscosity of all systems decrease with increasing temperature over the entire temperature range studied. This trend aligns with experimental findings on similar protein-water systems [1, 27–29] (see apparent viscosity results for snail mucus, a natural water-glycoprotein system in Fig. 6.5). For the 1MSI solutions, there is an non-linear increase in shear viscosity as the temperature decreases. It is also clear that the shear viscosity of the 1MSI solutions is strongly influenced by protein concentration. In contrast, the magnitude and behaviour of the shear viscosity of the simulated 4GQK-4 and 4F5S-3 solutions are similar to those of TIP4P/2005.

Figure 6.6 displays the natural logarithm of shear viscosity as a function of inverse temperature for all systems in this study. All simulated systems show a linear dependence on $1/T$ over the entire range studied. We therefore fit the Arrhenius relationship

$$\eta = \eta_0 e^{E_a/k_B T} \tag{6.3}$$

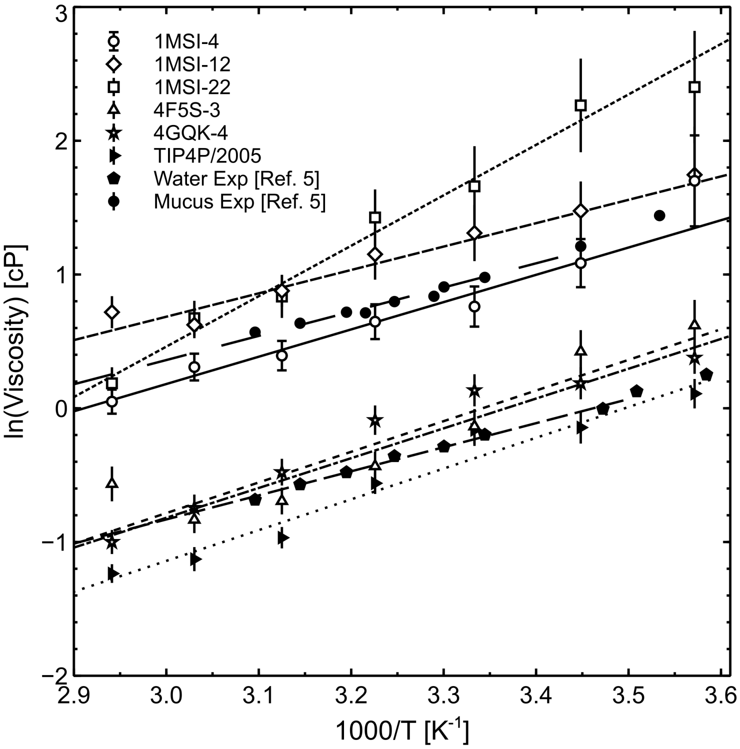

Figure 6.6: Plot of natural logarithm of shear viscosity of simulated systems as a function of temperature. Solid lines indicate best fits for the entire temperature region. Also shown for the purposes of comparison is the natural logarithm of apparent viscosity for water and snail mucus, a natural system consisting primarily of water and glycoproteins, obtained from Brillouin scattering experiments [1].

to the simulation data to obtain the activation energy E_a and entropic pre-factor η_0 (see Table 6.2). Notably, with the exception of 1MSI-22 the protein-water systems investigated in the current study have similar values of activation energy, ranging from 16.7 to 18.5 kJ/mol. These findings are consistent with previous experiments on aqueous protein and polymer systems [1, 27–29], where the E_a values were approximately 14-24% lower than those observed in our simulations. To address this difference we normalized the activation energy relative to ultra-pure water for experimental data and the TIP4P/2005 water model for simulations. This normalization allowed us to mitigate the influence of differences between the ultra-pure water used in experiments and the water model used in simulations. Figure 6.7 presents the ratios E_a^P/E_a^W

Table 6.2: Best-fit parameters for fit of function $\ln(\eta) = \ln\eta_0 + E_a/k_BT$ to computationally determined shear viscosity.

System	$\ln\eta_0$ (cP)	E_a kJ/mol	R^2
1MSI-4	-5.9 ± 0.8	16.7 ± 0.7	0.987
1MSI-12	-4.3 ± 0.9	14.5 ± 0.9	0.990
1MSI-22	-11.5 ± 0.9	31.3 ± 0.8	0.977
4GQK-4	-6.3 ± 0.6	18.2 ± 0.7	0.985
4F5S-3	-3.6 ± 0.9	18.5 ± 0.9	0.977
TIP4P/2005	-7.4 ± 0.6	18.5 ± 0.5	0.983
Water[1]	-5.6 ± 0.3	13.8 ± 0.3	0.991
Mucus[2]	-4.3 ± 0.3	13.6 ± 0.4	0.988
Water[3]	—	13.6 ± 0.6	—

for the protein-water solutions studied in this work and those obtained from Brillouin spectroscopy for various dilutions of snail mucus [5], E_a^M/E_a^W. Remarkably, except for 1MSI-22, the ratios for the protein-water systems analyzed in our research were close to unity. This finding aligns with the behavior observed in natural snail mucus, where the activation energy exhibited negligible variation across different concentrations. It is also consistent with the results of a Brillouin scattering study of water-tert-butyl alcohol in which activation energy was found to be nearly independent of polymer concentration [27].

As evident from the results displayed in both Fig. 6.5 and 6.6, the simulated systems show good agreement with both water and natural snail mucus as previously obtained experimentally [1]. For example, considering the 1MSI solutions, which contain antifreeze proteins of varying concentrations, we see very similar behaviour in the viscosity of simulated protein systems with the experimental values obtained for water and natural snail mucus. Additionally, if we consider the data for the natural logarithm of viscosity as a function of temperature, we see a very similar trend between

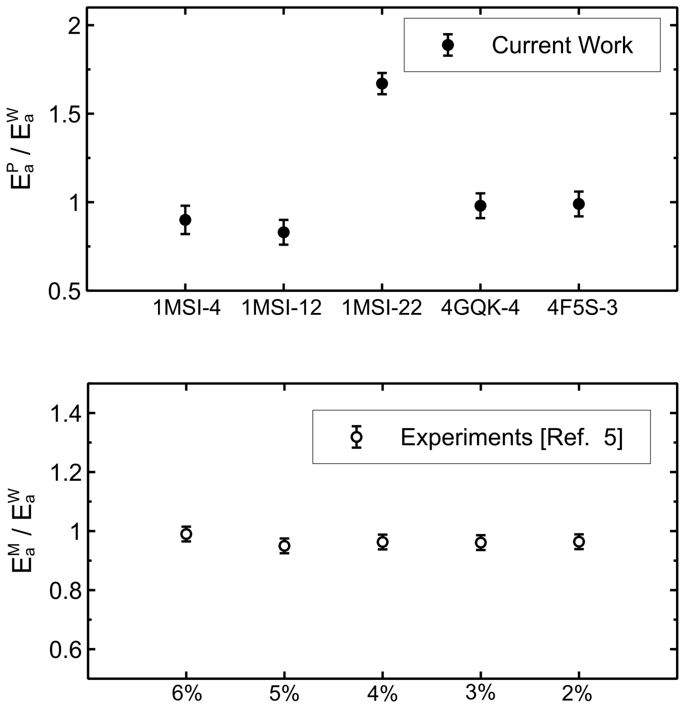

Figure 6.7: Top Panel: Ratio of activation energy for the simulated aqueous protein solution (E_a^P) to activation energy obtained for the TIP4P/2005 water model (E_a^W). Bottom Panel: Ratio of activation energy for hydrated snail mucus (E_a^M) to activation energy for ultra-pure water (E_a^W), as reported in Ref. [5]. The labels on the horizontal axis in the lower panel are approximate glycoprotein weight percentages. Error bars are approximately the size of the symbols.

the 1MSI-4 system and natural snail mucus. In fact, we know from Ref. [1] that for T ≤ 290 K, the viscous behaviour of snail mucus transitions from Arrhenius to non-Arrhenius. We can possibly start to see a similar feature if we consider the single data point at 280 K (~ 3.6 on x-axis), where the natural logarithm of viscosity increases substantially at this point (see Fig. 6.6). Overall, the behaviour observed in the shear viscosity is consistent with the trends observed in experimental work, providing strong support that the simulations can accurately describe the bulk viscoelastic properties of these systems.

6.5 Conclusion

This study is one of very few, if not the only, study to systematically investigate the temperature dependence behavior of viscoelastic properties in aqueous protein solutions using molecular dynamics simulations, while also considering variations in protein sizes and concentration. We determined the temperature dependence of the adiabatic bulk modulus, sound speed, and viscosity, and found behaviour consistent with that observed in previous experimental work on protein-water systems [1, 5, 27–32]. The general agreement between the simulations results and experimental observations highlights the potential of the former in predicting the viscoelastic properties of macromolecular solutions and in providing complementary molecular-level insight into the behaviour of these systems.

6.6 Supplementary Material for: Probing the Viscoelastic Properties of Aqueous Protein Solutions using Molecular Dynamics Simulations

Table 6.3: Density, bulk modulus, sound velocity and viscosity for TIP4P/2005 at the indicated temperatures.

T (K)	T (°C)	ρ (kg/m^3)	Bulk Modulus (GPa)	Sound Velocity (m/s)	Viscosity (cP)
340.0 ± 1.7	20.0 ± 0.2	979.0 ± 1.3	2.2 ± 0.3	1479 ± 7	0.29 ± 0.03
330.0 ± 1.6	25.0 ± 0.2	984.0 ± 1.2	2.2 ± 0.3	1471 ± 8	0.34 ± 0.03
320.0 ± 1.7	30.0 ± 0.2	988.6 ± 1.4	2.2 ± 0.3	1479 ± 8	0.38 ± 0.04
310.0 ± 1.6	35.0 ± 0.2	989.1 ± 1.5	2.1 ± 0.3	1439 ± 8	0.57 ± 0.06
300.0 ± 1.8	40.0 ± 0.2	995.0 ± 1.4	2.1 ± 0.2	1430 ± 8	0.85 ± 0.08
290.0 ± 1.8	45.0 ± 0.2	998.3 ± 1.7	2.0 ± 0.2	1410 ± 8	0.97 ± 0.09
280.0 ± 1.8	50.0 ± 0.2	999.3 ± 1.6	1.9 ± 0.2	1370 ± 10	1.2 ± 0.1

Table 6.4: Density, bulk modulus, sound velocity and viscosity for 1MSI-4 at the indicated temperatures.

T (K)	T (°C)	ρ (kg/m^3)	Bulk Modulus (GPa)	Sound Velocity (m/s)	Viscosity (cP)
340.0 ± 1.6	50.0 ± 0.5	981.3 ± 1.4	2.2 ± 0.3	1467 ± 8	1.1 ± 0.1
330.0 ± 1.6	45.0 ± 0.5	985.3 ± 1.3	2.2 ± 0.3	1468 ± 8	1.4 ± 0.1
320.0 ± 1.7	40.0 ± 0.5	990.0 ± 1.4	2.2 ± 0.3	1467 ± 10	1.5 ± 0.2
310.0 ± 1.5	35.0 ± 0.5	994.1 ± 1.6	2.2 ± 0.3	1461 ± 11	1.9 ± 0.2
300.0 ± 1.5	30.0 ± 0.5	998.6 ± 1.7	2.1 ± 0.2	1437 ± 13	2.1 ± 0.2
290.0 ± 1.5	25.0 ± 0.5	999.1 ± 1.7	2.0 ± 0.2	1409 ± 13	3.0 ± 0.3
280.0 ± 1.5	20.0 ± 0.5	1002.0 ± 1.8	1.9 ± 0.2	1380 ± 15	5.5 ± 0.5

Table 6.5: Density, bulk modulus, sound velocity and viscosity for 1MSI-12 at the indicated temperatures.

T (K)	T (°C)	ρ (kg/m^3)	Bulk Modulus (GPa)	Sound Velocity (m/s)	Viscosity (cP)
340.0 ± 1.6	50.0 ± 0.5	1012.0 ± 1.6	2.2 ± 0.3	1449 ± 8	2.05 ± 0.2
330.0 ± 1.7	45.0 ± 0.5	1018.0 ± 1.8	2.2 ± 0.3	1468 ± 13	1.87 ± 0.2
320.0 ± 1.7	40.0 ± 0.5	1022.0 ± 2.0	2.2 ± 0.2	1472 ± 15	2.41 ± 0.2
310.0 ± 1.4	35.0 ± 0.5	1024.0 ± 2.2	2.2 ± 0.2	1455 ± 15	3.16 ± 0.3
300.0 ± 1.7	30.0 ± 0.5	1025.0 ± 2.5	2.1 ± 0.2	1434 ± 12	3.71 ± 0.4
290.0 ± 1.8	25.0 ± 0.5	1026.0 ± 2.6	2.1 ± 0.2	1417 ± 18	4.37 ± 0.4
280.0 ± 1.7	20.0 ± 0.5	1026.0 ± 2.6	2.0 ± 0.2	1380 ± 19	5.73 ± 0.5

Table 6.6: Density, bulk modulus, sound velocity and viscosity for 1MSI-22 at the indicated temperatures.

T (K)	T (°C)	ρ (kg/m^3)	Bulk Modulus (GPa)	Sound Velocity (m/s)	Viscosity (cP)
340.0 ± 1.5	50.0 ± 0.5	1044 ± 1.8	2.2 ± 0.3	1468 ± 11	1.21 ± 0.1
330.0 ± 1.6	45.0 ± 0.5	1049 ± 1.9	2.3 ± 0.4	1472 ± 13	1.96 ± 0.2
320.0 ± 1.7	40.0 ± 0.5	1054 ± 2.1	2.3 ± 0.4	1494 ± 18	2.31 ± 0.1
310.0 ± 1.8	35.0 ± 0.5	1057 ± 2.2	2.3 ± 0.4	1491 ± 18	4.16 ± 0.4
300.0 ± 1.6	30.0 ± 0.5	1060 ± 2.3	2.3 ± 0.3	1488 ± 17	5.26 ± 0.5
290.0 ± 1.7	25.0 ± 0.5	1061 ± 2.3	2.3 ± 0.3	1478 ± 15	9.62 ± 0.9
280.0 ± 1.7	20.0 ± 0.5	1060 ± 2.3	2.2 ± 0.3	1468 ± 14	11.04 ± 1.0

Table 6.7: Density, bulk modulus, sound velocity and viscosity for 4GQK-4 at the indicated temperatures.

T (K)	T (°C)	ρ (kg/m^3)	Bulk Modulus (GPa)	Sound Velocity (m/s)	Viscosity (cP)
340.0 ± 1.6	50.0 ± 0.5	991 ± 1.4	2.15 ± 0.3	1457 ± 12	0.37 ± 0.03
330.0 ± 1.6	45.0 ± 0.5	999 ± 1.5	2.15 ± 0.3	1458 ± 13	0.47 ± 0.05
320.0 ± 1.7	40.0 ± 0.5	1010 ± 1.6	2.16 ± 0.3	1462 ± 14	0.62 ± 0.06
310.0 ± 1.6	35.0 ± 0.5	1017 ± 1.7	2.07 ± 0.2	1431 ± 16	0.91 ± 0.08
300.0 ± 1.6	30.0 ± 0.5	1024 ± 1.9	1.94 ± 0.2	1387 ± 17	1.1 ± 0.1
290.0 ± 1.6	25.0 ± 0.5	1027 ± 1.9	1.90 ± 0.2	1372 ± 14	1.2 ± 0.2
280.0 ± 1.5	20.0 ± 0.5	1030 ± 2.1	1.84 ± 0.2	1350 ± 14	1.5 ± 0.2

Table 6.8: Density, bulk modulus, sound velocity and viscosity for 4F5S-3 at the indicated temperatures.

T (K)	T (°C)	ρ (kg/m^3)	Bulk Modulus (GPa)	Sound Velocity (m/s)	Viscosity (cP)
340.0 ± 1.7	50.0 ± 0.5	976 ± 1.4	1.87 ± 0.3	1449 ± 12	0.57 ± 0.06
330.0 ± 1.6	45.0 ± 0.5	985 ± 1.4	1.96 ± 0.3	1455 ± 13	0.43 ± 0.05
320.0 ± 1.5	40.0 ± 0.5	992 ± 1.6	2.01 ± 0.4	1448 ± 15	0.52 ± 0.05
310.0 ± 1.6	35.0 ± 0.5	999 ± 1.6	2.07 ± 0.4	1426 ± 14	0.64 ± 0.07
300.0 ± 1.8	30.0 ± 0.5	1010 ± 1.7	2.14 ± 0.5	1405 ± 14	0.74 ± 0.07
290.0 ± 1.8	25.0 ± 0.5	1013 ± 1.9	2.16 ± 0.5	1386 ± 16	1.56 ± 0.09
280.0 ± 1.7	20.0 ± 0.5	1019 ± 2.2	2.14 ± 0.5	1354 ± 17	1.9 ± 0.1

Bibliography

[1] Dillon Hanlon, Maynard J Clouter, and G Todd Andrews. Temperature dependence of the viscoelastic properties of a natural gastropod mucus by brillouin light scattering spectroscopy. *Soft Matter*, 2023.

[2] M. Denny. Mechanical properties of pedal mucus and their consequences for gastropod structure and performance. *American Zoology*, 24(1):23–36, 1984.

[3] V. Sharma, A. Jaishankar, Y. Wang, and G. McKinley. Rheology of globular proteins: apparent yield stress, high shear rate viscosity and interfacial viscoelasticity of bovine serum albumin solutions. *Soft Matter*, 7(11):5150–5160, 2011.

[4] A. Dmitriev, V. Vashchenkov, A. Fedoseev, and S. Lushnikov. Phase transformations of bovine serum albumin: Evidences from rayleigh-brillouin light scattering. *Journal of Raman Spectroscopy*, 50(4):537–547, 2019.

[5] D. F. Hanlon, M. J. Clouter, and G. T. Andrews. Influence of hydration and dehydration on the viscoelastic properties of snail mucus by brillouin spectroscopy, 2023.

[6] A. Gautieri, S. Vesentini, Alberto Redaelli, and Markus J Buehler. Viscoelastic properties of model segments of collagen molecules. *Matrix Biology*, 31(2):141–149, 2012.

[7] H. Wei, Y. Fan, and Y. Gao. Effects of urea, tetramethyl urea, and trimethylamine n-oxide on aqueous solution structure and solvation of protein backbones: a molecular dynamics simulation study. *The Journal of Physical Chemistry B*, 114(1):557–568, 2010.

[8] F. Silver, J. Freeman, Istvan Horvath, and William J Landis. Molecular basis for elastic energy storage in mineralized tendon. *Biomacromolecules*, 2(3):750–756, 2001.

[9] F. Silver, D. Christiansen, P. Snowhill, and Y. Chen. Transition from viscous to elastic-based dependency of mechanical properties of self-assembled type i collagen fibers. *Journal of Applied Polymer Science*, 79(1):134–142, 2001.

[10] Z. Jia, C. DeLuca, H. Chao, and P. Davies. Structural basis for the binding of a globular antifreeze protein to ice. *Nature*, 384(6606):285–288, 1996.

[11] E. Durand, E. Derrez, G. Audoly, S. Spinelli, M. Ortiz-Lombardia, D. Raoult, E. Cascales, and C. Cambillau. Crystal structure of the vgrg1 actin cross-linking domain of the vibrio cholerae type vi secretion system. *Journal of Biological Chemistry*, 287(45):38190–38199, 2012.

[12] A. Bujacz. Structures of bovine, equine and leporine serum albumin. *Acta Crystallographica Section D: Biological Crystallography*, 68(10):1278–1289, 2012.

[13] B. Hess, C. Kutzner, D. Van Der Spoel, and E. Lindahl. Gromacs 4: algorithms for highly efficient, load-balanced, and scalable molecular simulation. *Journal of Chemical Theory and Computation*, 4(3):435–447, 2008.

[14] E. Lindahl, B. Hess, and D. Van Der Spoel. Gromacs 3.0: a package for molecular simulation and trajectory analysis. *Molecular Modeling Annual*, 7:306–317, 2001.

[15] D. Van Der Spoel, E. Lindahl, B. Hess, G. Groenhof, A. Mark, and H. Berendsen. Gromacs: fast, flexible, and free. *Journal of Computational Chemistry*, 26(16):1701–1718, 2005.

[16] J. Abascal and C. Vega. A general purpose model for the condensed phases of water: Tip4p/2005. *The Journal of Chemical Physics*, 123(23):234505, 2005.

[17] M. González, C. Valeriani, F. Caupin, and J. Abascal. A comprehensive scenario of the thermodynamic anomalies of water using the tip4p/2005 model. *The Journal of Chemical Physics*, 145(5), 2016.

[18] Z. Yu, R. Shi, and H. Tanaka. A unified description of the liquid structure, static and dynamic anomalies, and criticality of tip4p/2005 water by a hierarchical two-state model. *The Journal of Physical Chemistry B*, 127(15):3452–3462, 2023.

[19] W. L Jorgensen, D. S Maxwell, and J. Tirado-Rives. Development and testing of the opls all-atom force field on conformational energetics and properties of organic liquids. *Journal of the American Chemical Society*, 118(45):11225–11236, 1996.

[20] R. Zangi. Refinement of the oplsaa force-field for liquid alcohols. *ACS omega*, 3(12):18089–18099, 2018.

[21] M. Cuendet and W. van Gunsteren. On the calculation of velocity-dependent properties in molecular dynamics simulations using the leapfrog integration algorithm. *The Journal of Chemical Physics*, 127(18):184102, 2007.

[22] W. Humphrey, A. Dalke, and K. Schulten. Vmd: visual molecular dynamics. *Journal of Molecular Graphics*, 14(1):33–38, 1996.

[23] P. Ball. Water as an active constituent in cell biology. *Chemical Reviews*, 108(1):74–108, 2008.

[24] F. Mallamace, C. Corsaro, D. Mallamace, P. Baglioni, H. Stanley, and S. Chen. A possible role of water in the protein folding process. *The Journal of Physical Chemistry B*, 115(48):14280–14294, 2011.

[25] Y. Zhang, M. Lagi, D. Liu, F. Mallamace, E. Fratini, P. Baglioni, Eugene Mamontov, Mark Hagen, and S. Chen. Observation of high-temperature dynamic crossover in protein hydration water and its relation to reversible denaturation of lysozyme. *The Journal of Chemical Physics*, 130(13), 2009.

[26] M. González and J. Abascal. The shear viscosity of rigid water models. *The Journal of Chemical Physics*, 132(9), 2010.

[27] L. Lupi, L. Comez, C. Masciovecchio, A. Morresi, M. Paolantoni, P. Sassi, F. Scarponi, and D. Fioretto. Hydrophobic hydration of tert-butyl alcohol studied by brillouin light and inelastic ultraviolet scattering. *Journal of Chemical Physics*, 134(5):02B603, 2011.

[28] L. Comez, L. Lupi, M. Paolantoni, F. Picchiò, and D. Fioretto. Hydration properties of small hydrophobic molecules by brillouin light scattering. *Journal of Chemical Physics*, 137(11), 2012.

[29] M. Pochylski, F. Aliotta, Z. Błaszczak, and J. Gapiński. Structural relaxation processes in polyethylene glycol/ccl4 solutions by brillouin scattering. *Journal of Physical Chemistry B*, 109(9):4181–4188, 2005.

[30] M. Bailey, M. Alunni-Cardinali, N. Correa, S. Caponi, T. Holsgrove, H. Barr, N. Stone, C. P. Winlove, D. Fioretto, and F. Palombo. Viscoelastic properties of biopolymer hydrogels determined by brillouin spectroscopy: A probe of tissue micromechanics. *Science Advances*, 6(44), 2020.

[31] Y. Trosel, L. Gregory, V. Booth, and A. Yethiraj. Diffusion nmr and rheology of a model polymer in bacterial cell lysate crowders. *Biomacromolecules*, 24(6):2469–2478, 2023.

[32] A. Milewska, J. Szydlowski, and L. Rebelo. Viscosity and ultrasonic studies of poly (n-isopropylacrylamide)–water solutions. *Journal of Polymer Science Part B: Polymer Physics*, 41(11):1219–1233, 2003.

Chapter 7

Brillouin light scattering studies of aqueous *E. Coli* cell lysate: Viscoelastic properties of a multimacromolecular solution

D.F. Hanlon, S. Hearvi, V. Booth and G. T. Andrews

Co-Authorship Statement

We, the authors of this manuscript, have contributed collectively to the research, writing, and preparation of this work. Each author's contribution is outlined below:

D. F. Hanlon: Writing, Data Collection, Data Analysis, Sample Preparation and Editing.

S. Heravi: Writing, Sample Preparation, Data Analysis, and Editing.

V. Booth: Writing, Sample Preparation, Data Analysis, Editing, and Supervision.

G. T. Andrews: Writing, Data Collection, Data Analysis, Editing, Supervision, Conceived and Administered Experiment.

7.1 Abstract

Brillouin spectroscopy was used to probe the viscoelastic properties of *E. coli* bacterial cell lysate in aqueous solution at GHz-frequencies over the range -5.0 °C $\leq T \leq$ 50.0 °C. This work offers a first temperature dependent study on cell lysate by Brillouin light scattering. A single peak was observed in the spectra and attributed to a longitudinal acoustic mode of the solution. The speed of sound, bulk modulus, apparent viscosity and hypersound attenuation were extracted from the frequency shift and FWHM of the spectral peak. This study demonstrate that the behavior of complex multimacromolecular solutions, as shown by *E. coli* lysate, can exhibit viscoelastic properties closely akin to those observed in simple binary aqueous protein solutions. Furthermore, our findings show that by analyzing the raw spectral signature of the Brillouin spectra, it may be possible to identify protein denaturation.

7.2 Introduction

Cell lysate is a complex mixture of biomolecules that is released when cells are ruptured. It finds wide application in various fields of research, including fundamental biological studies and biotechnological applications like protein purification [6]. Bacterial cell lysate, in particular, has been extensively investigated in cell-free metabolic engineering for producing target molecules and debugging pathways, offering potential advantages for engineering bacterial cells such as the commonly used lysate derived from *Escherichia coli* (*E. coli*) [15]. The lysate derived from *E. coli* has been used extensively in the past due to its well-characterized genetics, ease of cultivation, and relevance to both environmental and clinical settings of the parent bacterium [17]. The study of *E. coli* lysate has yielded valuable insights into the composition, molecular interactions, and biochemical processes within bacterial cells, thanks to the diverse assortment of biomolecules it contains [18]. These biomolecules, including proteins, nucleic acids, lipids, carbohydrates, and associated metabolites, play crucial roles in essential cellular functions like metabolism, gene expression, signal transduction, and cell division [18].

In the context of experimental fluids physics, cell lysate serves as a model solute for studying aqueous multimacromolecular solutions commonly found in biological systems. Understanding these solutions has proven challenging due to their complex composition, however, their complexity also makes the system interesting as it consists of a diverse array of molecules differing in size, charge, and shape. To investigate the diffusivity of proteins and polymer crowding agents in cell lysate solutions, nuclear magnetic resonance techniques have been employed [28, 29]. In one study, the rotational and translational diffusion of a 7.4 kDa test protein, chymotrypsin inhibitor 2, was examined in the presence of synthetic polymer crowders, protein crowders, and lysate [29]. The results indicated that artificial crowders like poly(vinylpyrrolidone) 40 and Ficoll do not accurately replicate cellular environments due to the absence of many non-covalent interactions that are present in real cells. Another study investigated the effects of polymer crowders of polyethylene glycol in bacterial cell lysate, revealing that polyethylene glycol is also unsuitable as an excluded-volume crowding agent due to its strong association with lysate components [28]. Rheology techniques have also been employed to investigate the low-frequency viscoelasticity of cell lysate solutions [21, 28, 29]. These studies focused on shear and storage moduli, as well as viscosity in relation to shear thinning. Interestingly, all of these parameters exhibited a slight decrease with increasing shear rate. The high-frequency viscoelastic properties of cell lysate solutions, however, have not been examined. Such high-frequency viscoelastic characterization would inform the testing and refinement of theoretical models based on simpler systems to ensure that they capture the essential physics necessary to describe the behavior of more complex systems.

This paper reports the results of Brillouin light scattering experiments with an aqueous solution of *E. coli* cell lysate over the temperature range $-5.0\ ^{\circ}\mathrm{C} \leq T \leq 50\ ^{\circ}\mathrm{C}$. This is the first study to investigate the GHz-frequency viscoelastic properties of a cell lysate solution. We determined the hypersound velocity, bulk modulus, apparent viscosity and hypersound attenuation as a function of temperature. The results of this work provide new insight into the physics of complex multimacromolecular solutions that mimic real-world biological systems.

7.3 Methodology

7.3.1 Solution Preparation

A 500 mL flask containing 75 mL of Lysogeny Broth (LB) media, consisting of 5 g of yeast extract, 10 g of NaCl, and 10 g of tryptone [1], was closed with a sponge plug and aluminum foil, and autoclaved for sterilization. After reaching room temperature, overnight cultures of *E. coli* JM109 were prepared by inoculating the 75 mL of LB media with 1 mL aliquots of frozen glycerol cell stocks. The inoculated cultures were placed in a 30 °C incubator with shaking at 150 rpm, protected with a foam stopper. Six 4 L flasks, each containing 1 L of LB media, were pre-warmed to 37 °C. The following day, the flasks were inoculated with 1 mL of overnight culture per 100 mL of fresh LB media and incubated at 37 °C with shaking at 175 rpm. Each culture was protected with a foam stopper.

Cells were harvested during the midlog phase at an absorption of 600 nm (A_{600}) ranging from 0.6 to 1.0. The absorption is a measure of the optical density (OD) and is often used to characterize the concentration of cells in a culture. The higher the OD implies a higher cell concentration [30]. The harvested cells were centrifuged at 5670 g for 20 minutes at 4 °C. The resulting pellet was subjected to three cycles of the French press at a pressure of 10,000 psi (6.9×10^7 Pa) and maintained at 4 °C to mechanically lyse the cells. This method of lysing the cell involves passing the pellet through a tiny valve at extremely high pressures. As the cells leave the valve, the pressure difference between the valve pressure and the surrounding atmospheric pressure generates significant shear stress, which eventually causes the cells to burst. The volume of cell lysate obtained was approximately 30 mL. Once complete, the lysate was subject to lyophilization to remove water. To begin this process, the lysate was stored in a freezer set at -80°C for 24 hours. Subsequently, the lysate is transferred into a vacuum chamber, where it undergoes freeze-drying over the duration of 48 hours. Once freeze-dried, the volume reduced to ~ 5 mL. The lyophilized cell lysate was stored in a 15 mL falcon tube at -20 °C for future use.

To prepare the cell lysate solution, approximately 0.3 g of cell lysate was carefully added to a glass sample cell. The lysate was dissolved in 4.0 ± 0.1 ml of water. This gives a water concentration comparable to that inside cells. The solution was then thoroughly mixed for approximately 10 minutes using a stirring stick to promote uniform dispersion of the components. Following the completion of the mixing step, Brillouin scattering experiments were promptly initiated.

The density of the aqueous cell lysate solution was determined to be $\rho = 1.0 \pm 0.1$

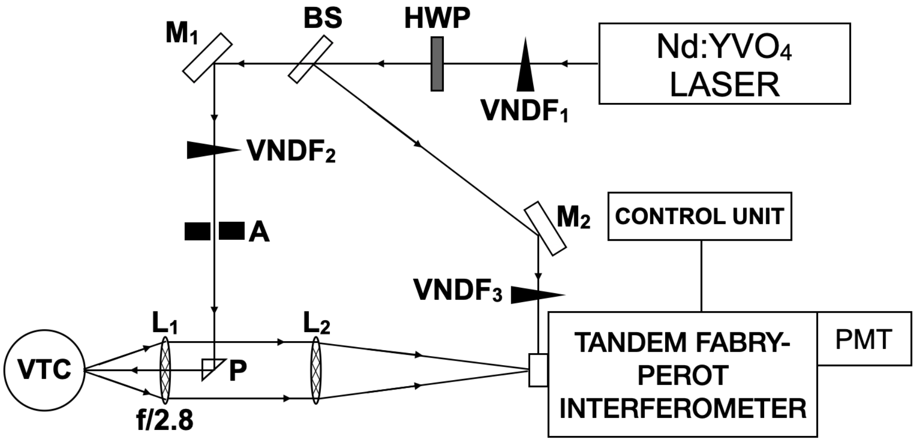

Figure 7.1: Optical setup for Brillouin scattering used in this study. VNDF - Variable neutral density filter, HWP - half wave plate, BS - beam splitter, M - mirror, VNDF - variable neutral density filter, A - aperture L - lens, P - prism, VTC - variable temperature chamber, PMT - photomultiplier tube.

g/cm^3, using the equation for a two-component solution

$$\rho = \frac{m_W + m_L}{\frac{m_W}{\rho_w} + \frac{m_L}{\rho_L}}, \tag{7.1}$$

where $\rho_W = 0.997$ g/cm^3 is the density of water, $\rho_L = 1.41$ g/cm^3 (dried) [10] is the density of cell lysate, and m_W and m_L are the mass of water and cell lysate (dried), respectively.

7.3.2 Brillouin Spectroscopy

Brillouin spectroscopy is a technique based on inelastic light scattering that enables the investigation of thermal acoustic phonons within a medium. For a 180° backscattering geometry as used in the present work, application of energy and momentum conservation to the scattering process reveals that the phonon velocity, v, and frequency shift of the Brillouin peak, f_B, are related by

$$v = \frac{f_B \lambda_i}{2n}, \tag{7.2}$$

where n is the refractive index of the target material at the incident light wavelength λ_i. The refractive index of the cell lysate solution used in the present work was taken to be equal to that of water, $n = 1.33$.

The apparent viscosity $\eta = 4\eta_s/3 + \eta_b$, where η_s and η_b are the shear and bulk viscosity, respectively, is related to the full width at half maximum (FWHM) of the Brillouin peak due to the longitudinal acoustic mode via [26],

$$\Gamma_B = \frac{16\pi^2 n^2}{\rho \lambda_i^2}\left[\eta + \frac{\kappa}{C_p}(\gamma - 1)\right], \tag{7.3}$$

where ρ is the density, κ is the thermal conductivity, and $\gamma = C_p/C_v$ is the ratio of specific heat at constant pressure to that at constant volume. The second term in the brackets of this expression is usually neglected for simple liquids, thus leaving the expression for viscosity [26],

$$\eta = \frac{\rho \lambda_i^2}{16\pi^2 n^2}\Gamma_B. \tag{7.4}$$

Knowledge of the hypersound velocity and apparent viscosity permits the real and imaginary parts of the complex longitudinal modulus, $M = M' + iM''$, to be determined through the relations

$$M' = \rho v^2 \tag{7.5}$$

and

$$M'' = 2\pi\eta f_B, \tag{7.6}$$

where M' and M'' are referred to as the storage and loss moduli, respectively [3].

The frequency-independent sound absorption coefficient may also be determined from Brillouin data through [26],

$$\frac{\alpha}{f^2} = \frac{\Gamma_B}{2vf_B^2}. \tag{7.7}$$

Brillouin spectra were collected using the 180° backscattering setup depicted in Fig. 7.1. A single-mode Nd:YVO$_4$ solid-state laser (Coherent Verdi-2) with an output power of 1.66 W and an emission wavelength of 532 nm served as the incident light source. A half-wave plate (HWP) was used to rotate the plane of polarization from vertical to horizontal. After leaving the half-wave plate, the beam was divided into a reflected reference beam and a transmitted sample probe beam by a beam splitter (BS). The reference beam is used in conjunction with a mechanical shutter system to maintain interferometer alignment and to prevent saturation of the photomultiplier tube (PMT) by intense elastically scattered light from the sample. The transmitted beam was reflected through an angle of 90° by front surface mirror (M1) and incident on a right-angle prism (P) where it underwent total internal reflection. The probe beam was then focused onto the sample using a camera lens (L1) with a focal length of 5 cm and an f/# of 2.8. Two variable neutral density filters (VNDF1 and VNDF2) were placed in the beam path to reduce the power at the sample to ~ 100 mW. Scattered light was collected and collimated by the same camera lens and subsequently focused onto the 450 μm-diameter input pinhole of a six-pass tandem Fabry-Perot interferometer by a f = 40 cm lens (L2). The frequency-analyzed scattered light transmitted by the interferometer was incident on the photocathode of a photomultiplier tube (PMT) where it was converted to an electrical signal and sent to a computer for recording and display.

The sample was housed in a custom-built variable temperature chamber (VTC). A Lakeshore Cryotronics temperature controller was used in conjunction with a resistor and thermoelectric cooler to regulate sample temperature. Depending on the target temperature for the experiment, either the heater or the cooler was initially activated. Once the desired temperature was reached, the heater and cooler worked in tandem to maintain the sample at that temperature. If the temperature exceeded the desired setpoint, the heater was shut-off and the cooler was switched on to reduce the temperature to the setpoint. Conversely, when the sample dropped below the setpoint, the cooler was turned off and the heater was activated to return the temperature to the setpoint. The accuracy of this variable temperature chamber was ±0.4 °C. Further details can be found in Ref. [11].

7.4 Results and Discussion

7.4.1 Brillouin Spectrum

General Features

Figure 7.2 shows Brillouin spectra collected from the *E. coli* lysate solution at temperatures ranging from -5.0 °C to 50 °C. The chronological order in which the spectra were collected is also indicated. A single Brillouin doublet was observed in the spectra at ~ ±7.2 GHz and attributed to the longitudinal acoustic mode of the cell lysate solution. Brillouin peak frequency shifts and linewidths (FWHM) were obtained by fitting

Lorentzian functions to the Stokes and anti-Stokes Brillouin peaks and averaging the resulting best-fit parameters. To obtain linewidths, the instrumental linewidth of 0.3 GHz was subtracted from FWHM values obtained from the Lorentzian fits. Estimated uncertainties in peak parameters (frequency shift and FWHM) were obtained from the uncertainty in the Lorentzian fits.

Sedimentation Effects

It was noted that the frequency shifts of Brillouin peaks in the first three spectra (obtained at 25 °C, 30 °C, and 35 °C and collected consecutively within an hour after solution preparation) trended toward that of water, raising concerns about the integrity of the data collected. The reason for this was later discovered to be sedimentation of larger particles present in the cell lysate, as made apparent by the presence of an ~ 2 mm-thick white residue at the bottom of the sample cell when removed from the temperature-controlled chamber at the conclusion of the experiment. These larger particles likely include remnants of the bacterial cell wall (characteristic size of ~ 1 μm [12, 25]), and not molecular constituents such as proteins, nucleic acids, or lipids due to the small sizes of the latter (see Table 7.1). There is also a small percentage of smaller particles such as ions, metabolites, and polysaccharides [13] not included in Table 7.1 due to their minimal abundance and significant variation in radii and density. This is in accord with Stokes' Law which predicts that the terminal velocity of a particle in a fluid is proportional to the square of its radius [4] (the strongest dependence on any parameter in this equation). With this in mind, the sedimentation time was estimated by first stirring the solution for approximately 10 minutes until homogeneous (as for the as-prepared solution at the outset of the experiment) and then visually monitoring it until the larger particles had settled. This time was found

Table 7.1: The approximate radius and density of cellular components in bacterial cells, along with their composition by weight [13].

Molecule	Radius (nm)	Mass Density (g/cm^3)	Abundance % Dry weight
Proteins	2 - 10 [31]	~ 1.35 [10]	50 - 55 [9]
RNA	7 - 10 [5]	~ 2.00 [2]	20 [9]
Phospholipids	0.5 - 1 [20]	~ 1.01 [14]	7 - 9 [9]
DNA	3 - 5 [27]	~ 1.70 [2, 23]	3 [9]

to be ~ 45 minutes. It is therefore likely that the spectra collected at 25°C, 30°C, and 35°C were affected by sedimentation. This was considered when analyzing the experimental results. It should also be noted that the probing incident laser beam was not impeded by the settled residue.

Temperature Dependence

Figure 7.3 shows the temperature dependence of the Brillouin peak frequency shift for water and the cell lysate solution. In general, the frequency shift for the lysate solution increases with increasing temperature. Previous Brillouin scattering work on aqueous protein systems have consistently reported a similar trend [3, 7, 8, 11, 16, 19, 22]. Notably, at higher temperatures, the frequency shift for the lysate solution has values that closely resemble those of water. For temperatures below T ~ 10 °C, however, a noticeable difference develops between the peak frequency shifts for water and the cell lysate solution.

Figure 7.3 also shows the Brillouin peak linewidth as a function of temperature for water and cell lysate. Unlike the peak frequency shift, the FWHM for the lysate solution is different from that of water over the entire temperature range studied. This is a clear indication that even though larger particles in the cell lysate have settled-out, smaller particles such as protein and lipid molecules remain in solution.

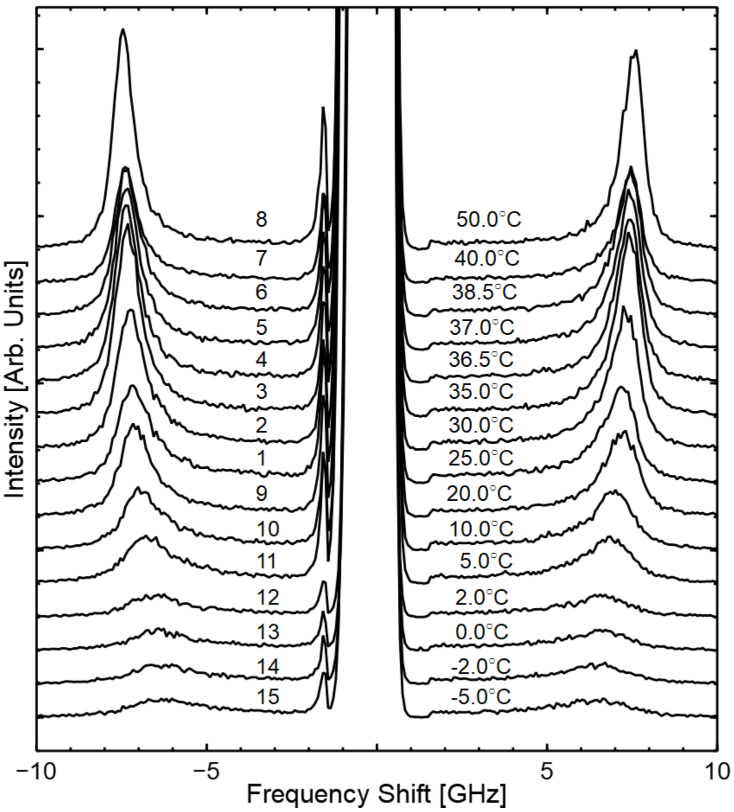

Figure 7.2: Brillouin spectra of an *E. coli* bacterial cell lysate-water solution collected at the temperatures indicated.

The FWHM begins to become appreciably different from that of water for $T \leq 10$ °C, the same temperature range as noted above for the Brillouin peak frequency shift.

7.4.2 Viscoelastic Properties

Temperature Dependence

Figure 7.4 presents viscoelastic properties for water and cell lysate solution over the range -5.0 °C to 50.0 °C determined from the Brillouin data using equations given in Sec. 7.3.2. As can be seen, the viscoelastic properties of the cell lysate solution obtained from the first few post-sedimentation spectra (#4 - #8 in Fig. 7.2, collected

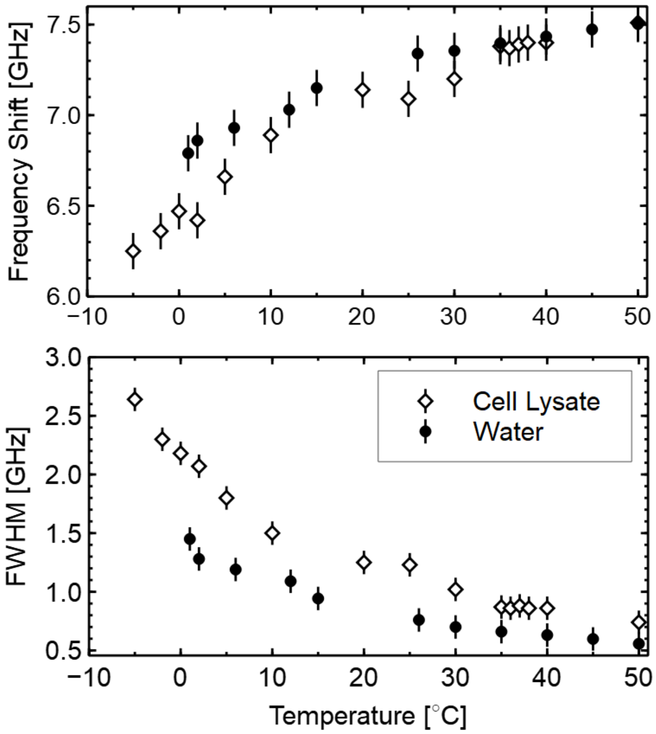

Figure 7.3: Plot of frequency shift and FWHM as a function of temperature for water and an aqueous *E. Coli* cell lysate solution.

at $T > 35$ °C), are nearly independent of temperature and closely resemble those of water. In contrast, solution viscoelastic properties obtained from spectra collected after those in this "high-temperature" region (*i.e.*, at $T \leq 20$ °C) are appreciably different from those of water, as can be seen in Fig. 7.4 by comparison of values for the lysate solution to those for water (direct or interpolated) at a given temperature. A possible reason for this behaviour could be the irreversible denaturation of proteins in the cell lysate solution at $T \sim 40$ °C [24]. If this is in fact the case, this result is very interesting because it means that protein denaturation and configuration (folded or unfolded) can be detected using Brillouin spectroscopy. This hypothesis is also supported by the results of recent molecular dynamics simulations on aqueous protein systems which show some convergence of sound velocity, adiabatic bulk modulus, and shear viscosity toward values for water for $T \gtrsim 40$ °C and a much reduced

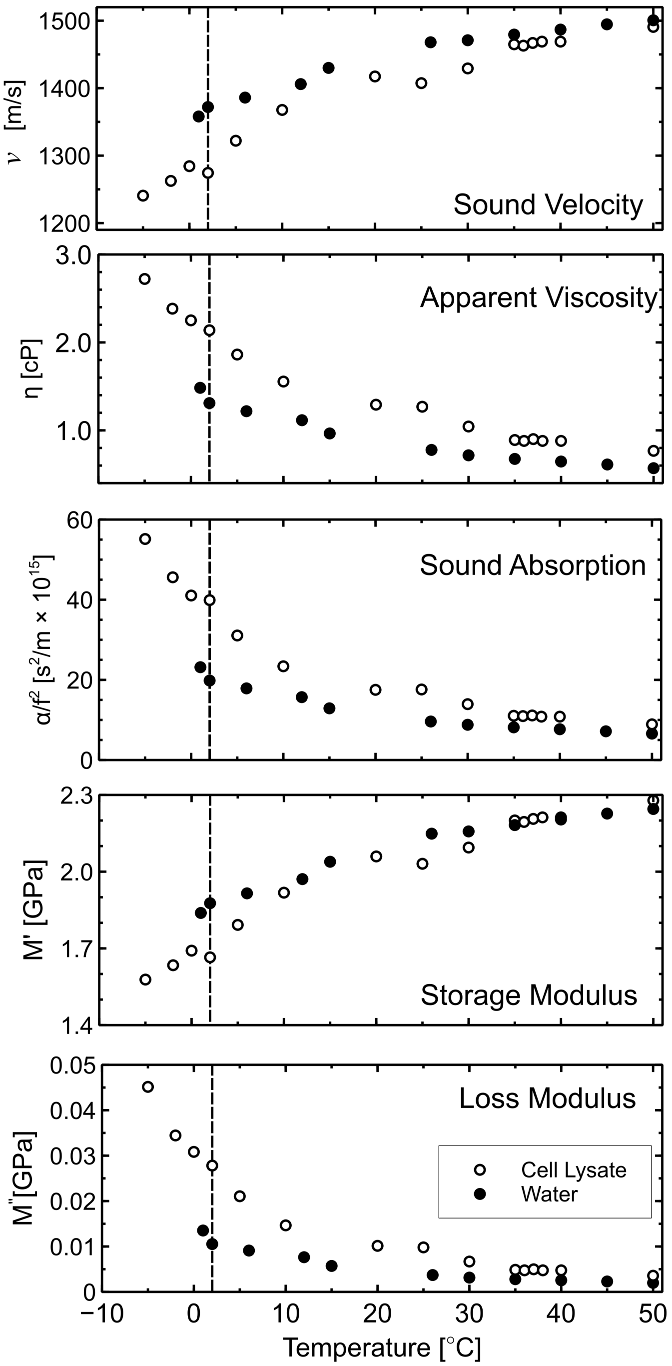

Figure 7.4: Sound velocity, apparent viscosity, frequency-independent sound absorption coefficient, storage, and loss modulus as a function of temperature for an aqueous cell lysate solution. The uncertainty is approximately twice the size of the symbols.

dependence of these quantities on temperature in this range compared to that at lower temperatures (as shown in Ch. 6).

The temperature dependence of several of the cell lysate solution viscoelastic properties seems to display a weak anomaly at $T \sim 2\ ^{\circ}\mathrm{C}$, as indicated by the dashed vertical line in Fig. 7.4. This anomaly is apparent in the velocity, sound absorption, and storage modulus data, but barely discernible in the temperature dependence of the apparent viscosity and loss modulus. Given that a significant fraction of the cell lysate solution is water with a well-known liquid-to-solid phase transition at 0 °C, this anomaly is not completely unexpected and may in fact be a manifestation of a corresponding liquid-solid phase transition in the lysate solution at approximately the same temperature.

It is also interesting to note the qualitative similarity of the temperature dependence of some lysate solution viscoelastic properties to those of simple aqueous protein systems obtained using molecular dynamics simulations (see Fig. 7.4 in this paper and Figs. 2, 4 and 5 in Ch .6). Despite considerable differences in composition, the sound velocity and storage modulus for the lysate solution and nearly all of the model systems show an overall increase with increasing temperature over the range from a few °C to $\sim 40 - 45\ ^{\circ}\mathrm{C}$ and a much weaker dependence for higher temperatures, with some convergence of values toward those for water in this upper range. In addition, the overall decrease in shear viscosity with increasing temperature for the simulated protein-water systems mimics that of the apparent viscosity of the cell lysate solution. Interestingly, similar behaviour was found for the temperature dependence of sound velocity, storage modulus, and apparent viscosity of natural snail mucus, a system comprised primarily, but not only, of water and glycoproteins [11]. When considered together, these results suggest that the underlying physical mechanisms responsible for the bulk viscoelasticity of simple aqueous protein solutions are also at play in multimacromolecular solutions. Consequently, it may be possible to predict the viscoelastic behaviour of complex macromolecular solutions, such as found in biological systems, using rather simple models.

Activation Energy

Figure 7.5 shows the natural logarithm of the apparent viscosity as a function of inverse temperature. The natural logarithim of apparent viscosity for the entire temperature region depends linearly on $1/T$ so we fit an Arrhenius relationship of the form

$$\eta = \eta_0 e^{E_a/k_B T} \tag{7.8}$$

to the data. The activation energy for the cell lysate was determined to be $E_a = 17.1$ kJ/mol, which is approximately 20% higher than the activation energy for water and other polymer-water systems [7, 11, 16]. Notably, the observed data exhibited a linear relationship, indicating a negligible thermal dependence of both the activation entropy (η_0) and enthalpy (E_a) across the entire temperature range studied. In contrast to other systems, no evidence of a transition to non-Arrhenius behavior was observed. For example, in other aqueous protein solutions, the apparent viscosity typically follows an Arrhenius behavior in the high-temperature region ($T \geq 20$ °C), which is associated with the onset of cooperative motions at the molecular level and is often described by a power law or a Vogel–Fulcher relationship [11, 16].

7.5 Conclusion

In this study the GHz-frequency viscoelastic properties of an aqueous solution of *E. coli* cell lysate were probed by Brillouin spectroscopy across a temperature range of -5.0 °C to 50 °C. We find that the observed behaviour in the frequency shift and FWHM, and consequently the speed of sound, viscosity and sound absorption

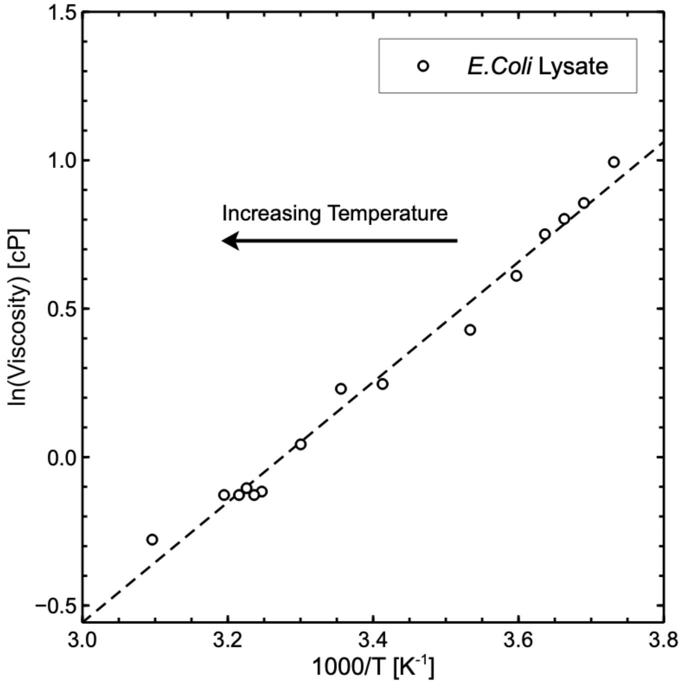

Figure 7.5: Natural logarithm of viscosity for an aqueous solution of bacterial cell lysate as a function inverse temperature. Dashed lines represent best fit. The uncertainty is approximately twice the size of the symbols.

closely resembles that of simple aqueous solutions containing only a single protein or polymer species. For instance, previous Brillouin scattering studies [3, 7, 8, 11, 16, 19, 22] have shown the general increase in frequency shift and decrease in FWHM with increasing temperature. This could have potentially important implications for computer simulations and theoretical work on multimacromolecular systems because it demonstrates that the viscoelasticity of a complex systems can, at least in some cases, be accurately modelled using much simpler systems. The quantitative nature of the results obtained in this work also highlight the potential of Brillouin light scattering spectroscopy as a potent tool for examining the viscoelasticity of complex biological systems, as the influence of proteins on the viscoelastic properties of these systems is still in some ways poorly understood.

7.6 Supplementary Material for: Brillouin light scattering studies of aqueous *E. Coli* cell lysate: Viscoelastic properties of a multimacromolecular solution

Table 7.2: Brillouin peak frequency shift (f_e), full width at half-maximum (Δf_E), and intensity (I_E) for *E* - *E. coli* lysate solution at indicated temperatures.

T [± 0.5 K]	T [± 0.5°C]	f_E [± 0.3 GHz]	Δf_M [GHz]	I_M [Arb. Units]
323.0	50.0	7.5	0.8 ± 0.3	1250 ± 30
313.0	40.0	7.4	0.8 ± 0.3	700 ± 60
311.5	38.5	7.4	0.9 ± 0.3	900 ± 60
310.0	37.0	7.4	0.9 ± 0.3	970 ± 50
309.5	36.5	7.4	0.9 ± 0.3	1030 ± 40
308.0	35.0	7.4	0.9 ± 0.3	1140 ± 30
303.0	30.0	7.2	1.0 ± 0.4	850 ± 50
298.0	25.0	7.2	1.2± 0.5	590 ± 60
293.0	20.0	7.2	1.2 ± 0.5	540 ± 60
283.0	10.0	7.0	1.5 ± 0.7	370 ± 50
278.0	5.0	6.9	1.9 ± 0.6	290 ± 60
275.0	2.0	6.6	2.2 ± 0.8	140 ± 40
273.0	0.0	6.5	2.3 ± 0.8	130 ± 50
271.0	-2.0	6.3	2.4 ± 0.7	130 ± 40
268.0	-5.0	6.3	2.9 ± 0.8	100 ± 50

Bibliography

[1] Fisher scientific. https://www.fishersci.com.

[2] N. Anderson, W. Harris, A. Barber, C. Rankin Jr, and E. Candler. Separation of subcellular components and viruses by combined rate-and isopycnic-zonal centrifugation. *National Cancer Institute Monographs*, 21:253–283, 1966.

[3] M. Bailey, M. Alunni-Cardinali, N. Correa, S. Caponi, T. Holsgrove, H. Barr, N. Stone, C. P. Winlove, D. Fioretto, and F. Palombo. Viscoelastic properties of biopolymer hydrogels determined by brillouin spectroscopy: A probe of tissue micromechanics. *Science advances*, 6(44):eabc1937, 2020.

[4] C. K. Batchelor and G. K. Batchelor. *An Introduction to Fluid Dynamics*. Cambridge University Press, 1967.

[5] A. Borodavka, S. W. Singaram, P. G. Stockley, W. M. Gelbart, A. Ben-Shaul, and R. Tuma. Sizes of long rna molecules are determined by the branching patterns of their secondary structures. *Biophysical Journal*, 111(10):2077–2085, 2016.

[6] C.-L. Chiang, C.-S. Sung, T.-F. Wu, C.-Y. Chen, and C.-Y. Hsu. Application of superparamagnetic nanoparticles in purification of plasmid dna from bacterial cells. *Journal of Chromatography B*, 822(1-2):54–60, 2005.

[7] L. Comez, L. Lupi, M. Paolantoni, F. Picchiò, and D. Fioretto. Hydration properties of small hydrophobic molecules by brillouin light scattering. *The Journal of Chemical Physics*, 137(11):114509, 2012.

[8] L. Comez, M. Paolantoni, P. Sassi, S. Corezzi, A. Morresi, and D. Fioretto. Molecular properties of aqueous solutions: a focus on the collective dynamics of hydration water. *Soft Matter*, 12(25):5501–5514, 2016.

[9] F. Feijó Delgado, N. Cermak, V. C. Hecht, S. Son, Y. Li, S. M. Knudsen, S. Olcum, J. M. Higgins, J. Chen, W. H. Grover, et al. Intracellular water exchange for measuring the dry mass, water mass and changes in chemical composition of living cells. *Public Library of Science ONE*, 8(7), 2013.

[10] H. Fischer, I. Polikarpov, and A. F. Craievich. Average protein density is a molecular-weight-dependent function. *Protein Science*, 13(10):2825–2828, 2004.

[11] D. Hanlon, M. J. Clouter, and G. T. Andrews. Temperature dependence of the viscoelastic properties of a natural gastropod mucus by brillouin light scattering spectroscopy. *Soft Matter*, 2023.

[12] K. C. Huang, R. Mukhopadhyay, B. Wen, Z. Gitai, and N. S. Wingreen. Cell shape and cell-wall organization in gram-negative bacteria. *Proceedings of the National Academy of Sciences*, 105(49):19282–19287, 2008.

[13] A. Johnson, J. Lewis, and B. Alberts. *Molecular Biology of the Cell.* Garland Science New York, NY, USA:, 2002.

[14] S. Johnson and N. Buttress. The osmotic insensitivity of sonicated liposomes and the density of phospholipid-cholesterol mixtures. *Biochimica et Biophysica Acta (BBA)-Biomembranes*, 307(1):20–26, 1973.

[15] J. E. Kay and M. C. Jewett. Lysate of engineered escherichia coli supports high-level conversion of glucose to 2, 3-butanediol. *Metabolic Engineering*, 32:133–142, 2015.

[16] L. Lupi, L. Comez, C. Masciovecchio, A. Morresi, M. Paolantoni, P. Sassi, F. Scarponi, and D. Fioretto. Hydrophobic hydration of tert-butyl alcohol studied by brillouin light and inelastic ultraviolet scattering. *The Journal of Chemical Physics*, 134(5):02B603, 2011.

[17] R. Macnab. Escherichia coli and salmonella: Cellular and molecular biology. *Flagella and Motility*, pages 123–145, 1996.

[18] M. P. Molloy, B. R. Herbert, M. B. Slade, T. Rabilloud, A. S. Nouwens, K. L. Williams, and A. A. Gooley. Proteomic analysis of the escherichia coli outer membrane. *European Journal of Biochemistry*, 267(10):2871–2881, 2000.

[19] G. Monaco, D. Fioretto, L. Comez, and G. Ruocco. Glass transition and density fluctuations in the fragile glass former orthoterphenyl. *Physical Review E*, 63(6):061502, 2001.

[20] J. F. Nagle and S. Tristram-Nagle. Structure of lipid bilayers. *Biochimica et Biophysica Acta (BBA) - Reviews on Biomembranes*, 1469(3):159–195, 2000.

[21] J. M. Newton, J. Vlahopoulou, and Y. Zhou. Investigating and modelling the effects of cell lysis on the rheological properties of fermentation broths. *Biochemical Engineering Journal*, 121:38–48, 2017.

[22] F. Palombo and D. Fioretto. Brillouin light scattering: applications in biomedical sciences. *Chemical reviews*, 119(13):7833–7847, 2019.

[23] B. Panijpan. The buoyant density of dna and the g+ c content. *The Journal of Chemical Education*, 54(3):172, 1977.

[24] G. A. Petsko and D. Ringe. *Protein structure and function.* New Science Press, 2004.

[25] M. Riley. Correlates of smallest sizes for microorganisms. In *Size Limits of Very Small Microorganisms: Proceedings of a Workshop*, volume 3, page 21. National Academies Press Washington, DC, 1999.

[26] J. Rouch, C. C. Lai, and S. H. Chen. Brillouin scattering studies of normal and supercooled water. *The Journal of Chemical Physics*, 65(10):4016–4021, 1976.

[27] R. R. Sinden. *DNA Structure and Function.* Gulf Professional Publishing, 1994.

[28] Y. Trosel, L. P. Gregory, V. K. Booth, and A. Yethiraj. Diffusion nmr and rheology of a model polymer in bacterial cell lysate crowders. *Biomacromolecules*, 24(6):2469–2478, 2023.

[29] Y. Wang, C. Li, and G. J. Pielak. Effects of proteins on protein diffusion. *Journal of the American Chemical Society*, 132(27):9392–9397, 2010.

[30] F. Widdel. Theory and measurement of bacterial growth. *Di dalam Grundpraktikum Mikrobiologie*, 4(11):1–11, 2007.

[31] V. P. Zhdanov. Conditions of appreciable influence of microrna on a large number of target mrnas. *Molecular BioSystems*, 5(6):638–643, 2009.

Chapter 8

Conclusion

8.1 Summary

The acoustic and viscoelastic properties of gastropod snail mucus, and bacterial cell lysate were studied carefully by using Brillouin light scattering spectroscopy. The GHz-frequency viscoelastic properties and phase behavior of a natural gastropod mucus were investigated using Brillouin light scattering spectroscopy in the temperature range of -11 °C $\leq T \leq$ 52 °C as discussed in great detail in Chapter 4. Anomalies in the temperature-dependent spectral peak parameters and derived viscoelastic properties revealed the emergence of a previously unidentified liquid-to-solid phase transition at -2.5°C, with both liquid mucus and solid ice coexisting until at least -11°C. The gradual nature of this transition and the observed temperature-dependent changes in apparent viscosity and hypersound attenuation were attributed to water-glycoprotein interactions, specifically the binding of water molecules to glycoproteins, which hindered the reconfiguration and crystallization necessary for ice formation. Additional

Brillouin scattering experiments were employed to investigate the viscoelastic properties and phase behavior of diluted and dehydrated snail mucus. The temperature range of -11°C $\leq T \leq$ 52 °C was explored for all dilutions of the snail mucus, while the dehydrated mucus was examined with respect to time and corresponding protein concentration. Intriguingly, deviations in both temperature and concentration dependencies of spectral peak parameters and derived viscoelastic properties validate the previously identified liquid-to-solid phase transition at -2.5°C, while additionally revealing an association between concentration and this transition temperature. Particularly in the dehydrated experiment, these findings support the notion of a liquid to solid-like phase transition occurring as the protein-to-water ratio reaches homogeneity in the sample.

This study employed Brillouin spectroscopy to examine the GHz-frequency viscoelastic properties of an aqueous solution containing *E. coli* cell lysate. The investigation spanned a temperature range from -5.0 °C to 50 °C. Notably, this study represents the first investigation of the mechanical properties of *E. coli* using Brillouin scattering. The findings revealed that the observed behavior closely resembles that of simple aqueous protein solutions with a single protein or polymer component. The results in this work carries significant implications for computational simulations and theoretical studies of complex multimacromolecular systems. It underscores the potential for accurately modeling the viscoelastic properties of intricate systems using simpler models. The comprehensive and quantitative nature of the obtained results also showcases Brillouin light scattering spectroscopy's potential as a robust tool for exploring the viscoelastic characteristics of intricate biological systems.

Lastly, this thesis used molecular dynamics simulations to study the bulk viscoelastic properties of water-protein systems in an attempt to uncover the dynamics of these interactions on the microscopic level of these interactions. This study represents the first systematic exploration of protein-water solution viscoelasticity through molecular dynamics simulations. We investigated the temperature-dependent variations in adiabatic bulk modulus, sound speed, and viscosity. The observed trends closely align with those documented in earlier experimental research on protein-water systems [1–8]. The notable consistency between simulation and experimental findings underscores the potential of simulations for assessing macromolecular solution viscoelastic properties. Furthermore, simulations offer additional molecular-level insights into the systems' behavior, complementing experimental observations.

Notably, this research offers fresh insights into the significance of hydration water in protein-water systems of biological relevance. From investigating the spectral peak parameters obtained in Brillouin scattering, and calculated quantities such as apparent viscosity, we were able to extract qualitative information about the conformational changes occurring in the systems studied. Furthermore, it underscores the effectiveness of Brillouin spectroscopy in studying this unique class of natural materials, expanding the range of systems to which this technique has proven to be highly valuable. Moreover, this work also contributes to the ongoing exploration of the role of water in biological processes and establishes a solid foundation for future research in this rapidly evolving field.

8.2 Future Work

While this work provided a careful investigation of the viscoelastic properties of aqueous protein systems, more work is required to fully understand the physics of the interaction between protein and water molecules. To comprehensively explore these interactions, a diverse array of polymer-water systems should be investigated, preferably focusing on well-characterized proteins and polymers. Thus, changing experimental parameters such as temperature and concentration will then allow for more insight into these interactions. Complementing these experiments then with simulations would then allow a extensive comprehensive study of these interactions.

This work also aims at investigating the depression of ice crystals and investigating the true mechanism by which antifreeze proteins inhibit ice from growing. There have been some studies in the past that propose a model that attempts to explain the mechanism of such a feature. We believe glycoproteins bind to water before the system freezes, and do not absorb on ice surfaces as previously proposed [9]. More research in this area needs to be investigated in order to fully understand this phenomenon. An additional aspect to this that we wish to understand is how exactly does nucleation occur in these sort of systems and in water in general. Brillouin scattering experiments alone cannot answer this question, computer simulations should be used in combination with experiments to fully grasp how nucleation occurs. Furthermore, other experimental methods like x-ray diffraction, raman spectroscopy, and nuclear magnetic resonance (NMR) are potential techniques for investigating this phenomenon.

Bibliography

[1] M. Bailey, M. Alunni-Cardinali, N. Correa, S. Caponi, T. Holsgrove, H. Barr, N. Stone, C. P. Winlove, D. Fioretto, and F. Palombo. Viscoelastic properties of biopolymer hydrogels determined by brillouin spectroscopy: A probe of tissue micromechanics. *Sci. Adv.*, 6(44):eabc1937, 2020.

[2] L Comez, L Lupi, M Paolantoni, F Picchiò, and D Fioretto. Hydration properties of small hydrophobic molecules by brillouin light scattering. *J. Chem. Phys.*, 137(11):114509, 2012.

[3] L Lupi, L Comez, C Masciovecchio, A Morresi, M Paolantoni, P Sassi, F Scarponi, and D Fioretto. Hydrophobic hydration of tert-butyl alcohol studied by brillouin light and inelastic ultraviolet scattering. *J. Chem. Phys.*, 134(5):02B603, 2011.

[4] M Pochylski, F Aliotta, Z Błaszczak, and J Gapiński. Structural relaxation processes in polyethylene glycol/ccl4 solutions by brillouin scattering. *J. Phys. Chem. B*, 109(9):4181–4188, 2005.

[5] Dillon Hanlon, Maynard J Clouter, and G Todd Andrews. Temperature dependence of the viscoelastic properties of a natural gastropod mucus by brillouin light scattering spectroscopy. *Soft Matter*, 2023.

[6] Y. Trosel, L. P. Gregory, V. K. Booth, and A. Yethiraj. Diffusion nmr and rheology of a model polymer in bacterial cell lysate crowders. *Biomacromolecules*, 24(6):2469–2478, 2023.

[7] A. Milewska, J. Szydlowski, and L. P. N. Rebelo. Viscosity and ultrasonic studies of poly (n-isopropylacrylamide)–water solutions. *Journal of Polymer Science Part B: Polymer Physics*, 41(11):1219–1233, 2003.

[8] D. F. Hanlon, M. J. Clouter, and G. T. Andrews. Influence of hydration and dehydration on the viscoelastic properties of snail mucus by brillouin spectroscopy, 2023.

[9] S. Ebbinghaus, K. Meister, B. Born, A. L. DeVries, M. Gruebele, and M. Havenith. Antifreeze glycoprotein activity correlates with long-range protein-water dynamics. *J. Am. Chem. Soc.*, 132(35):12210–12211, 2010.

Appendix A

Python Code for Lorentzian Fit

Listing A.1: Python Code to Perform Lorentzian fit

```
import numpy as np
import matplotlib.pyplot as plt
import sys
from lmfit import Model

dat_1 = np.genfromtxt('FILENAME',delimiter=' ') #change data file

xf = dat_1[:,0] # Full X Range
x1 = dat_1[300:485,0] # Lower Shift on LHS - x data
x2 = dat_1[539:724,0] # Lower Shift on RHS - x data

yf = dat_1[:,1] # Full Y Range
y1 = dat_1[300:485,1] # Lower Shift on LHS - y data
```

```
y2 = dat_1[539:724,1] # Lower Shift on RHS - y data

def lorentz(x, y0, A, x0, wid):
    """Fit =y0+(2*A/pi).*(w./(4*(x-x0).^2+w.^2))"""
    return (y0 + A * wid / (4*(x-x0)**2 + wid**2))

gmodel = Model(lorentz)
result1 = gmodel.fit(y1, x=x1,y0 = 12, A=50, x0=-8.5, wid=0.5) # LHS Fit
result2 = gmodel.fit(y2, x=x2,y0 = 12, A=50, x0=8.5, wid=0.5) # RHS Fit


print(result1.fit_report())
print(result2.fit_report())


plt.plot(xf, yf, 'ko-')
#plt.plot(x, result.init_fit, 'k--', label='initial fit')
plt.plot(x1, result1.best_fit, 'r--', label='best fit')
plt.plot(x2, result2.best_fit, 'r--')
plt.legend(loc='best')
plt.xlim(-25,25)
plt.ylim(0,2000)
#plt.savefig('test.png')
plt.show()
```